Nuclear Materials and Energy 29 (2021) 101051

Contents lists available at ScienceDirect

Nuclear Materials and Energy

journal homepage: www.elsevier.com/locate/nme

Multiscale modelling for fusion and fission materials: The M4F project

L. Malerba [a,*], M.J. Caturla [b], E. Gaganidze [c], C. Kaden [d], M.J. Konstantinović [e], P. Olsson [f], C. Robertson [g], D. Rodney [h], A.M. Ruiz-Moreno [i], M. Serrano [a], J. Aktaa [c], N. Anento [j], S. Austin [i], A. Bakaev [e], J.P. Balbuena [b], F. Bergner [d], F. Boioli [k], M. Boleininger [l], G. Bonny [e], N. Castin [e], J.B. J. Chapman [l], P. Chekhonin [d], M. Clozel [m], B. Devincre [k], L. Dupuy [g], G. Diego [a], S.L. Dudarev [l], C.-C. Fu [g], R. Gatti [k], L. Gélébart [g], B. Gómez-Ferrer [n], D. Gonçalves [g], C. Guerrero [a], P.M. Gueye [n], P. Hähner [i], S.P. Hannula [o], Q. Hayat [p], M. Hernández-Mayoral [a], J. Jagielski [m], N. Jennett [p], F. Jiménez [a], G. Kapoor [d], A. Kraych [h], T. Khvan [e,q], L. Kurpaska [m], A. Kuronen [r], N. Kvashin [j], O. Libera [s], P.-W. Ma [l], T. Manninen [o], M.-C. Marinica [g], S. Merino [a], E. Meslin [g], F. Mompiou [t], F. Mota [a], H. Namburi [s], C.J. Ortiz [a], C. Pareige [n], M. Prester [u], R.R. Rajakrishnan [t], M. Sauzay [g], A. Serra [j], I. Simonovski [i], F. Soisson [g], P. Spätig [v], D. Tanguy [h], D. Terentyev [e], M. Trebala [o], M. Trochet [g], A. Ulbricht [d], M.Vallet [g], K. Vogel [d], T. Yalcinkaya [w], J. Zhao [r]

[a] Centro de Investigaciones Energéticas, Medioambientales y Tecnológicas (CIEMAT), Madrid, Spain
[b] Universidad de Alicante, San Vicente del Raspeig, Spain
[c] Karlsruher Institut für Technologie (KIT), Karlsruhe, Germany
[d] Helmholtz-Zentrum Dresden-Rossendorf Ev (HZDR), Rossendorf, Germany
[e] Studiecentrum voor Kernenergie / Centre d'Étude de l'Énergie Nucléaire (SCK CEN), Mol, Belgium
[f] KTH Royal Institute of Technology, Stockholm, Sweden
[g] Université Paris-Saclay, Commissariat à l'Énergie Atomique et aux Énergies Alternatives (CEA), Gif-sur-Yvette, France
[h] Institut Lumière Matière (ILM), Centre National de la Recherche Scientifique, Lyon, France
[i] Joint Research Centre (JRC)- European Commission, Petten, the Netherlands
[j] Universitat Politècnica de Catalunya, Barcelona, Spain
[k] Laboratoire d'Etude des Microstructures (LEM), Centre National de la Recherche Scientifique, Châtillon, France
[l] United Kingdom Atomic Energy Authority (UKAEA), Culham, UK
[m] Narodowe Centrum Badan Jadrowych (NCBJ), Swierk, Poland
[n] Normandie Univ, UNIROUEN, INSA Rouen, CNRS, Groupe de Physique des Matériaux, 76000 Rouen, France
[o] Aalto University, Espoo, Finland
[p] Coventry University, UK
[q] Université de Liège, Belgium
[r] Helsingin Yliopisto, Helsinki, Finland
[s] Centrum Vyzkumu Řež S.R.O. (CVR), Řež, Czech Republic
[t] Centre pour l'Élaboration Elaboration de Matériaux et pour l'Étude des Structures (CEMES), Centre National de la Recherche Scientifique, Toulouse, France
[u] Institut za Fiziku, Zagreb, Croatia
[v] Paul Scherrer Institut (PSI), Villingen, Switzerland
[w] Middle East Technical University (METU), Ankara, Turkey

A B S T R A C T

The M4F project brings together the fusion and fission materials communities working on the prediction of radiation damage production and evolution and their effects on the mechanical behaviour of irradiated ferritic/martensitic (F/M) steels. It is a multidisciplinary project in which several different experimental and computational materials science tools are integrated to understand and model the complex phenomena associated with the formation and evolution of irradiation induced defects and their effects on the macroscopic behaviour of the target materials. In particular the project focuses on two specific aspects: (1) To develop physical understanding and predictive models of the origin and consequences of localised deformation under irradiation in F/M steels; (2) To develop good practices and possibly advance towards the definition of protocols for

* Corresponding author.
E-mail address: lorenzo.malerba@ciemat.es (L. Malerba).

https://doi.org/10.1016/j.nme.2021.101051
Received 26 February 2021; Received in revised form 5 July 2021; Accepted 1 August 2021
Available online 8 August 2021

the use of ion irradiation as a tool to evaluate radiation effects on materials. Nineteen modelling codes across different scales are being used and developed and an experimental validation programme based on the examination of materials irradiated with neutrons and ions is being carried out. The project enters now its 4th year and is close to delivering high-quality results. This paper overviews the work performed so far within the project, highlighting its impact for fission and fusion materials science.

1. Introduction

Nuclear energy, in alliance with renewables, has an important role to play towards a climate-neutral society [1,2,3]. In order to improve the sustainability of this important source of energy, the path to be followed involves the development of fourth generation (GenIV) fission reactors [4] and fusion reactors [5]. Both these technologies impose very severe requirements on materials, in terms of resistance to prolonged high energy neutron irradiation, with significant helium production in the case of fusion, thermal cycles, high temperature and compatibility with corrosive coolants [6,7]. Accordingly, it has been long recognized that fission and fusion materials share several research and development commonalities [8], while over the years steps have been taken towards more detailed designs of reactor demonstrators. When looking at the structural (and cladding for fission) materials' choices that are currently being made by designers of GenIV fission [7] and fusion [9] reactor demonstrators, it is easy to see that the intersection between the two selections are (advanced) ferritic/martensitic (F/M) steels. The main strength of these steels over the more commonly used austenitic steels is the higher resistance to radiation-induced swelling, the higher thermal conductivity and the lower thermal expansion, as well as, importantly for fusion, the possibility of tuning their composition in order to reduce their end-of-life level of activation [10]. This last point makes F/M steels essentially the only possible choice for the structural material of the breeding blanket of a fusion demonstrator. In the case of GenIV fast reactors in Europe, in contrast, it is expected that the cores of the demonstrators (sodium, lead and gas cooled fast reactors) will be mainly fabricated using austenitic steels, because of the return of experience from already built reactors. This, however, will oblige the demonstrators to work, at least in their first phases of operation, at a lower level of performance than expected in commercial reactors (lower temperatures, lower doses, …). In order to reach higher doses, swelling-resistant advanced F/M steels, especially with oxide dispersion strengthening to reach higher temperatures, or alumina forming to guarantee protection against corrosion, need to be developed and used. Thus, F/M steels remain the goal for GenIV commercial fast reactors [7] and this is why these materials are the focus of extensive research and development effort for both applications, with several challenges remaining ahead [10]. Ultimately, for application in the nuclear field these materials need to enter the design codes and this requires that their properties are known or safely predicted in the whole range of operating temperatures, as well as in a sufficient range of radiation doses and in the expected chemical environment.

In this framework, the M4F project brings together the fusion and fission materials communities working on the prediction of irradiation-induced microstructural damage and deformation mechanisms of irradiated ferritic/martensitic (F/M) steels, with focus on the lower side of the operational temperature window, which is determined by hardening and embrittlement [11]. It is a multidisciplinary project, where both modelling and experiments at different scales are integrated to foster the understanding of the complex phenomena that are associated with the formation and evolution of irradiation induced defects and their role on deformation behaviour.

The ultimate objectives of the project (Fig. 1) are:

- To develop physical understanding and predictive models of the origin of localised deformation under irradiation in F/M steels and especially its consequences on the mechanical behaviour of components. This is expected to contribute to providing input to the design codes, for the elaboration of physically-motivated, non-over-conservative design rules, of use for this class of steels in both fission and fusion applications.
- To develop good practices towards the definition of standard protocols for the use of ion irradiation as a tool to evaluate radiation effects on materials, by minimising artefacts with respect to neutron irradiation experiments. The use of nanoindentation (NI), which is able to test the limited thickness affected by ion irradiation, is in this

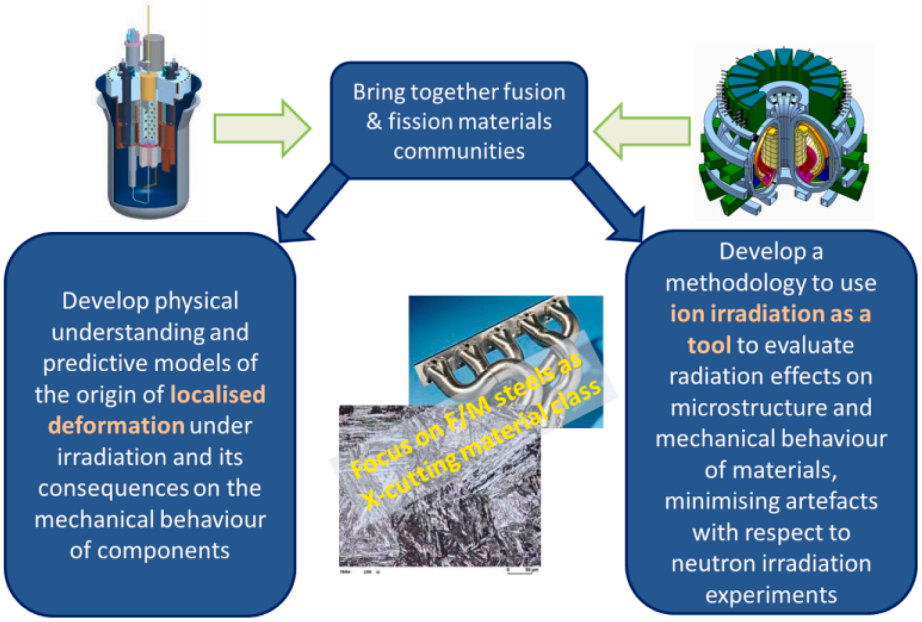

Fig. 1. Objectives of the M4F project.

context expected to provide an evaluation of mechanical property changes related with the microstructural changes.

Radiation-induced hardening and loss of uniform elongation are amongst the major limiting factors for the application of F/M steels as structural materials in nuclear power reactors, based on both fission and fusion, at temperatures below ~ 350–400 °C. Irrespective of the target outlet temperature, this range cannot be fully avoided because of transients and temperature gradients through the different reactor components. In particular, in fusion the water-cooled blanket concept for DEMO will work between 250 and 350 °C and even the He-cooled concept, with outlet temperature anyway not exceeding 500 °C, will have He inlet temperatures in the range 300–350 °C [12]. In this range, most F/M steels undergo severe hardening already after accumulating only relatively few dpa [10,13]. Similarly, the inlet temperatures of systems cooled with Na and Pb and even more PbBi will likely operate in the range where embrittlement may occur. This is caused by the formation of nano-scale defects such as dislocation loops, voids and solute clusters that act as obstacles to gliding dislocations, thereby increasing the hardness and consequently affecting the fracture toughness of the material [14,15]. Some of these defects can be absorbed by dislocations upon deformation, thereby causing, after hardening, dramatic loss of uniform elongation [16]. The absorption of hardening defects leads indeed to a change of the deformation mode in the irradiated state, characterized by a strong localization of the plastic flow in so-called clear bands or dislocation channels [17], with subsequent softening and reduction of irradiation induced hardening, respectively, within the course of plastic deformation. This behaviour is not limited to the F/M steels and is observed in irradiated pure metals such as Fe [18,19], as well as in austenitic [20,21] and reactor pressure vessel [22] steels used in current nuclear power plants. The investigation of post-irradiation plastic deformation in body-centred-cubic (bcc) Fe grains by 3D dislocation dynamics simulation revealed the dislocation decoration effects equivalent to a shortening of initial dislocation sources to play an important role in the flow localization process [23]. The complete understanding of plastic flow localization in the channels involves, therefore, a correct assessment of the microstructure evolution that is produced by irradiation, as well as the comprehension and modelling of plastic deformation, from elementary processes to the level of propagation of dislocation channels between grains. This involves mechanisms that occur at scales ranging from the atomic level to the dislocation, crystal and polycrystal scales. This multiscale approach is therefore pursued within the project, including neutron and especially ion irradiation experiments.

The interest in using heavy ion irradiations to investigate neutron irradiation damage in materials reaches back to the 1970 s [24]. Recently this interest increased considerably because of a combination of factors: growing need to understand irradiation effects on nuclear materials under a variety of fission and fusion-relevant conditions, together with limited access to neutron irradiation facilities and limited variability of irradiation parameters in these facilities. This prompted studies on issues that need to be taken into account when attempting to transfer results of ion irradiation to neutron environments, such as [25]. These issues include:

- The effect of higher dose rates [25,26];
- The effect of injected interstitials and the vicinity of a surface [25,27];
- Effects related to the energy spectrum and cascade morphology [25];
- Rastered versus defocused beam and pulsed versus continuous irradiation [28,29];
- The angle of incidence of the ion beam [30];
- Carbon contamination [31,32].

Among the most important conclusions of these studies is the fact that, depending on the irradiation temperature, self-ion energy values>5 MeV have to be used in order for a “safe zone” to be formed [25] in Fe-based alloys, where ion irradiation artefacts are minimised. Moreover, it is important to foresee a number of countermeasures [31,32] to avoid, or at least minimise, carbon contamination, as much as possible. However, it remains to be verified whether and up to what extent these recommendations are sufficient to extrapolate from ions to neutrons, while there is no fully clear perception of the consequences of the above effects on the microstructure that is observed under ion versus neutron irradiation when the conditions are comparable. For example, in Fe-Cr model alloys dislocation loops have been observed to be homogeneously distributed after ion irradiation for different Cr contents, while they were preferentially aligned along dislocation lines and grain boundaries in Fe-Cr alloys with 5 at% Cr or more after neutron irradiation under similar conditions [33,34]. Likewise, α’-phase particles were formed in Fe-Cr alloys with 9 at% Cr or more under neutron [35–38], but not under ion irradiation [34,39]. In contrast, the features of irradiation-induced solute clusters seem to agree for both types of irradiation under the same conditions [37–39]. While in the case of the α‘-phase it was possible to identify the origin of the difference to be the injected interstitial [27], this connection is not always immediately clear. In addition, in order to produce a sort of ion-to-neutron “transfer function’, it is necessary to develop models that should go beyond the basic SRIM (http://www.srim.org) results for the design of ion-irradiation experiments [40,41], by providing information also on the trends that different ion irradiation modes will produce on the microstructure evolution. It is indeed believed that the traditional temperature shift model that is used to compensate for the dose-rate [42] is a strong and probably largely inadequate simplification, that suggests different temperature shifts for different microstructural features, as concluded also by Zinkle and Snead [25]. Appropriate microstructure evolution models that include all the features of ion irradiation experiments do not exist, yet. It is also important to note that the possibility of transferring data from ion irradiation results to neutrons requires that a number of post-irradiation chracterization issues, not listed above, should be addressed, as well. The fact that ion irradiation gives rise to thin damage layers, steep damage profiles and microstructure variations as functions of depth prevents in several instances the use of bulk characterization methods that, in contrast, can be safely applied to neutron-irradiated samples. One of the main limitations certainly concerns the evaluation of mechanical property changes under ion irradiation. These are broadly the problems that the M4F project is addressing, by combining targeted experiments and the use of specific mechanical characterization methods, such as nanoindentation, with suitable advanced models, ranging from atomistic to continuum.

In general, the distinctive feature of the M4F project is its combination of multiscale physical modelling approaches and exhaustive advanced microstructural and mechanical characterisation using several complementary techniques. This enables a full comprehension of the physics that drive the change of properties under irradiation of F/M steels, including direct comparison between the effects of neutron and

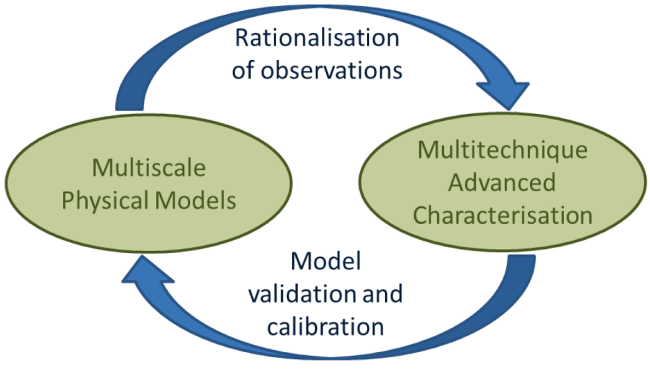

Fig. 2. Two-way interaction between models and experiments.

ion irradiation. Models and experiments feed each other: models provide a rationalisation of experimental observations based on fundamental physical laws and possible mechanisms; in turn, experimental data that cover as many microstructural features and deformation modes as possible, allow the validation and the calibration of the models (Fig. 2).

The models used in the project cover a wide range of scales and methods. In the **Supplementary Material** (**Table SM.1**) the list of the 19 different codes used and/or developed in the project is provided. Specific materials were chosen at the beginning of the project for the experimental programme, namely F/M model alloys (with 9 and 14%Cr, with or without addition of minor solutes) and one steel, Eurofer97, as detailed in Tables 1 and 2.

The model alloys have been chosen because their simpler chemical composition and controlled microstructure (fully ferritic, G alloys in Table 1, versus largely martensitic, L alloy in Table 1 and Eurofer97) enable the effects of different variables to be separated. The list includes Fe, because this material is always a good reference to understand the effects of the alloying elements that are added to it. Details about the fabrication and purity of the selected alloys can be found in [43]. The reason of the choice of their composition is detailed in section 3.1.3. In contrast the steel, Eurofer97, provides data for a material of technological interest, the behaviour of which is interpreted based also on the observations made on the model alloys, after irradiation under the same conditions. The heat of Eurofer97 later exposed to neutron irradiation was produced by Böhler Austria GmbH (heat 83699). It was normalized at 979 °C for 1 h 51 min., followed by air cooling. The heat was then tempered at 739 °C for 3 h 42 min., followed by air cooling. The samples were cut from ∅=100 mm cylindrical bars, such that the sample axis and bar axis coincide.

All these materials except three (G391, G392 and G393) had been neutron irradiated to low dose (0.11 dpa) in the Callisto loop of the BR2, the materials testing reactor of SCK CEN, at two temperatures (290 and 450 °C), in the framework of the FP7/MatISSE project [43]. Some Eurofer97 specimens came also from a previous irradiation in BR2 at 300 °C, to higher doses. All these irradiations, after complementary post-irradiation examination (PIE) performed in this project, provide valuable data for the models and a reference for the comparison with ions.

This paper presents the structure of the M4F project and highlights some of the results that have been so far produced, while discussing their possible future impact. For more details the reader is obviously redirected to the specific publications. It is important to present the project structure, the overall connection between activities and some preliminary results, as a reference for future papers that will detail more specifically the results obtained in it.

2. Project structure and content

The project is organized in two scientific domains, namely irradiated microstructure (Domain 1, DM1) and plastic deformation (Domain 2, DM2). DM1 includes two work-packages (WP), which have in common the focus on the microstructure evolution under irradiation, as follows. (Note that WP1 deals with ethical aspects thus its description is out of scope here).

WP2: Radiation-induced microstructure evolution. This WP investigates how specific features of Fe-Cr-C-X alloys - model alloys for F/M steels, where X stands for any other minor substitutional alloying elements, e.g. Ni, Si, P, Mn, … - influence and determine the microstructural changes induced in them by neutron irradiation. Focus is on the formation and configuration of irradiation defects, with a view to identifying the features that mainly cause radiation-induced hardening and subsequent embrittlement in F/M steels, as input to DM2. This is done combining advanced physical models with refined multi-technique examination of irradiated materials. A comparison of neutron with ion irradiation under comparable conditions is also performed, to highlight differences or similarities between the two irradiation techniques. In particular, WP2 studies:

- Magnetic interactions and transitions at the electronic and atomic scale, addressed by using density functional theory (DFT) and developing DFT-based models that account both for temperature and spin effects, with appropriate experimental verification whenever possible.
- Effect on the microstructural evolution of the initial microstructure (e.g. ferritic versus martensitic), the Cr content and the C distribution in the matrix, as well as of other minor substitutional solutes. This is studied by performing large-scale object kinetic Monte Carlo (OKMC) simulations, which are contrasted with comprehensive experimental defect characterization of neutron- and ion-irradiated Fe-Cr-C-X alloys.

WP3: Transferability of ion and neutron irradiation. This WP is specifically focused on developing good practices to use ion irradiation as a tool to evaluate radiation effects on materials. The goals in WP3 are, accordingly:

- To improve the basic understanding of how the microstructure evolves under irradiation, the mechanisms and factors influencing this evolution and, in particular, how they are affected depending on whether the impinging particles are ions or neutrons. This is done by developing and validating suitable microstructure evolution models. Specific ion irradiation experiments are in addition performed to cast some light on the effect of its specificities, such as high dose-rate, rastering versus defocused beam, damage gradient, etc. …
- To provide eventually guidance for the design of experiments based on ion irradiation as neutron irradiation surrogate, in terms of identification of suitable irradiation conditions and recommendations for post-irradiation examination (PIE), so as to avoid potential ion-irradiation specific artefacts.

Fig. 3 schematically describes the flow of information between WPs

Table 1
Basic composition of the materials selected for the experiments in M4F. The last column specifies in which WP each material was studied. For the detailed composition of Eurofer97 see Table 2.

ID	Short name	Cr (w.%)	Ni (w.%)	Si (w.%)	P (w.%)	Al (w.%)	WP where studied
G379	Fe	0.002	0.007	0.001	0.003	0.023	WP2, WP3, WP6
G385	Fe-9Cr	9.1	0.009	0.004	0.003	0.027	All WP
G389	Fe-9Cr-NiSiP	9.1	**0.092**	**0.212**	**0.032**	0.028	WP2, WP3
G390	Fe-14Cr	14.5	0.009	0.008	0.003	0.030	WP3
G391	Fe-14Cr-Ni	14.4	**0.094**	0.004	0.003	0.030	WP3
G392	Fe-14Cr-Si	14.5	0.007	**0.203**	0.003	0.023	WP3
G393	Fe-14Cr-P	14.4	0.008	0.003	**0.032**	0.024	WP3
G394	Fe-14Cr-NiSiP	14.4	**0.087**	**0.194**	**0.031**	0.025	WP2, WP3
L252	Fe-9Cr-NiSiP F/M	9.1	**0.07**	**0.09**	**0.012**	0.007	WP2, WP3, WP6
E97	Eurofer	8.99	0.007	0.07	<0.005		All WP

	C	Cr	N	Si	P	Ni	V	Ta	W	Mn	S	Ti	Al	O	Mo
Fe*	<0.005		<0.005	<0.005	<0.005	<0.005					<0.005				

* Electrolitic iron composition used for G alloys

Table 2
Composition of Eurofer (in wt.%), heat E83699, Böhler Austria GmbH.

ID	C	Cr	N	Si	P	Ni	V	Ta
E97	0.12	8.99	0.017	0.07	<0.005	0.007	0.19	0.14
	Mo	Cu	Ti	Al	Sn	As	Pb	S
	<0.001	0.022	0.009	0.008	<0.005	<0.005	<0.0003	0.004
	W	Mn	B	Nb	Zr	Sb	O	Fe
	1.10	0.44	<0.001	<0.001	<0.005	<0.005	0.0013	Balance

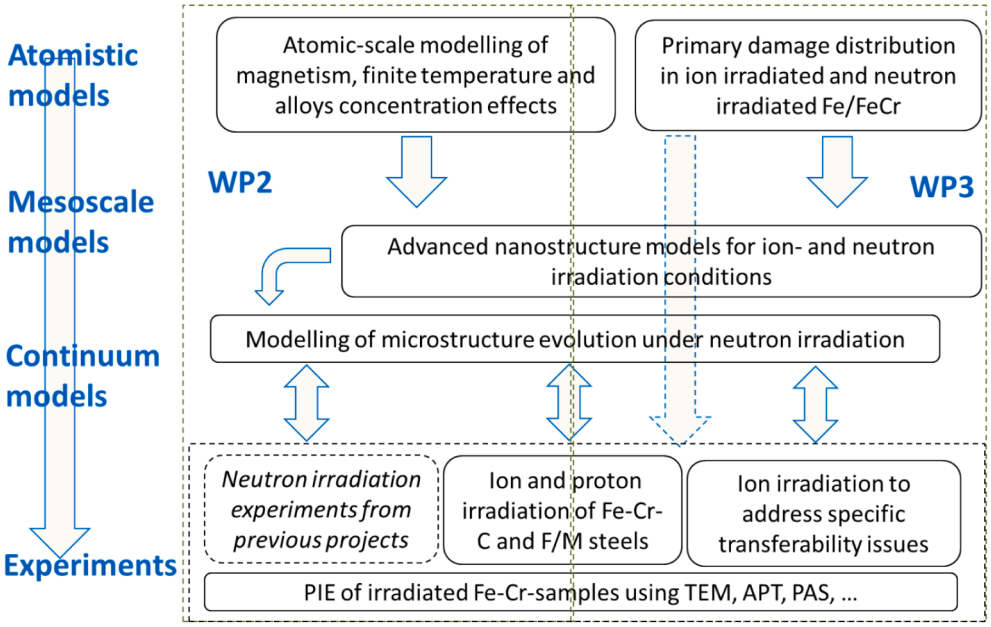

Fig. 3. Connections between scales and tasks in DM1.

and tasks through different scales in DM1.

DM2 is in turn organised in three WPs according to physical scales. They have in common the study of materials subjected to deformation:

WP4: Deformation mechanisms at the grain scale. This WP develops dislocation dynamics models to describe deformation at the grain level, accounting for the presence of irradiation defects, including the influence of alloying elements on dislocation glide and on the interaction strength between dislocations and irradiation defects. Simulations are performed at different length- and time-scales, from the atomic (dislocation cores) to the continuum scale (entire grain). Experimental work for validation of the models is included in the WP.

WP5: Channelling at the polycrystal scale. This WP investigates channeling at the polycrystalline scale and its impact on the deformation and damage evolution. The main outcome will be the prediction of the post yield-post necking behavior of irradiated F/M steels by using mean-field and full-field homogenization, finite element crystal plasticity and continuum mechanics modelling tools. Experimental observations to support the above mentioned simulations are carried out.

WP6: Nanoindentation. Here nanoindentation models and experiments are applied to study irradiation hardening and how irradiation affects plastic flow in ion irradiated specimens. Noting that ion irradiated layers present inhomogenous damage profiles, these experiments, with the support of suitable models, are also used to define good measurement practice for the execution of NI tests on the small thickness within which ion irradiation affects materials.

Fig. 4 schematically describes the flow of information between WP and tasks through different scales in DM2, including input from DM1.

3. Results

3.1. Radiation-induced microstructure evolution

3.1.1. Density functional theory based modelling and experimental validation

Multiscale modelling of radiation effects almost always starts with a cohesive model at the atomic scale. The most commonly used high-fidelity cohesive models are based on DFT calculations, sometimes explicitly, sometimes indirectly through fitting force fields of different kinds. For studies of Fe-Cr alloys, DFT simulations have in the last decades played a crucial role. The prediction of mixing energy asymmetry [44–47] and consequent high solubility of Cr together with calculations focusing on the solute–defect interactions [48–51] sparked wide interest. How these properties affect for instance the phase diagram, embrittlement, radiation induced segregation and the concentration dependence of swelling has been the focus of numerous papers and large projects [52–57]. DFT has thus over the years proven to be an invaluable tool that can be used to understand many features and properties of this and many other alloys. Recent work combined the predictive power of DFT with machine learning, using a kinetic Monte Carlo model driven by a neural network that was trained directly on DFT calculated migration barriers in the Fe-Cr system. This work showed how well DFT captures the physics of phase separation in supersaturated alloys through the near perfect agreement with thermal ageing experiments [58–59]. It is thus well-established that systematic DFT studies of defects are of crucial importance. In this project, a database of 2000 vacancy and 5600 self-interstitial atom (SIA) migration barriers has been generated for Fe-Cr using DFT calculations, with either a vacancy or a SIA defect and with Cr concentrations ranging from 0 to 40 at. %. The data, still under

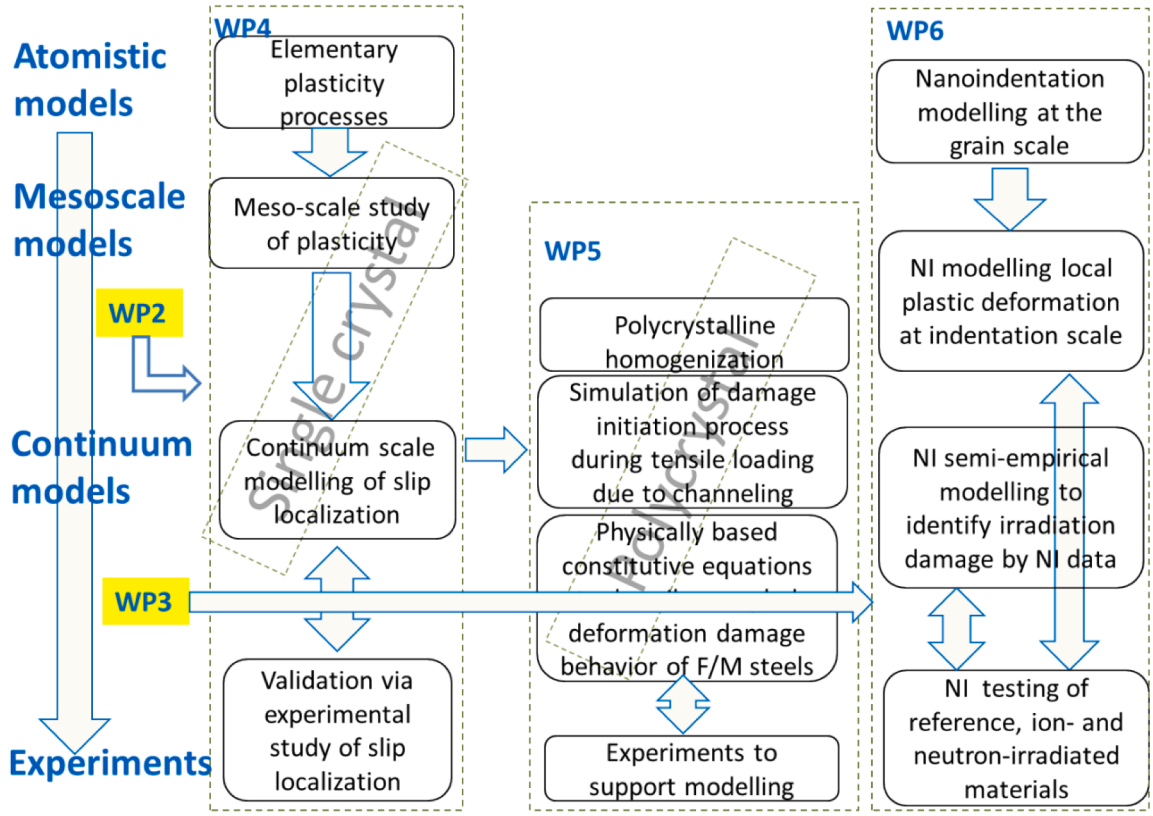

Fig. 4. Connections between scales and tasks in DM2, including link with DM1.

analysis, are employed to investigate coupled magnetic and concentration effects in Fe-Cr alloys. As a first step of the analysis, point defects in body-centered cubic Fe, Cr and concentrated random magnetic Fe-Cr alloys have been extensively investigated not only using DFT, but also the theory of elasticity [60]. It was found that the volume of a substitutional Cr atom in ferromagnetic bcc Fe is approximately 18% larger than the volume of a host Fe atom, whereas the volume of a substitutional Fe atom in antiferromagnetic bcc Cr is 5% smaller than the volume of a host Cr atom. Elastic dipole and relaxation volume tensors of vacancies and SIA exhibit large fluctuations, with vacancies having negative and SIA large positive relaxation volumes. To understand the origin of differences between the relaxation volumes of dumbbells on Fe and Cr sites, the values of relaxation volume have been correlated with the variation of the magnitude of the magnetic moment of the supercell caused by the defect. Fig. 5 shows that the relaxation volumes of dumbbells are smaller when the magnetic moment is more negative. This suggests that magnetism has a strong correlation with structural relaxation and hence relaxation volumes of defects in Fe-Cr alloys, which is consistent with the fact that internal friction (IF, *mechanical* relaxation) and magnetic after effect (MAE, *magnetic* relaxation) experiments provide typically very similar results [61]. The difference in magnetic properties between the structures containing Fe-Fe and Fe-Cr dumbbells is caused mainly by the differences in magnetic moments of the atoms forming the dumbbells.

Dipole tensors of vacancies are nearly isotropic across the entire alloy composition range, with diagonal elements decreasing as a function of Cr content. Fe-Fe and Fe-Cr SIA dumbbells are more anisotropic than Cr-Cr dumbbells. Fluctuations of elastic dipole tensors of SIA defects are primarily associated with the variable crystallographic orientations of the dumbbells. Statistical properties of tensors have been analyzed using their principal invariants, suggesting that point defects differ significantly in alloys containing less or>10% at. Cr. This study showed the clear benefits of an approach that combines *ab initio* treatment of defects with auxiliary analysis based on elasticity. This enabled

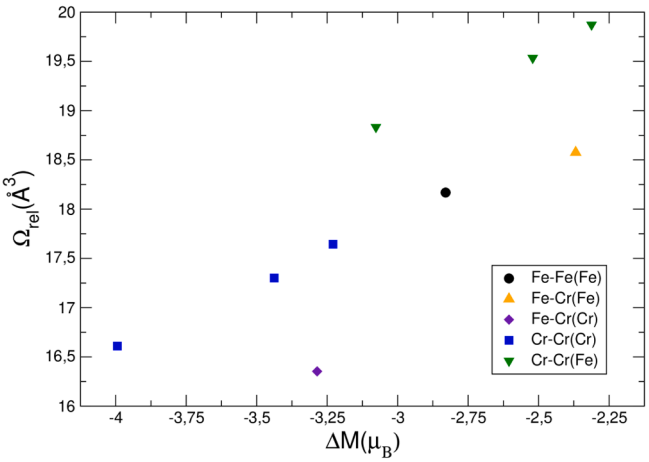

Fig. 5. The relaxation volumes of dumbbells in bcc Fe matrix as functions of the change in the magnitude of the total magnetic moment in the supercell associated with the formation of the defect [60].

the elastic effects of expansion and contraction of the lattice, which are due to the fact that the atoms forming the alloy have different volumes, to be quantified. An example of application of this approach for another bcc metal, tungsten, is given in [62], where DFT-predicted elastic tensors for point defects and point defect clusters are used to generate stress fields that enter a finite element modelling framework, which can be eventually used for modelling on the macroscale. Something similar will be attempted in the case of Fe, in the framework of WP4 (section 3.2.2).

Using the above and other DFT data as reference, spin dynamics simulations have been performed to investigate the magnetic properties in $Fe_{1-x}Cr_x$ alloys for different Cr contents and degrees of Cr clustering (α' phase) [63]. A magnetic cluster expansion (MCE) Hamiltonian that

includes both longitudinal and transverse fluctuations of magnetic moments was developed, in the framework of Langevin spin dynamics. This revealed a strong dependence of the magnetic properties of the Fe-Cr alloys on the local microstructure. The magnetization of the disordered solid solutions is shown in Fig. 6 over a temperature range of 100 K < T < 1500 K. At low temperatures, the magnetization decreases as the Cr concentration increases. The magnetization profiles are similar to pure Fe as the temperature is raised. For Cr concentrations of 5 and 9 at.%, the magnetization is found to remain finite to temperatures higher than the Curie temperature, T_C, in pure Fe.

Upon increasing temperature, the Fe moments close to the interfaces became more disordered than in the bulk. The Cr cluster interface acted as a magnetic disordering nucleation site with a reduced effective T_C. Conversely, the Cr moments on the interface remained statistically correlated at temperatures exceeding the Néel point. The spin–spin autocorrelation and first nearest neighbour correlation functions were studied in Cr clusters and (0 0 1) Fe-Cr superlattices. Contrary to expectation, the high index of the cluster interface did not significantly change the observed correlation of Fe and Cr across the interface with respect to the simple (0 0 1) case. Fe magnetic moments near the interface fluctuate more readily than in the bulk of the α phase. This resulted in enhanced susceptibility of Fe atoms in the interfacial layers. The dynamic properties observed for the impure clusters remained consistent with the pure clusters and (0 0 1) interface. These studies may help in the interpretation of non-invasive ways of determining the level of Cr precipitation through the observation of magnetic properties of alloys, similarly to what was done in [64].

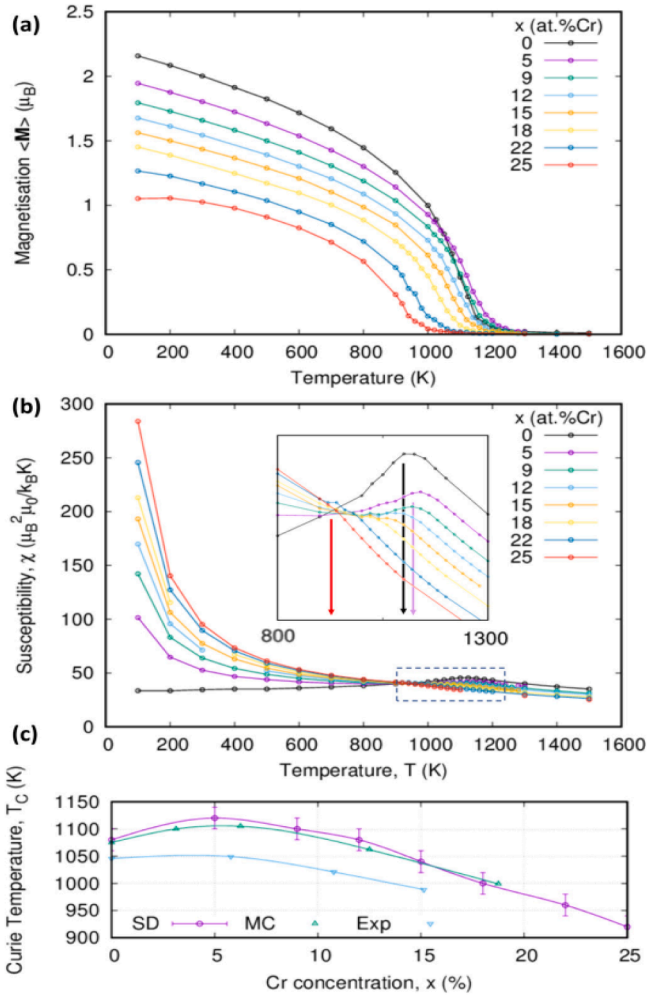

Fig. 6. Magnetic properties of disordered $Fe_{1-x}Cr_x$ solid solutions with different Cr concentrations. (a) Magnetization versus temperature. (b) Magnetic susceptibility versus temperature. (Inset: Susceptibility around the Curie temperature T_C) The points of inflection for × = 0, 5, and 25 at. % Cr are indicated by arrows. (c) Curie temperature T_C versus Cr concentration as determined from the susceptibility [Reprinted figure with permission from Ref. 63, with licence no. RNP/21/FEB/036556. Copyright 2019 American Physical Society].

The magnetic properties of Fe-Cr, especially the ferro-to-paramagnetic transition in iron-rich alloys, which occurs at T_C, cause a strong acceleration of diffusion above it (kink of the Arrhenius plot of diffusion coefficients in many iron based alloys), thereby influencing also the processes of precipitation and segregation. In order to be able to perform atomistic kinetic Monte Carlo (AKMC) simulations of diffusion and precipitation/segregation kinetics that take these effects into account, an atomistic Hamiltonian that describes both thermodynamic and diffusion properties of Fe-Cr alloys has been built, also based on the above and additional first principle calculations. The starting point was the MCE by Lavrentiev *et al.* [65], which includes an explicit treatment of the magnetic moments using a Heisenberg-Landau formalism, with parameters fitted to DFT calculations of various chemical and magnetic configurations. The corresponding phase diagram has been built, using equilibrium Monte Carlo methods and the parameters of the original MCE have been modified to take into account the vibrational entropy of the system and improve the phase diagram description, in particular reduce the maximum temperature of the α-α' miscibility gap, in agreement with experiments [66].

This MCE for the Fe-Cr alloy is now being adapted to include the description of the properties of vacancies and carbon interstitials (in stable and saddle-point positions) with parameters fitted to DFT calculations. The on-site terms of the MCE have been modified for atoms in first and second nearest neighbour positions of the vacancy, to reproduce the change of the amplitude of the magnetic moments it induces: a specific interaction model has been developed for the saddle-point properties and the parameters of the BCC and saddle-point models have been respectively fitted to DFT calculations of formation and migration energy values in Fe-Cr alloys. In addition, the equilibrium and kinetic Monte Carlo codes have been parallelized in the part that deals with spin changes, which accounts for most CPU time, as these simulations require attempting many spin relaxations (typically 100–1000) after each atomic exchange (for equilibrium Monte Carlo) or vacancy jump (for kinetic Monte Carlo). Without parallelization, the systematic study of diffusion in concentrated alloys and the simulation of precipitation kinetics would be very difficult. The parallel code reproduces well the results that were previously obtained in pure iron, with good scalability. Subsequently, the AKMC method will be used to calculate diffusion coefficients of Fe, Cr and C, accounting for the effects of the magnetic transition and of the alloy composition. For the diffusion of Fe and Cr (which occurs by the vacancy mechanism) the evolution of the Gibbs free energy of formation and migration is determined independently. The method has been recently successfully applied to the self-diffusion and impurity diffusion of Cu in iron [67].

These AKMC models will be eventually validated on experiments of determination of interdiffusion coefficients at 500 °C in multilayer alloys that are being performed combining nanometer-scale transmission electron microscopy (TEM) techniques and atom-probe tomography (APT). The structure and the chemical composition of (0 0 1)Fe/(0 0 1)Cr superlattice have been analysed after deposition and after annealing at 500 °C for 4 h. The annealing increases from 9.7 ± 0.3 nm to 10.3 ± 0.3 nm the iron layer thickness and decreases from 9.4 ± 0.3 nm to 8.6 ± 0.3 nm the chromium layer thickness (measurements on 3 layers). Before annealing, the chromium and iron contents in contiguous multilayers, as measured by electron energy loss spectroscopy (EELS), are equal to 100% and there is no change in the solute contents near the dislocation lines. After annealing, the formation of misfit dislocation lines at the interfaces affects the diffusion. The distribution of chromium and iron within the layers was determined by APT and the diffusion anisotropy in the iron and chromium revealed by EELS layers has been

confirmed. Away from the defects, the Cr content in the Cr layers reaches 100% and the Fe content along the dislocation lines varies between 10 and 90% over the 8 dislocations detected. Within the iron layers, in contrast, Cr diffuses mainly homogeneously. A content of 4.7% at. Cr was measured at the center of the layers. However, part of the diffusion is heterogeneous, since a maximal content of 8 at. % has been measured near the dislocation lines. The results of homogeneous diffusion should be comparable with simulations performed with the above AKMC. This work is still in progress.

In parallel to the above work, focused on the atomistic description of the Fe-Cr-C system, the development of machine learning-based spin–lattice dynamics potentials that consider magnetic excitations is being explored, separately, for Fe-C and Fe-Cr. If successfully developed, these potentials will enable atomic-level calculations of enhanced reliability with millions of atoms, to produce the parameters and provide the mechanisms that are needed for higher scale microstructure evolution models (**section 3.1.2**). As a first step, various empirical potentials based on the embedded atom method (EAM) formalism and currently used to study radiation defects in iron have been reviewed. Based on this review, a sort of last chance was given to new EAM empirical potentials for Fe to study irradiation-induced defects, such as self-interstitial atom clusters or dislocation loops [68]. These potentials were fitted to appropriately selected experimental values of solid-state properties, as well as *ab initio* formation energies of basic point defects in the solid crystal and forces acting on the atoms in the liquid or in random state configurations. Bulk and defect properties were compared to validate the transferability of these new potentials. The energy landscape of the three-dimensional C_{15} SIA cluster configurations was also explored using these potentials, thereby identifying three selection rules that facilitate the construction of the lowest energy ones. These rules have practical importance, as they enable the construction of C_{15} clusters with hundreds of interstitials with minimal effort. The newly-developed potentials have then been used to address the relative stability of $\frac{1}{2}\langle 1\,1\,1\rangle$ dislocation loops and C_{15} clusters. This analysis gives a crossover between C_{15} and $\frac{1}{2}\langle 1\,1\,1\rangle$ cluster below 50 SIAs. This information is potentially of high importance for, e.g., object kinetic Monte Carlo (OKMC) models that are used to trace the microstructure evolution in Fe alloys. The specific crossover values are dependent on the empirical potential, though. The shortcomings of the existing Fe potentials and the lack of any universally applicable potential were thereby highlighted. Ironically, even after additional developments and improvements, the traditional empirical potentials fail to reach a consensus on the energy landscape of radiation-induced defects in bcc metals. This is a clear motivation to explore new approaches in order to increase the accuracy and the transferability of empirical force fields, such as surrogate models or machine/statistical learning approaches.

As a step forward towards the development of machine learning type interatomic potentials, the concept of "distortion score" of local atomic environments was introduced, to describe the statistical distance from a reference structure, for example a perfect crystal structure [69]. Based on these distortion scores, structural defects were identified as atoms-outliers deviating from the reference structure. This score facilitates the automatic localization of defects and enables their stratified description, which allows the zones with different levels of distortion to be distinguished within the structure. The method is well adapted for the detection of structural defects and for monitoring their trajectories, as well as for tracking structural changes during phase transitions or crystallization. When computing the distortion scores with respect to the underlying perfect crystal structure, there is conjecture between the computed scores and the local atomic energy (i.e., the proposed distortion score exhibits a correlation with the local atomic energy). Trying to better understand the origin of this correlation, a panel of statistical distances was proposed, which establishes a good agreement with the local energies. This finding opens up many perspectives in the field of computational materials science, in particular applications ranging from the surrogate concept for the energy per atom to the selection of the relevant structural information for the evaluation of energy barriers. The proposed definition of defects through the concept of distortion score serves not only to reinforce the performance of traditional approaches, but also to design and improve machine learning interatomic potentials such as multicomponent force fields. Although not developed further here than for pure bcc Fe, yet, this approach has great potential in enabling robust applications of machine learning for multicomponent materials modelling given that an issue of key interest is managing the complexity that is present in concentrated magnetic alloys where defects are created continuously.

3.1.2. Microstructure evolution models

Microstructure evolution models, specifically those based on the already cited OKMC techniques, started to be used already in the late 1990 s to simulate the effects of neutron and ion irradiation in α-Fe [70–82] and its alloys [75,83–90]. These models, together with phase field [91] and cluster dynamics [92], each of them with advantages and inconveniences (the discussion of which is out of the scope of the present paper), allow the simulation of the microstructure evolution under irradiation conditions that are comparable with the experimental ones. OKMC models have been evolving over the years, by spanning increasingly larger timescales, and thus dose intervals, as well as including more details about the defect configurations [70–90]. For long, only vacancies and self-interstitials, single and in clusters, were tracked, without making any distinction about their inherent characteristics. As more information arose from atomistic calculations, the models became more complex and different configurations of defects were distinguished and considered, so long as possible. Therefore, several of the DFT results from the work described in section 3.1.1, as well as other insights into how magnetism influences the properties of Fe-Cr-C alloys, or more complete and accurate descriptions of the properties of defects such as different families of self-interstitial clusters, are expected, partly now and mostly in the future, to contribute to improve the quality and reliability of the microstructure evolution models. Before the start of M4F, the application of OKMC models was hindered by both computational and physical limitations. From the computational point of view, one of the problems was the difficulty of parallelising these algorithms in order to increase simulated volumes and times [93–95]. Earlier attempts [93] turned out to be not so effective [94], while recent ones [95] still need full assessment. On the physical side, these models have had so far limited application to alloys: either only a second element has been added explicitly [75,81], or a "grey alloy' approach has been used [73,79,80,83–90]. The latter consists in translating the effect of the presence of solute atoms or impurities into modifications of, especially, the defect mobility parameters, either directly [83–90] or by introducing "effective traps' [73,79,80]. As described in what follows, the project addressed both these limitations, with a view to removing them, with a reasonable degree of success.

As a preliminary step to performing ion irradiation experiments, and before entering the details of microstructure evolution models, binary collision approximation (BCA) simulations were used to find ion implantation conditions that could emulate the neutron damage, at least in terms of primary damage [96]. For this, the primary knock-on atom (PKA) spectra were first calculated for different fission and fusion neutron facilities. Then, using BCA calculations, the PKA spectrum for proton and self-ion irradiations was calculated for different implantation energies. From the PKA results that were thereby obtained, three different metrics were defined and calculated, namely, the displacements per atom (dpa), the fraction of self-interstitials and the fraction of vacancies in clusters. For this purpose, the three-dimensional vacancy and self-interstitial distributions corresponding to a given spectrum up to very high recoil energy were obtained, using a database of collision cascades from simulations performed with a hybrid BCA-MD (molecular dynamics) approach [97]. By comparing the metrics obtained for different neutron facilities and those obtained for protons, it emerged that proton damage does not resemble neutron damage. This is due to

the fact that the maximum PKA energy expected under proton irradiation is about 10 keV, whereas PKAs of 1 MeV are expected under neutron irradiation. On the other hand, the BCA calculations showed that self-ion (Fe) irradiation at 5 and 8 MeV produces very similar results to those of neutrons and is therefore more suitable to emulate the neutron damage. Concerning the specific features of heavy ion irradiation, in the case of 5 and 8 MeV self-ions the critical depth below which<5% of implanted self-ions are expected was estimated, as well as the content of self-ions expected below 500 nm. The BCA simulations confirm, thus, that below this depth the content of injected self-ions is negligible, so the microstructure can be characterized with no significant effect expected due to self-interstitial injection, in agreement with the suggestion of Zinkle and Snead [25].

For the simulation of microstructure evolution under irradiation, three OKMC models have been developed. These models are being applied to address different cases of interest for the project using three different computer codes. All of them are based on the same idea, i.e. they describe the evolution of an alloy under irradiation with stochastic events that correspond to the migration and interaction of diffusing species, namely point defects and their clusters or complexes involving point defects and solutes, e.g., vacancy-solute clusters. All these models need as prerequisite the knowledge of a large number of parameters that describe the stability and the mobility of all the defects introduced in the simulation, as well as the reactions between them and with the pre-existing microstructure. In order to define the parameter set, all the relevant information available in the literature and usable as input for the simulations in Fe and Fe-Cr alloys, including carbon, has been collected [98,99].

While sharing principle and parameters, each of the codes has different, and largely complementary, inherent features. The three codes are illustrated in Fig. 7: (a) MEGA-OKMC (Microstructure Evolution GPU-Accelerated OKMC), developed by CIEMAT; (b) MATEO, developed by SCK CEN; and (c) MMonCa, a code developed initially at IMDEA Materials [78] and now being extended by the University of Alicante. The reason for using three codes is that the complexity of the problems to be addressed advises that each issue is first dealt with separately, being it currently not feasible to produce a single, all-including, tool. Nevertheless, the information obtained from calculations with one code can be transferred to the other OKMC codes, in an effective way, having demonstrated that all codes provide the same result when fed with equivalent parameters. An example taken from [100] is provided in Fig. 7**d**.

MEGA-OKMC is based on graphic processing unit (GPU) programming to gain efficiency. It uses a parallelisation algorithm in which the most appropriate time step is found according to the defects that are present in the simulation box, thereby advancing time by steps that are orders of magnitude larger than in standard models [95]. This strongly reduces the number of computational steps that are necessary to reach a given physical time. In particular, it is not limited in space and thus can follow the evolution of defects in large simulation boxes. This is very useful to simulate the evolution of defects in materials irradiated with energetic ions that reach large depths, when compared to the typical length scale of OKMC models. As an example, Fig. 8a shows the implantation profile corresponding to 5 MeV Fe^{+} ions in Fe simulated with the MARLOWE code [101]: as can be seen in Fig. 8a, ions penetrate up to a depth of about 2 μm, which is about 10 times the typical length of volumes simulated with customary OKMC models. Preliminary simulations performed with the MEGA-OKMC code show that simulations with defect accumulation in boxes of 2.28 and 3.43 μm length are possible, as shown in Fig. 8b and 8c. A simulation box of 2.28 μm represents a good compromise between size and computational efficiency. In addition, simulations have been performed in an Fe matrix with different carbon concentrations, exploring also the effect of pulsed vs. continuous irradiation, as well as analyzing the damage profile versus depth and dose,

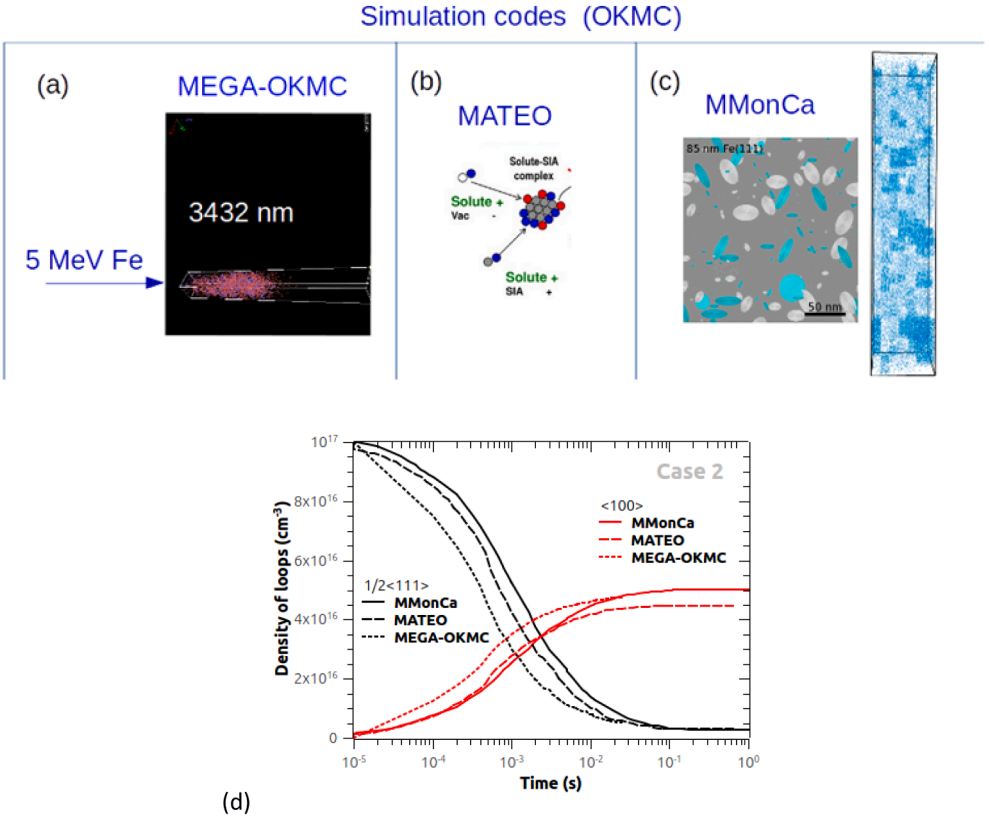

Fig. 7. OKMC codes used in the project (a) Mega-OKMC (b) MATEO (c) MMonCa. (d) shows the time evolution of the distribution of ½⟨111⟩ and ⟨100⟩ loops with the three codes using equivalent parameters (compatibly with the hard-wired differences between codes) and under the same irradiation conditions. For more benchmark results, see [100].

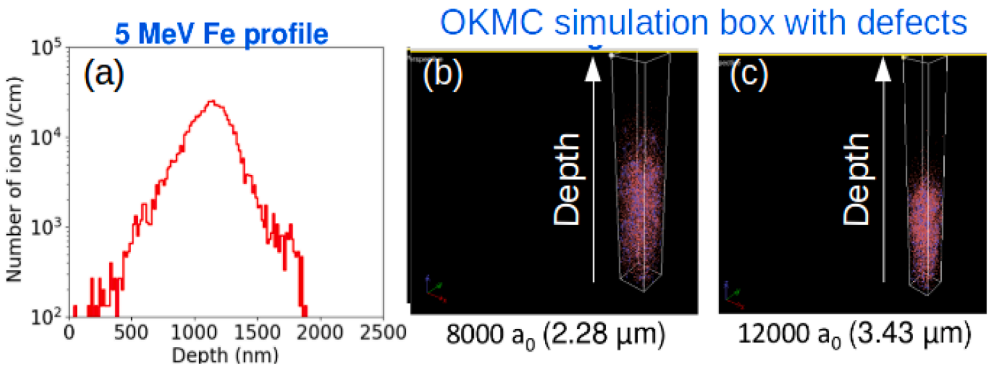

Fig. 8. (a) Depth profile of implanted 5 MeV Fe in Fe as obtained by Marlowe. Mega-OKMC simulation cell with a depth of (b) 2.28 μm and (c) 3.43 μm showing the location of the damage produced by the irradiation.

thereby demonstrating that the code can be used to study the consequences of these ion irradiation features on the microstructure.

The OKMC code MATEO, has the capability of modeling the nucleation and evolution of solute rich clusters, by including explicitly the description of how minor solute atoms are transported by point-defects. Solute-rich clusters are a major and important microstructural feature that is observed in irradiated Fe-Cr-based alloys that contain small concentrations of other solutes [38,39] (see also references in **section 3.1.3**) and are considered responsible for radiation hardening [15]. Thus, even though MATEO is not able to simulate large system sizes like MEGA-OKMC, it allows the evolution under irradiation of chemically complex systems containing small concentrations of solutes such as Cu, Ni, Mn, P or Si to be studied and the results to be directly compared with experimental observations with APT. Key reactions in this OKMC model are the dragging of minor solute atoms by single point defects, and the binding of solute atoms with small loops, which were parameterized based on DFT calculations [102]. In order to be applied to concentrated Fe-Cr alloys, the "grey alloy" approximation is used for the Cr atoms, i.e. the effect of their presence in high concentration is reflected in the parameters used, but Cr atoms are not explicitly described as objects in the model [83–90]. In contrast, all other minor alloying elements are included explicitly. Thus, this OKMC model has been designed to describe the formation under irradiation of vacancy clusters, dislocation loops, and also NiSiP-rich clusters, but it cannot directly predict their Cr content, nor the formation of α' particles. This approximation is a compromise between the current capabilities of the OKMC technique and an explicit description of the formation of solute/point-defect clusters, which allows the results to be used for an assessment of the microstructural features that are expected to mainly cause radiation hardening. As explained below, a description of the redistribution of Cr under irradiation, including formation of α' precipitates, is provided by the cellular OKMC model, which is described next. Concerning dislocation loops, the OKMC model assumes for the moment that all self-interstitial atom (SIA) defects have ½⟨1 1 1⟩ Burgers vectors, although it is known experimentally that a fraction of ⟨1 0 0⟩ loops also exists. This is especially pronounced for pure Fe, because 90% of the loops are ⟨1 0 0⟩ in this case, when the irradiation temperature is high (above 300 °C) [33]. In Fe-9%Cr alloys, however, the observed fraction of ⟨1 0 0⟩ is reduced to 30% [33], which partially justifies the approximation. However, the introduction of this second class of clusters will be the next step. The results of this OKMC model enabled the rationalization of the experimental examination of neutron irradiated Fe-Cr-C alloys by positron annihilation spectroscopy (PAS), small angle neutron scattering (SANS) and TEM, see [102,103]. Thus, the simulation results are discussed jointly with the experimental results in the **section 3.1.3**.

The segregation and precipitation of Cr when present in high concentrations, in the presence of defects produced by the irradiation, are addressed with a different OKMC model, named cellular (Cell) OKMC. This model is implemented in the third OKMC code used in the project, MMonCa. This code also includes long range elastic interactions between loops following the description by Dudarev and co-workers [104–106]. In the Cell-OKMC model the simulation volume is partitioned in cells, each of which has an associated Cr concentration. Defect migration is biased according to the local Cr concentration in a given cell and in the neighbouring ones, following the thermodynamics of the system. It also includes the possible formation of pairs involving a Cr atom and either single vacancies or single self-interstitials. Most work has been devoted so far to calibrating the model for the vacancy-Cr pair, starting also the work on the mixed dumbbell, in order to re-obtain the temperature dependence of transport coefficients as with other, more accurate atomistic methods [55,57], particularly for the vacancy-drag ratio. This method has been tested against experimental results of α' precipitation obtained in [107] for high purity Fe-20 %Cr (40 appm C), thermally aged at 500 °C. Preliminary results of the comparison for two cell sizes are shown in Fig. 9 [108].

3.1.3. Post-irradiation examination of neutron- and ion-irradiated Fe-Cr alloys

Work performed within the FP7-GETMAT [33,34] and the FP7-MatISSE [109] projects showed that three classes of nano-features are responsible for irradiation hardening of Fe-Cr model alloys: (i) clusters of minor solutes or impurities such as Ni, Si and P; (ii) Cr-rich α' precipitates and (iii) the so-called *matrix damage*, interpreted as the clustering of point-defects, eventually growing into dislocation loops or, occasionally, small voids [15,33,37,38,39,103,110,111,112]. The α' precipitates are radiation enhanced nanofeatures that form, consistently with the phase diagram of the Fe-Cr system [49,50], only in Cr supersaturated alloys [37,38,110,113,114]. Minor solute clusters, in contrast, are clearly radiation induced features [37,38,39,112,114,115], which are formed via either self-interstial or vacancy dragging of the impurities and Cr towards immobilized point defect clusters [57,116,117]. C and P atoms are seemingly the main contributors to the formation of immobilized point defect clusters [79,80,81,112,118].

Whereas α' precipitates have a significant contribution to hardening when Cr supersaturation is significant, solute clusters have been shown to contribute importantly to the increase in yield strength, irrespective of the Cr content [15,119]. However, the latter observation was done in fairly complex bainitic/martensitic Fe-Cr alloys with different microstructure depending on the Cr content. In order to verify that the role of minor solutes is actually crucial and to evaluate the role of the different added impurities, the simpler, all fully ferritic G alloys of Table 1, with controlled composition, were fabricated and then neutron-irradiated (see below) [43,109], together with actual 9%Cr steels and a F/M alloy (L252 in Table 1). Their mechanical properties after neutron irradiation were then evaluated [43] and, irrespective of irradiation temperature and Cr content, significant hardening was again observed only in model alloys containing minor solute atoms [43]. The M4F experimental activities in WP2 and WP3 were hence designed in order to

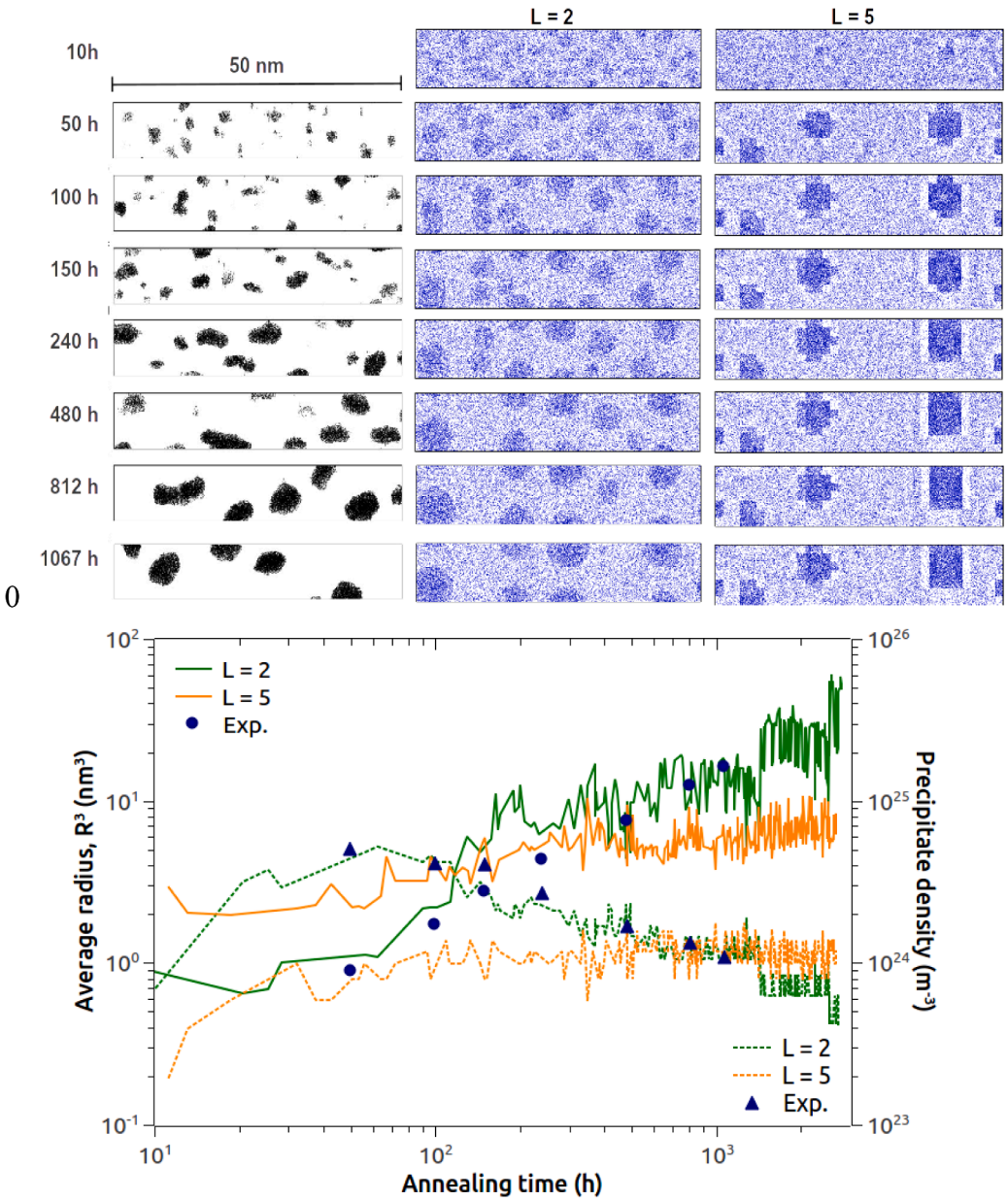

Fig. 9. Cr precipitation evolution as a function of time in Fe-20%Cr for different cell sizes (L = 2 and 5), based on the cell-OKMC method and compared to experimental data from [107]. Upper figure: visual comparison between atom probe reconstructions and Cr concentration maps from the simulation . Lower figure: quantitative analysis of precipitate radius and density in the experiment and in the simulation.

provide a more solid interpretation of these mechanical property results in terms of microstructural features, as well as to provide microstructural data for the development of relevant models: both microstructure evolution models and plasticity models. Concomitantly, the ion irradiation programme was designed to enable the possible effects of corresponding potential artefacts to be studied experimentally and to provide reference cases for models. A variety of microstructural characterization techniques such as PAS, small-angle neutron scattering (SANS), APT, TEM and magnetic after-effect (MAE) have been used to characterize the pristine and irradiated materials.

All materials of Table 1 except three, namely G391, G392 and G393, had been neutron irradiated in the BR2 of SCK CEN to 0.11 dpa at two temperatures (290 °C and 450 °C) in the framework of the FP7-MatISSE project [43,109]. The same alloys, as well as G391, G392 and G393, have been ion-irradiated as part of M4F at the Ion Beam Center of HZDR, with the protocols developed in the running IAEA coordinated research project on Accelerator Simulation and Theoretical Modelling of Radiation Effects – SmoRE II (https://www.iaea.org/projects/crp/t14003). The Fe ion energy was chosen to be either 5 or 8 MeV; the chosen temperatures were 300 °C and 450 °C; and doses of 0.1, 0.5, 1 and 2.5 dpa were reached (the reference dpa corresponded to 500 nm depth for both energy values). These ion energy values were chosen to allow a depth range where potential artefacts are minimised, based on the experience of the researchers involved [27] and in accordance with the recommendations of Zinkle and Snead [25]. The flux was also varied, as well as the way of irradiating, by rastered focused or defocused ion beam. Specifically, x/y raster scanning was performed over a square area of the sample holder that covers all samples included in the corresponding irradiation run. Holders for one to nine samples were available and used to provide the needed total number of samples. The horizontal and vertical frequency of scanning were 1041 and 1015 Hz, respectively. Scanning was performed in such a way that the lateral distribution of fluence was uniform throughout the rastered area. The ion flux (via current) was measured continuously using Faraday cups

and integrated over time to obtain the ion fluence. Not all materials were irradiated at all conditions and with all variations, the detailed conditions for each material are provided in the **Supplementary Material**.

HZDR made a significant effort to minimise an important issue in ion irradiation of Fe and FeCr alloys, i.e. C contamination. This issue is not yet fully solved [31,32]. International projects such as the above mentioned one, SmoRE II, have been launched to gain better insight. Currently it cannot be firmly excluded that the intensity of C contamination may vary from irradiation run to irradiation run, or exhibit spatial and temporal variations within a single irradiation run. However, in M4F a multitude of countermeasures were taken according to the current best practice, such as: plasma cleaning of each specimen immediately before irradiation, in order to remove hydrocarbons from the surface; maintainance of vacuum in the irradiation chamber (recorded range from 1 to $4{\cdot}10^{-7}$ mbar); use of components in the accelerator systems such as analyzing magnets and neutral particle traps. Moreover, in support of the experiment, a C-free Si sample was irradiated using the same setup and characterized on the basis of a combination of Rutherford backscattering spectroscopy (RBS) and nuclear reaction analysis (NRA). NRA measurements were conducted with 1.25 MeV D + ions. RBS was based on the nuclear reaction 12C(d,p0) 13C. The carbon profile was approximated as a three-layer profile and derived by way of fitting the measured NRA and RBS spectra simultaneously, using the NDF V9.6 software. This particular experiment indicated a C concentration of about 10 at% at depths smaller than 14 nm, 0.03 at% at depths between 14 nm and 1.2 μm, and no carbon at larger depths. In conclusion, a near-surface region of 20 nm extension should be avoided or at least taken with care in post-irradiation examinations in M4F.

Both the samples that were neutron-irradiated at 290 °C and the ion-irradiated samples have been examined after irradiation as part of the M4F project (samples that were neutron-irradiated at 450 °C had been already studied as part of FP7/MatISSE), using the already listed variety of microstructural examination techniques (TEM, APT, SANS, PAS, MAE), as well as probing their mechanical properties (tensile tests, hardness, NI). Here, a few preliminary results are overviewed. NI results are reported separately in section 3.2.1.

a) Neutron irradiated materials

Neutron-irradiated materials have been mechanically tested [43] and their microstructure has been studied using PAS and SANS. A few preliminary TEM results exist, while APT is in course. These techniques altogether provide different and complementary information, as amply discussed in [34].

As already mentioned, the hardness measurements and the tensile test results [43] on the model materials from Table 1 (G379, G385, G389, G394 and L252) after neutron-irradiation to 0.1 dpa at 290 °C, revealed clear irradiation hardening only in the ferritic alloys that contain minor solute elements, namely Ni, Si and P. From the microstructural point of view, both PAS and SANS experiments confirm in a consistent way the formation in all ferritic alloys of solute-clusters containing also vacancies [103], thus the latter appear to have a clear role on the former, as summarised in what follows.

Fig. 10 shows the W versus S parameter correlation from Coincidence Doppler Broadening (CDB) PAS for both neutron- (Fig. 10b) and ion- (Fig. 10c) irradiated materials, as compared to the non-irradiated ones (Fig. 10a). The effect of irradiation depends on composition, initial microstructure and also type of irradiation (see below the discussion for the ion irradiated specimens). In all cases the value of the S parameter, which directly correlates to vacancy-type defects, is found to lie between the minimum given by non-irradiated pure Fe and the maximum found for irradiated pure Fe. When comparing with the non-irradiated alloys, S increases in all neutron-irradiated alloys except the F/M Fe-9Cr alloy (L252 in Table 1) and the steels. The largest increase of the S-parameter after neutron irradiation is found for the fully ferritic Fe-9Cr alloy (G385

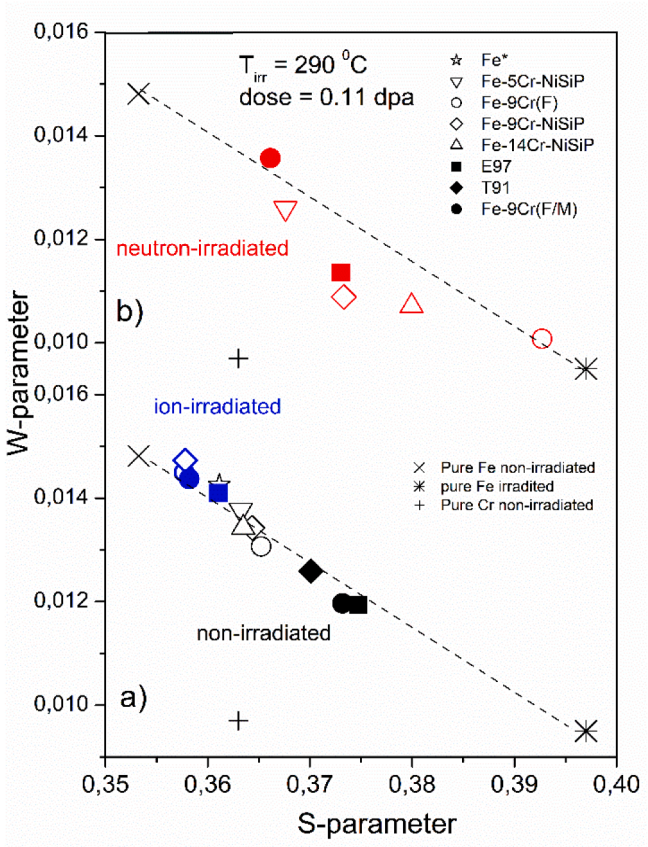

Fig. 10. S versus W parameters of a) ion irradiated and b) neutron irradiated FeCr alloys and steels considered in M4F. The results are compared with existing data of similar materials and steels.

in Table 1). Thus vacancy clusters are the largest in the Fe-9Cr ferritic alloy (though smaller than in irradiated pure Fe), while in alloys containing minor solutes they are smaller. The difference between the F/M and the fully ferritic Fe-9Cr alloys is consistent with the known fact that ferrite develops more easily a void population than martensite [120]. The fact that S is smaller in presence of Ni, Si and P suggests that these solutes hinder the growth of vacancy clusters. In these alloys vacancy clusters are associated with solutes, i.e. vacancy-CrNiSIP clusters form: this is revealed by the significant difference of the W parameter, which acts as signature of positron annihilation with non-valence, thus element-specific, electrons, with respect to pure Fe or Fe-9Cr alloys without minor solute elements: all points lie underneath the line of pure Fe. Thus it can be surmised that the association of solutes with vacancies creates more stable and less mobile complexes, which therefore remain smaller.

The magnetic SANS cross sections are presented in Fig. 11 for the ferritic Fe-9Cr (G385) and Fe-9Cr-NiSiP (G389) alloys; the Fe-9Cr F/M alloy (L252) and the Fe-14Cr-NiSiP (G394) alloys exhibit similar SANS spectra as the Fe-9Cr-NiSiP, thus they are not shown to save space. Increased scattering intensities of the irradiated states are observed for the range $Q > 0.3\,nm^{-1}$ for all materials. The estimated values of the A-ratio, volume fraction, number density and mean size of the scatterers are listed in Table 3. The A-ratio that is observed for ferritic pure Fe-9Cr indicates that the majority of irradiation-induced scatterers are vacancy-containing clusters. Indeed, vacancy clusters in Fe9Cr give rise to a theoretical A-ratio of 1.4 [103,121]. This observation is consistent with the PAS data discussed above. The higher A-ratios of the other four alloys indicate a dominant contribution of solute clusters, especially Cr-rich, α‘ precipitates, the A-ratio of which is typically slightly above 2.0 [36].

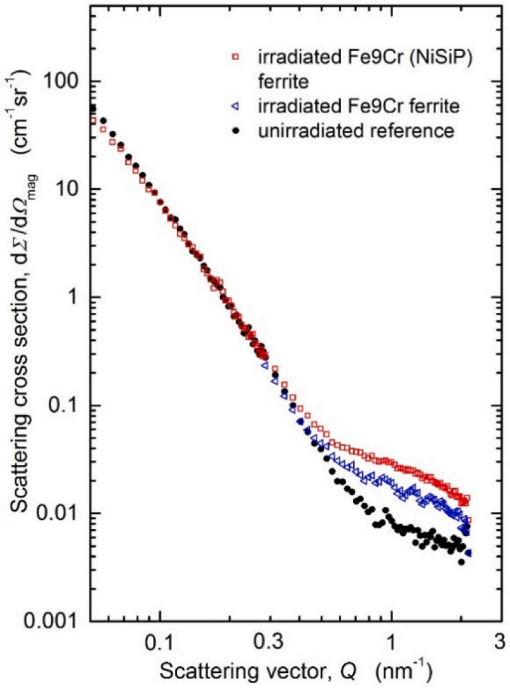

Fig. 11. SANS cross section of non-irradiated and neutron irradiated Fe-9Cr and Fe-9Cr-NiSiP alloys.

Table 3
Scatterer properties derived by SANS: volume fraction c, number density N, mean radius R_{mean}, and A-ratio.

Material	c (vol %)	N (10^{16}cm^3)	R_{mean} (nm)	A-ratio
Fe9CrC F/M (L252)	0.13 ± 0.01	19 ± 4 1.04	1.04 ± 0.07	2.2 ± 0.2
Fe9Cr ferrite (G385)	0.15 ± 0.01	39 ± 8 0.90	1.45 ± 0.1	1.45 ± 0.1
Fe9Cr-NiSiP (G389)	0.29 ± 0.01	69 ± 12	0.95 ± 0.05	1.90 ± 0.15
Fe14Cr-NiSiP (G394)	1.75 ± 0.05	592 ± 76	0.83 ± 0.03	2.15 ± 0.15

The clearly higher volume fraction in Fe-14Cr-NiSiP (G394), combined with the higher A-ratio, provides indeed clear arguments for the presence of Cr-rich α'-phase particles in this alloy, as expected from the Fe-Cr phase diagram. The A-ratio is also high in Fe-9Cr-NiSiP (G389); however, if α'-particles were dominant in Fe9Cr-NiSiP, they should also dominate in Fe-9Cr without solutes, given that α-α‘ demixing is a thermodynamics-driven process; yet, this is not the case. Therefore, it is reasonable to assume that the higher A-ratio in the former alloy is caused by other types of solute clusters, most probably vacancy-CrNiSiP solute clusters [38], consistently with the PAS results. These solute-rich clusters do not form in the same amount, or do not have the same composition, in the 9%Cr alloys with lower or no solute content: Cr will dominate in the latter case, while other solutes will dominate in the former. APT will cast more light on these results.

Most of these experimental microstructural results in neutron-irradiated materials can be rationalized, at least in terms of trends, based on the OKMC model implemented in the MATEO code, using a "grey alloy" approximation for the Cr atoms (all other alloying elements are included explicitly as objects). The OKMC results are summarized in Table 4**.** The comparison with Table 3 cannot be one-to-one, because to start with the "solute clusters" in the OKMC are defined in terms of Ni,Si and P solute atoms only. This happens because the "grey alloy" approximation assumes Cr to be a disturbance to the defect properties, but the atoms of this element are not physically in the system. Thus the OKMC size does not take into account the possible Cr content, whichever its fraction (which SANS cannot measure, although APT will likely clarify this point). The model, therefore, can also not describe and predict α-α´ demixing (this can be done with Mmonca, though [108], which does not include, however, minor solutes). Thus the comparison with 14%Cr should be ideally made by subtracting the density of α´ precipitates from the total, something that SANS also does not allow, as it does not distinguish between different types of scatterers (APT data will help in this respect, as well). The OKMC model predicts three kinds of defects that involve solutes: (a) those with vacancies and solutes; (b) those with self-interstitial atoms and solutes; (c) those without point-defects, but only solutes. All of these can be scatterers that are "seen' by SANS, provided their radius is sufficiently large (above 0.5 nm). In principle there could be also point-defect clusters without solutes, but in practice in alloys this is extremely unlikely and, assuming it happens, they shall be only small clusters, below the resolution of SANS, therefore they should not be added to the total of scatterers. In Table 4 the three categories of solute-containing clusters from the OKMC are put together and defined as "scatterers" (*scat*), without distinguishing between the type of point-defects they contain (and excluding α´). Table 4 also reports about the vacancy clusters (irrespective of their solute content), because these compare with PAS results: all of them are very small in terms of number of vacancies per defect, thus they are invisible to SANS, but they are in the range of sensitivity for PAS.

Table 4
Defect properties derived by OKMC: f_{vac} is the atomic fraction of vacancies, which roughly correlates (non-linearly) with the S parameters; n_{vac} is the average number of vacancies per cluster; N_{scat} is the number density of scatterers; R_{scat} is the mean scatterer radius (not accounting for Cr and α‘ precipitates). The different microstructure (F/M versus ferritic) is represented in the model by a different grain size and carbon content.

Material	f_{vac} (appm)	n_{vac} (vac/cluster)	$N_{scat} \times 10^{16}$cm^3	R_{scat} (nm)
Fe9CrC F/M	5.7	1.9	None with $R_{scat} > 0.5$ nm	None with $R_{scat} > 0.5$ nm
Fe9Cr ferritic	142	9.8	3.4	0.76
Fe9Cr (NiSiP) ferritic	39.8	2.0	48	0.93
Fe14Cr (NiSiP) ferritic	43.4	2.1	34	0.94

Despite the different types of snapshots taken by experiments and OKMC, the model results are consistent with the PAS data of Fig. 10: the vacancy fraction is the highest in Fe-9Cr ferritic, the lowest in Fe9CrC F/M and intermediate in the ferritic alloys with solutes. Accordingly, the largest vacancy clusters are formed in the Fe-9Cr ferritic alloy. The low fraction of vacancies in Fe9CrC F/M is largely the result of simulating this alloy with higher sink strength than in the case of the ferritic alloys, reflecting the much higher denstiy of absorbing boundaries (laths, blocks, packets, …), and with a higher carbon content. This leads, however, to the formation in the model of very small solute clusters, below the SANS radar, which is clearly a shortcoming: the scatterer population in the F/M alloy, therefore, cannot be compared with SANS data. In the ferritic alloys, however, the trend is correct: the density is smaller in the Fe-9Cr alloy and higher in the other two, but smaller than the SANS numbers because α´ precipitates are not accounted for by the model. The calculated mean solute cluster radius is around 1 nm, in good agreement with the SANS results. These defects contribute to hardening: solute clusters associated with point-defects are the main hardening elements, while small voids and α´ precipitates contribute significantly less than the solute clusters [103,119]. The model reinforces the notion that solute clusters are formed by segregation of solutes at point-defect clusters, dragged there by single point-defects [117].

In addition to vacancy-related defects, interstitial dislocation loops were clearly observed by TEM to be present in all irradiated materials. Numerous small loops characterized the Fe-9Cr alloy, often decorating

dislocation lines, but regions with homogeneous loop distributions were observed as well. In the case of Fe-9Cr-NiSiP, in contrast, the vast majority of the loops was found to decorate dislocation lines. The areal density of the loops observed in the Fe-9Cr-NiSiP alloy was evidently lower than in Fe-9Cr, which may imply that the presence of minor solutes reduces both loop and vacancy cluster size alike. These loops also contribute to hardening. However, the SIA loop density and size distribution in the OKMC model deviate from the experimental evidence, see Fig. 12: density and size are both underestimated in the F/M alloy irradiated at 450 °C. This may be due to the fact that the model does not include explicitly the presence of dislocations as sinks: instead, homogeneously distributed spherical absorbers are introduced, which of course prevent the description of heterogeneous loop distribution. Another strong approximation is the inclusion in the model of a single family of dislocation loops, namely those with Burgers vector $a_0/2\langle 1\,1\,1\rangle$, instead of two types, i.e. including also the loops with Burgers vector $a_0\langle 1\,0\,0\rangle$. These two families of loops are known to exhibit very different mobility, but the relative importance of the mechanisms whereby the latter family forms is not simple to quantify [82,98].

b) Ion irradiated materials

The ion irradiated materials have been studied from the microstructural point of view using PAS, MAE and, partially, APT. TEM is also in course. For the complementarity between these techniques, see [34]. Because of the still only partial post-irradiation examination results that have been reported and are available, it is currently not possible, yet, to provide a complete and consistent picture of the microstructural examination results, of which only a few are here sketched.

Fig. 10 shows the W versus S parameter correlation from CDB PAS also for the materials that were ion-irradiated to 0.1 dpa at 290 °C (lower side), thus under conditions comparable to neutrons, except of course for all the specificities of ion irradiation. These correspond especially to higher dpa/rate, as all other artefacts were minimized with the choice of the energy and the depth from which specimens were lifted, while C contamination was under control, as much as reasonably possible. Ion irradiation seems to produce no increase of the S parameter in any of the alloys or steels. In fact, both the S and W parameters after ion irradiation exhibit values that are closer to pure unirradiated Fe than to the as-received non-irradiated alloys and steels. It is possible, however, that these results, rather than reflecting the nature of the defects that were created by irradiation, reflect the fact that ion irradiation concerns very small volumes, which may be too small to provide sufficient statistics in PAS measurements performed with bulk methods, i.e. without using a positron beam. This is one of the important differences between ion and neutron irradiat ion, i,e, that beyond the different type of microstructure they produce, bulk chearacterization methods are not generally applicable to ion irradiated specimens, as mentioned in the introduction.

MAE measurements were also performed on the FeCr alloys and steels after ion-irradiation to 0.1 dpa at 290 °C and compared with the non-irradiated materials. The spectra, corresponding to alternate current (AC) susceptibility, are presented in Fig. 13. Significant differences between irradiated and non-irradiated conditions are observed in the α-Fe sample, which exhibits a clear increase of the Snoek relaxation peak (<300 K) after irradiation. This is accompanied by the decrease of its activation energy (the peak position shifts to lower temperatures). In addition, some redistribution of carbon associated with dislocations occurs, as revealed by the change of 400 K relaxation peak. These effects may originate from limited injection of additional carbon during ion irradiation experiments. In addition, it should be taken into account that the interpretation of the evolution of these peaks is often partly speculative. In the Fe-Cr samples, in contrast, there are either no differences between non-irradiated and irradiated samples, e.g. in Fe9Cr and Fe9CrNiSiP alloys, or there are modest reductions of the 800 K peak in irradiated F/M Fe9Cr and E97 [122]. This absence of difference is as yet unexplained.

APT was used to characterize solute clusters in the Fe-9Cr-NiSiP alloy, ion-irradiated under the same conditions as with neutrons, i.e. 0.11 dpa at 300 °C. An example of chemical reconstruction maps is given in Fig. 14. At this low dose only P clustering is clearly detected, while there is no visible sign of clustering of Ni and Si on the 3D images, although statistical treatments revealed clustering of these species together with P.

Even though doubts about the capability of some techniques, e.g. CDB PAS, to unambiguously detect damage in ion irradiated materials exist, because of the limited volume of material that is affected, overall these results seem to suggest that ion irradiation to low dose, perhaps because of the higher dose rate, is less effective than neutron irradiation in producing radiation damage, at least vacancy and solute clusters, at the same dose and temperature. MAE studies, in addition, reveal a different behaviour between Fe and Fe-9%Cr alloys. These results will be further rationalized with the help of models that are under development, analyses that are still in course and new results that are being produced.

APT characterization is being performed also on samples of other alloys that were irradiated with ions to higher dose than 0.1 dpa, namely 0.5 and also 2.5 dpa. Fig. 15 shows an example of preliminary results for 0.5 dpa. In this case, Cr rich clusters (red) and NiSiPCr clusters (blue) can be clearly identified and their density and size compared for different irradiation conditions, namely: two different energy values (8 MeV and 5 MeV) and defocused vs. rastered beam. Preliminary results seem to indicate that beam focusing and rastering do not have a significant effect on Cr-rich cluster concentration or size and only have a small influence on solute rich clusters (SRC), which exhibit lower Ni and Si enrichment for defocused beam and slight number density reduction with similar size. Thus defocusing without rastering would have a negligible effect in terms of radiation damage. Flux, in contrast, seems to have an important contribution, consistently with the comparison with neutrons. At low flux, Cr-rich clusters increase in number density while keeping a constant size. In contrast, SRCs decrease in number density and increase in size. Note, however, that the irradiation energy was also

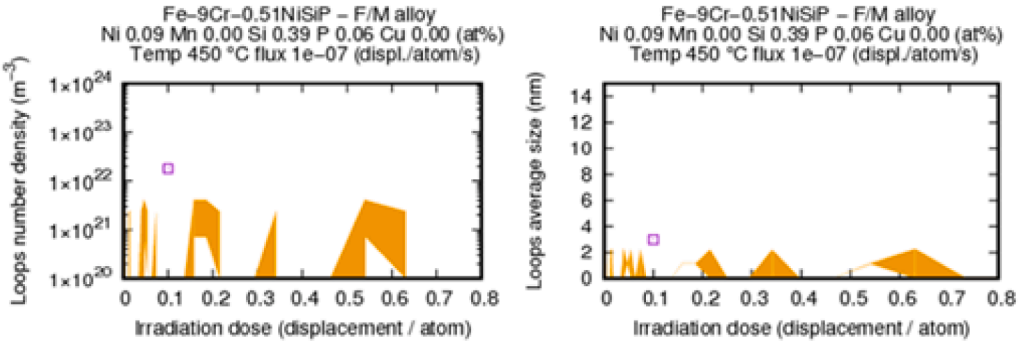

Fig. 12. Loop density and size in the Fe-9Cr-NiSiP ferritic alloy at 450 °C as a function of dose according to OKMC simulations (gold ranges) and according to experiments (empty squares).

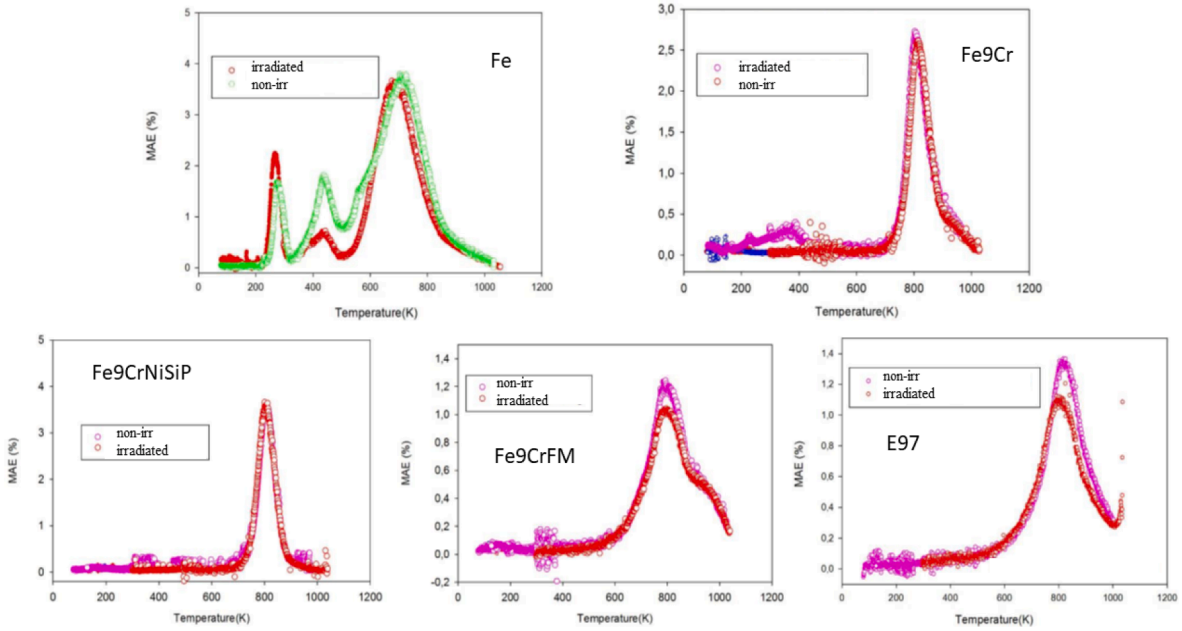

Fig. 13. AC susceptibility/Magnetic After-Effect measurements on 9%Cr alloys and Fe, both non-irradiated and irradiated.

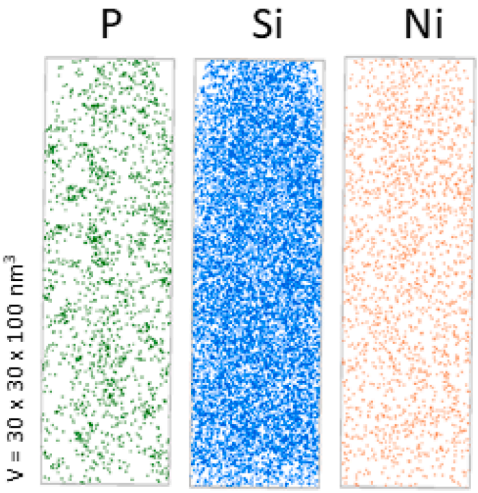

Fig. 14. APT data of ion-irradiated (0.1 dpa, 300 °C, @500 nm depth) Fe-9Cr-NiSiP alloys, see text and [112] for details.

different, which may have an influence, as well. Studies were also conducted to highlight the possible synergy between different impurities, i.e. Si, Ni and P, together with C when detected (whichever its origin), in the formation of SRC, by examining the alloys with only one minor solute added at a time, or the three of them together. This study showed that P is the fastest diffuser regarding the formation of the solute-rich clusters. P segregation in clusters saturates between 0.1 and 0.5 dpa, but no synergistic effects between Ni, Si and P are observed up to 0.1 dpa [112]. At higher dose, the influence of P on Ni segregation has been shown, confirming the major role of P on the nucleation process of SRCs.

3.2. Deformation after irradiation

3.2.1. Nanoindentation modelling and experiments

Notwithstanding its limitations in capturing irradiation embrittlement, nanoindentation is a method of choice when it comes to the assessment of irradiation hardening, in particular for self-ion irradiation resulting in shallow damage profiles with penetration depths on the order of 1 μm only. However, while irradiation-induced hardness changes are readily detected, their quantitative interpretation is rendered difficult by the non-uniformity of the damage profile and the fact that the plastic zone created under the indenter may well extend beyond the Bragg peak and, hence, be affected by the mechanical properties of the unirradiated material. The observed effective hardness then represents a convolution of the local hardness vs. depth profile. Nanoindentation hardness is also affected by indentation size effects [123], which in turn will be subjected to irradiation-induced microstructural changes. The same is true for the propensity of a material to pile up at the edges of the indent: as irradiation hardening goes along with decreased strain hardening rate, increased pile-up formation results, which introduces additional bias in assessing irradiation-induced hardness changes. It is therefore important to note the specific limitations for the derivation of irradiation-induced mechanical property changes using nanoindentation testing that come on top of the generic limitations for the use of self-ion irradiation as a fast and convenient means to (try to) emulate neutron irradiation-induced microstructures and damage. As mentioned, there are limitations due to different cascade sizes resulting from different recoil energy spectra, the effect of strongly increased displacement damage rates, the implantation of self-interstitial atoms, and the occurrence of near-surface defect-denuded zones followed by inhomogeneous damage profiles of limited depth [25].

In the above context, the activities on nanoindentation within the project covered a wide spectrum, ranging from modelling to experiments, with a view to establishing harmonized methods of measurement and analysis:

- Exploration of the use of step-wise MD simulations of nanoindentation to provide useful information for upper scale models.
- Establishment of approaches for strain gradient and crystal plasticity finite element models of nanoindentation processes, accounting for indentation size effects and able to incorporate the effects of irradiation damage.
- Optimisation of surface preparation of Fe (G379 in Table 1), Fe-9Cr (G385 in Table 1) and Eurofer97 for nanoindentation testing. It is important to note that the surface preparation of ion-irradiated

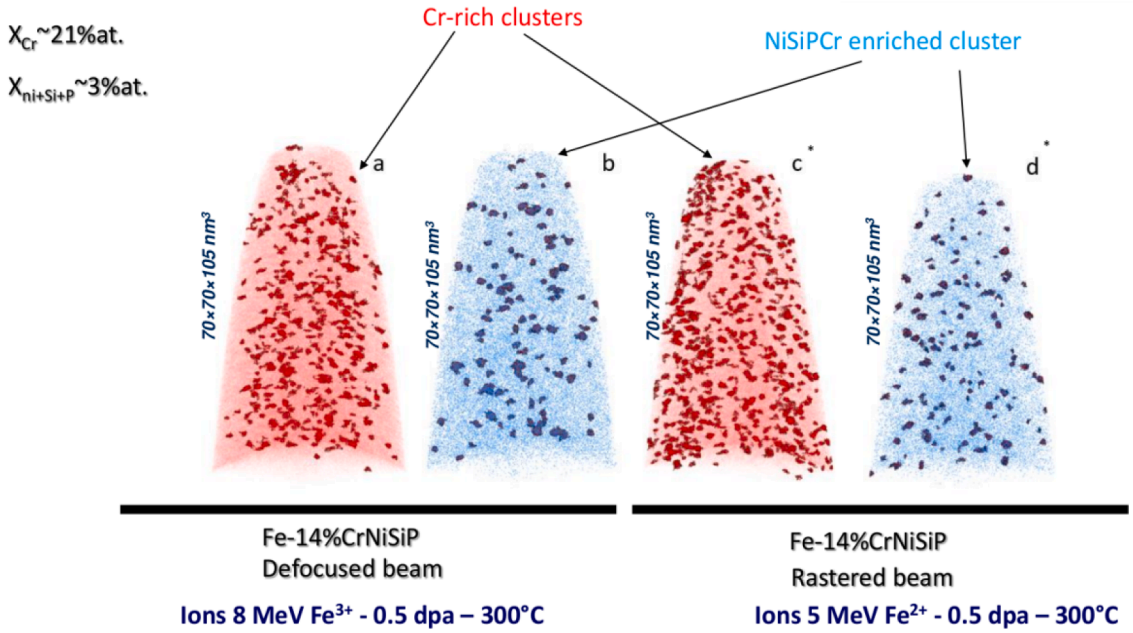

Fig. 15. APT results for two different irradiation conditions: (left) 8 MeV Fe and defocused beam (right) 5 MeV Fe and rastered beam, both to 0.5 dpa.

samples has to be performed prior to ion irradiation and cannot be modified after ion irradiation.

- Execution of nanoindentation testing on pure Fe (G379 in Table 1), Fe-9Cr (G385 in Table 1) and Eurofer97, irradiated with 5 MeV Fe^{2+} ions at 300 °C and 450 °C, up to 0.1 and 1 dpa.
- Development of a methodology to derive information on radiation effects from nanoindentation curves, using mechanically deformed Fe as a proxy and supported by optimized nanoindentation testing protocols and TEM analyses of the as-irradiated and as-indented materials.

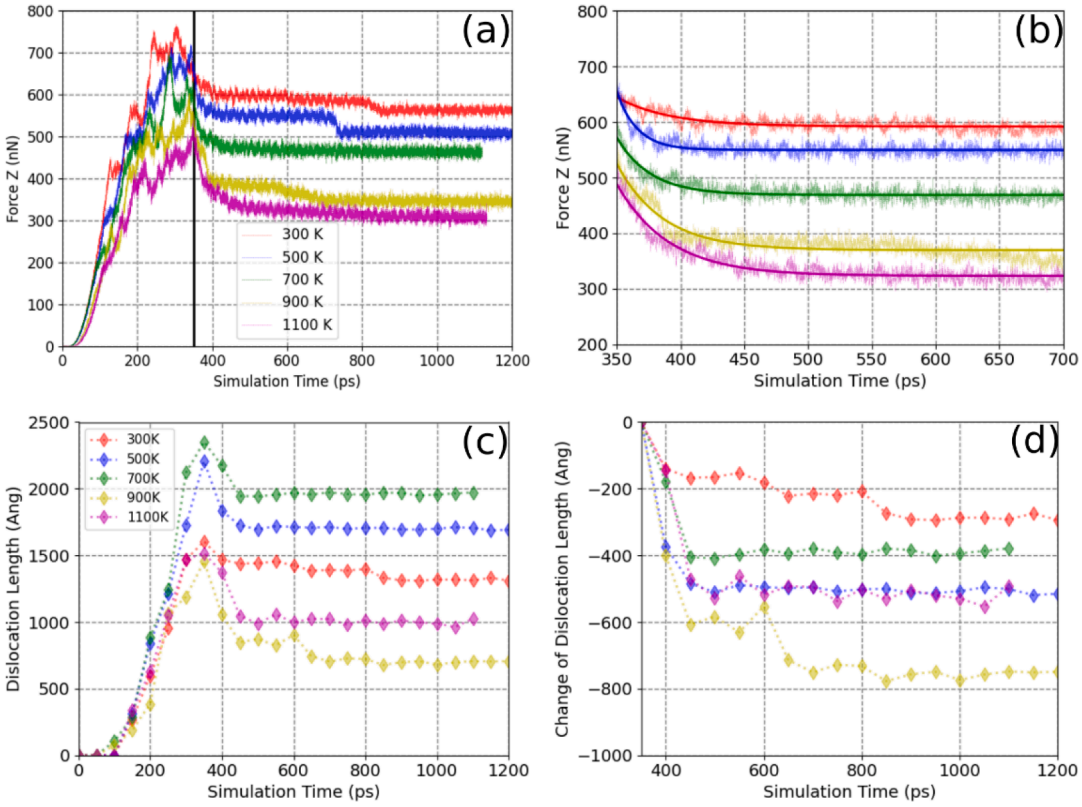

Fig. 16. (a) Force on the indenter as a function of the simulation time at different temperatures. The vertical line shows the point where the indenter was stopped. (b) Same as (a) but only showing the beginning of the relaxation. (c) Total dislocation length during the simulation. (d) Change of the total dislocation length in the relaxation phase.

- Collection of datasets in an engineering materials database and an interoperable nanoindentation test data format developed within the framework of a CEN Workshop (see Appendix).

As regards the numerical modelling, molecular dynamics (MD) simulations of indentation of pure Fe samples were performed on virtual samples where defects were introduced applying the "random atomic displacements and annealing' (RADA) scheme, according to which atoms are randomly displaced to generate Frenkel pairs, after which the system is annealed. In the annealing phase point defects evolve into dislocation loops and self-interstitial and vacancy clusters. Previously this was also done in Fe-9Cr [124]. The resulting force-depth curves did not show any effect that could be unambiguously related with the presence of defects, similarly to the case of the alloy. The possibility of using the step-wise indentation in MD simulations was then further studied. In this scenario, indentation was first performed with a constant speed, followed by a relaxation stage in which the indenter is not moved. In Fig. 16 we see the results of a single indent-relax cycle. Here, we used for Fe-Cr the two-band embedded atom method (2B-EAM) potential developed by Bonny *et al.* [125]. The Fe-C and Cr-C interactions, which were used to describe the interaction of the indenter with the alloy, were purely repulsive and obtained from the Ziegler-Biersack-Littmark (ZBL) potential [40]. We constructed a simulation cell consisting of 4,500,000 atoms in bcc lattice (~430 Å × 430 Å × 290 Å in xyz side-length) and used an indenter with a diameter of 71 Å in rigid diamond carbon. First, the indenter was lowered with a constant speed of 0.1 Å/ps, after which it was stopped and the system was allowed to relax. Simulations were performed in the temperature range between 300 and 1100 K. The relaxation time was not found to depend strongly on temperature. Also, the indenter force and the total length of dislocations seemed to settle to a constant value during the 1 ns relaxation period. The incipient plasticity data in the form of force-depth curves obtained from MD simulations are being compared with those obtained from Finite Element Modelling (FEM) simulation, based on the MD simulation of compression stress–strain data. By using the step-wise indentation it might be possible to reach longer effective time scales (i.e. smaller strain rates) in MD simulation of NI. Thus, the aim of ongoing work is to determine whether it is possible to get similar size dependence of hardness at the nanometer scale.

Work is underway for the implementation of a FEM crystal plasticity (CP) approach to model the nanoindentation load–displacement based on the true stress–true strain curves otherwise derived from the tensile tests. A model is being developed to introduce flexible CP laws, such that the effect of neutron irradiation and the interaction between the plastic deformation and neutron irradiation defects (under progressive plastic deformation) can be accounted for. The Berkovich and spherical nanoindentation experiments have shown that the Eurofer97 samples display indentation size effect. The spherical NI load–displacement curves that were derived following the Pathak-Weaver approach [126] show a strong dependence on the tip curvature. The indentation size effect is taken into account in these FEM simulations by using a strain gradient plasticity model with a proper scaling factor. An approach following the work of Martínez-Pañeda and Betegón [127] has been adopted. This approach is based on conventional theory of mechanism-based strain-gradient plasticity and has been implemented in the Abaqus code. The calculations performed have shown that the scaling factor adopts a value around 1 μm. This value yields a decent compatibility of indentation stress–strain curves at different values of tip radius from 1 μm to 5 μm. The influence of the experimental uncertainties such as surface roughness, surface detection procedure and its influence on zero-point determination and coefficient of friction between the tip and the test material is considered.

Furthermore, methodologies to generate local stress–strain curves from spherical nanoindentation data and infer tensile equivalent properties of steels have been assessed [128]. Key points for the construction of indentation stress–strain curves are the determination of contact radius and the definition of strain, for which it was concluded that Tabor's equations and the geometrical definition of the contact radius performed best in extracting indentation stress–strain curves [128].

Work is also underway to underpin a final indentation protocol and analysis method to identify different types of irradiation damage on the nanoindentation curves and allow for the known interaction between the indentation size and other length scales that exist in materials (grain size and defect density amongst others) [129]. Key issues have been identified. It is important to:

- Achieve sample surfaces prepared in a manner that does not change their mechanical properties. This means careful removal of the previous work hardened layer in each stage of polishing and a final polish that is either chemo-mechanical or electro-polishing to remove the final mechanical damage layer;
- Know or measure the existence or generation of residual stresses and/or pile-up;
- Select an indentation cycle that optimises the determination of the contact stiffness and minimizes the effect of creep on the force removal gradient;
- Understand the effect on hardness of the total amount of indentation creep that is allowed;
- Understand and exploit the fact that the measured amount of indentation size effect is dependent on the combination of length scales in the material and in the test.

Methods to quantify the offset in results caused by residual stress and/or pile up formation have been investigated using the measured stiffness and a reference elastic modulus value. The effect of calibration, creep and other sources of instrumental or methodological bias have also been investigated, see Fig. 17. Fe tensile specimens strained to 15 % engineering strain at room temperature, 125 °C and 300 °C have been analysed by nanoindentation and TEM [130]. Results are currently being extended using newer, optimized indentation cycles. Pre-strained specimens exhibited higher hardness as compared to the non-strained counterpart due to dislocation multiplications during straining, but creep rates vary and affect the hardness values obtained. Differences in pile-up and residual stress are also being investigated. The focus is now on optimizing the correction of hardness data using elastic modulus [130,131] and the procedures to fit data sets to semi-empirical models, so as to obtain the relationship between the derived fitting parameters and the involved length scales due to the test size (a combination of indent size and indenter geometry), the microstructure, and the damage density.

Nanoindentation tests have been performed in four different ferritic/martensitic materials: the Eurofer97 steel, the Fe-9Cr model alloy with ferritic microstructure (G385 in Table 1), the Fe-9Cr model alloy with more complex martensitic–ferritic-bainitic microstructure (L252 in Table 1) and pure Fe (G379 in Table 1). Berkovich and spherical nanoindentations have been carried out on the non-irradiated materials and in the materials irradiated with the following conditions:

- Fe^{2+} self-ions at 5 MeV and the following temperatures and doses:
  - o RT, 1 dpa
  - o 300 °C, 0.1 dpa
  - o 300 °C, 1 dpa
  - o 450 °C, 0.1 dpa
  - o 450 °C, 1 dpa

Neutron-irradiated ferritic Fe-9Cr (G385 in Table 1) has been characterized, as well, using a Berkovich indenter and applying continuous stiffness measurements. A protocol to optimize surface preparation of the neutron-irradiated samples has been developed, with the aim of obtaining a surface finish similar to the ion-irradiated materials. The nanoindentation response of unirradiated, and ion- and neutron-irradiated materials is presented in Fig. 18. The Nix-Gao plot on the

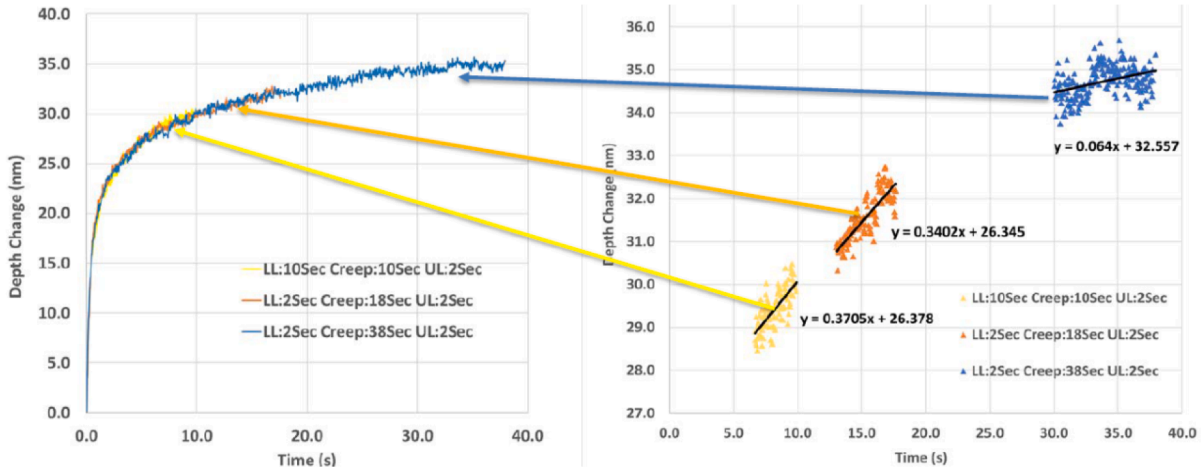

Fig. 17. Plot of indentation depth into mechanically strained Fe vs. time at a constant force. This shows the variation of indentation creep rate at the end of different selected holding times. A hold at maximum indentation force is used to reduce the error in the measured unloading stiffness (and so Indentation Modulus) by reducing the creep rate during force removal in NI experiments (ISO14577).

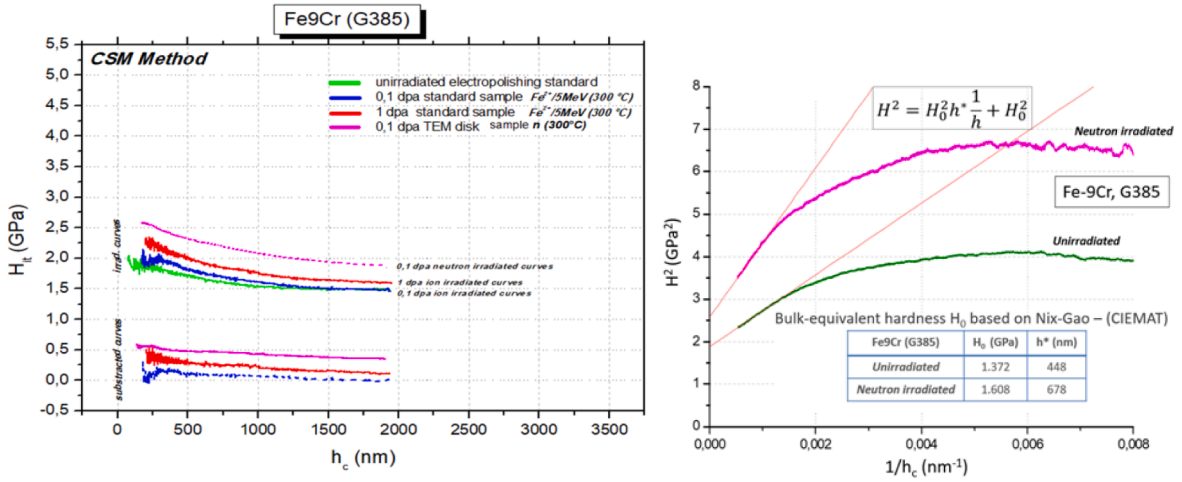

Fe9Cr (G385)	H_0 (GPa)	h* (nm)
Unirradiated	1.372	448
Neutron irradiated	1.608	678

Fig. 18. Continuous stiffness measurement results for Fe9Cr samples and irradiation hardening by the Nix-Gao approach [123].

right-hand side indicates a possibility to derive the bulk-equivalent hardness, also for neutron irradiated specimens, which is not granted *a priori*. Indeed, the measured neutron-irradiation-induced increase of the bulk-equivalent indentation hardness, $\Delta H_0 = 0.24$ GPa, converted to Vickers-hardness increase (22HV10) agrees well with the measured Vickers-hardness increase of 22 ± 3 HV10 [103]. A comparable procedure for ion-irradiated materials is not yet available at this stage for several reasons mentioned at the beginning of this section, notably the effects of steep damage gradients and injected self-interstitials. It is important to note that the indentation response for the ion-irradiated samples integrates over the plastic zone, which extends into depth regions exposed to different levels of displacement damage. Further results of this NI characterization work are reported in references [132–135]. In particular, a methodology to separate the effects of injected interstitials and displacement damage for ion-irradiated materials was introduced in [133]. Ongoing work in this field is tackling the specifics for ion-irradiated materials and is expected to be one of the final achievements of the project.

3.2.2. *Deformation mechanisms at the grain scale*

As mentioned, the complete understanding of plastic flow localization involves mechanisms that occur at scales ranging from the atomic-level, to dislocation, crystal and eventually polycrystal scales. It is conceptually accepted that the origin of this phenomenon are reactions between mobile dislocations gliding along a slip plane and irradiation defects, which lead to different mechanisms of removal of the latter. The specific reactions depend on the one hand on the character of the gliding dislocations and on the other on the features of the irradiation defects. In bcc metals the only type of defects that are more or less easily absorbed by dislocations are prismatic dislocation loops, which have generally their origin in the clustering of self-interstitial atoms created by irradiation. More difficult, though not *a priori* impossible, is the absorption of other types of defects. Thanks to MD simulations [136–147], much is known about the mechanisms of defect absorption by gliding dislocations, at least in pure Fe [136–142] and, to some extent, in Fe-Cr [144–146] and also in Fe-C [143,147]. However, little is known about these same mechanisms in complex alloys, for example in the presence of, simultaneously, substitutional solutes such as Cr, and interstitial ones such as C, which are both found to decorate loops. Large scale simulations provide an idea of the collective behaviour of gliding loops and clouds of irradiation defects, thereby reproducing the nucleation of channels in Cu [148], to be compared with experimental in-situ studies [149], as well as in Fe [150], or more recently using approaches of wider applicability [151], while the multiscale approach proposed by Cui et al. [152] seems promising in the simulation of channelling beyond nucleation. The goal to achieve better precision should be to simulate this at

single crystal level, by using detailed discrete dislocation dynamics (DDD) approaches, which can treat the interaction of dislocation segments with irradiation defects, for instance using a nodal code such as NUMODIS. [153]. However, simulations of this type are very time-consuming and require handling numerous parameters, among which a detailed description of the interaction of the dislocation segments with every possible radiation defect, while describing correctly the mobility of the dislocation segments, thus it is crucial to both pursue methods to accelerate the computation and identify generalized methods to describe dislocation mobility including the effect of the interaction with defects. Ideally, then, a reliable description of dislocation channel nucleation and evolution inside one grain should be brought to the level of continuum models, as a step towards the study of aggregates. In addition, in order to step to the polycrystal, one should know how dislocations and their pileups interact with grain boundaries, to assess the possibility that channels are transmitted through boundaries. Only very few examples of studies of the latter type existed before the project. In this framework, the activities that are being carried out in the project are listed in what follows. The target material, both for the simulations and in the experimental activities, is the ferritic Fe-9%Cr alloy (G385 in Table 1), with comparatively small C content.

1. Use MD with suitable interatomic potentials to study atomic-scale processes that are relevant to plasticity in irradiated steels, including the simultaneous effect of C and Cr solutes on dislocations and dislocation loops, as well as the interaction of dislocations with grain boundaries.
2. Improve the efficiency of DDD simulations, by developing an adapted framework to include irradiation defects and by accelerating the calculation of the elastic fields through DDD / fast Fourier transform algorithm coupling.
3. Model crystal plasticity at the single grain level as a continuum, using a strain gradient plasticity approach, as well as a micro-model to be developed based on DDD simulations, accounting for dislocation/defect interactions and cross-slip.
4. Perform in-situ straining experiments in irradiated and pristine samples, in order to study the interaction between dislocations and irradiation defects and compare the observations with DDD simulations, but especially to derive quantitative features concerning shear bands and dislocation channels: width, length and thickness, as well as inter-channel spacing and strain inside them.

a) Molecular dynamics studies

The density functional tight binding (DFTB) method, an approximate density functional theory (DFT) approach, has been investigated as a way to model dislocations in iron and its alloys. The freely available dftb + code (http://www.dftbplus.org) was used. A new parametrization of DFTB for bulk bcc iron was developed, which provided much better elastic constants and lattice parameter than the previous one, as is shown in Table 5, as well as providing information about magnetization and electronic band structure.

The new parametrization was then used to model the core of a dislocation in pure iron and in presence of carbon interstitials, as shown in Fig. 19. However, even if DFTB is much less computationally expensive than DFT, this method remains significantly expensive. It is estimated that, with current computational resources, it remains difficult to simulate systems with >5,000 atoms, which is not enough to model the full 3D migration process of a dislocation in bulk iron. Thus in practice, despite its promises, this method did not prove suitable to extensively study dislocation properties in Fe-Cr-C, in replacement of interatomic potentials and with a view to obtaining more reliable results.

Table 5
Improvement of the DFTB prameterization: comparison of lattice parameter (a_0), bulk modulus (B) and elastic constants (C_{ij}) in experiments and calculated using different methods (standard DFT and DFTB).

Method	a_0	B	C_{11}	C_{12}	C_{44}
Experimental	2.87	168	234	136	116
DFT(VASP)	2.83	209	257	185	93
DFTB (old)	2.93	400	567	317	157
DFTB (new)	2.83	180	247	146	121

In parallel, the combined effect of C and Cr enrichment of loops on the hardening of Fe-Cr-C alloys is being investigated by studying the atomic scale interaction mechanism between dislocation and C/Cr decorated loops using empirical interatomic potentials. The task goes through three steps: (i) DFT computations have been performed to characterize the interaction between C, Cr and point defects [155]); (ii) an EAM-type ternary Fe-Cr-C interatomic potential compatible with the LAMMPS code has been fitted to the DFT data; (iii) large scale MD simulations are being carried out, employing the interatomic potential, to characterize the interaction between a dislocation line and (decorated) loop, see an example in Fig. 20 from previous similar work [156,157]. Specifically, the effect of C and Cr enrichment, and their combination, on the absorption of square ⟨1 0 0⟩ loops is being studied. Interactions of the loop in three non-equivalent orientations with an edge dislocation are being investigated. Conditions consistent with the experimental TEM observations for ion irradiation at 300 °C for 0.5 dpa are being selected. Loops of size 1–5 nm are being studied with an interspacing of 22 and 44 nm, which corresponds to a loop number density of ~ 1–8 × 10^{22} m^{-3}. The position of the loop compared to the dislocation slip plane was chosen to promote full absorption of the loop when the simulation is done in pure Fe. In this way, a clear effect of C and/or Cr can be observed. The main preliminary conclusions are that the combination C + Cr slightly hinders loop absorption and increases the obstacle strength, but no synergy between C and Cr has been observed so far. These types of effects need to be taken into account in the parameterization of detailed dislocation dynamics simulations that, such as in the case of the code NUMODIS, can reproduce in detail the processes of absorption of loops by gliding dislocations [153]. However, since DDD simulations do not contain any explicit chemical information, this can mainly be done implicitly, through some sort of calibration that still needs to be applied.

MD simulations are also applied to study the interaction of dislocations with three different ⟨1 1 0⟩ tilt grain boundaries (GB) and a ⟨1 0 0⟩ tilt-GB in α-Fe [158]. The GBs that have been considered are: (1) Σ3(1 1 2) < 1–10 > and vicinal to GB112, (2) Σ11(3 3 2) < 1–10 > and (3) Σ5(3 1 0) ⟨1 0 0⟩ . Two calculation methods have been used: MD and a hybrid continuum-atomistic model [159], the latter was modified to include all dislocation types. Each GB has been fully characterized by studying all the potential dislocation-GB interactions, for all possible combinations of Burgers vector orientations and dislocation character (edge or mixed). Considering the case of a single dislocation-GB interaction, the only observed outcome at all temperatures is absorption, leading to the creation of a GB dislocation (GBD), along with the emission of disconnections. When dislocation pile-up-GB interaction is considered, the reaction mainly observed at all temperatures is also dislocation absorption, although for GB112 transmission and reflection under specific conditions could be observed, as well. Even if absorption is essentially the only reaction observed, in terms of plasticity the outcome of the reaction is strongly dependent on the interface that is considered. In the GB112 a source of disconnections is created, which enhances shear-coupled GB migration, while for GB332 the outcome depends on the combination of incidence angle and Burgers vector [160]. For a low incidence angle, a GBD with a facet that steps the interface is created and every dislocation absorbed increases the height of the step. In contrast, for a high incidence angle we observed the creation of a seed for stress-induced twin growth. The appearance of the (1 1 2) twin is an efficient way to accommodate the stress at the interaction region of the GB. The twin grows by the pile-up of the glissile

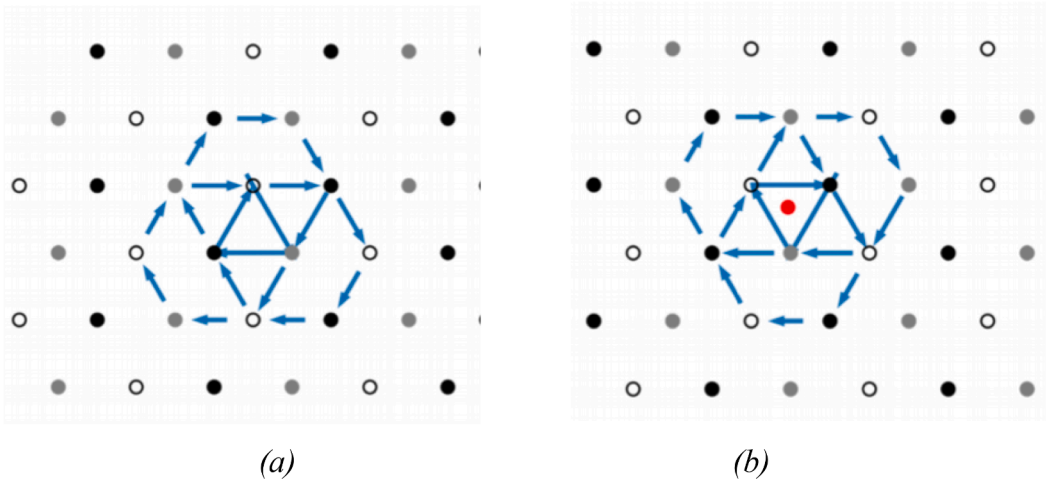

Fig. 19. Easy (a) and hard (b) cores relaxed with DFTB in pure iron and in presence of C atoms respectively. In (b) we recover the reconstructed prismatic core identified by DFT in [154].

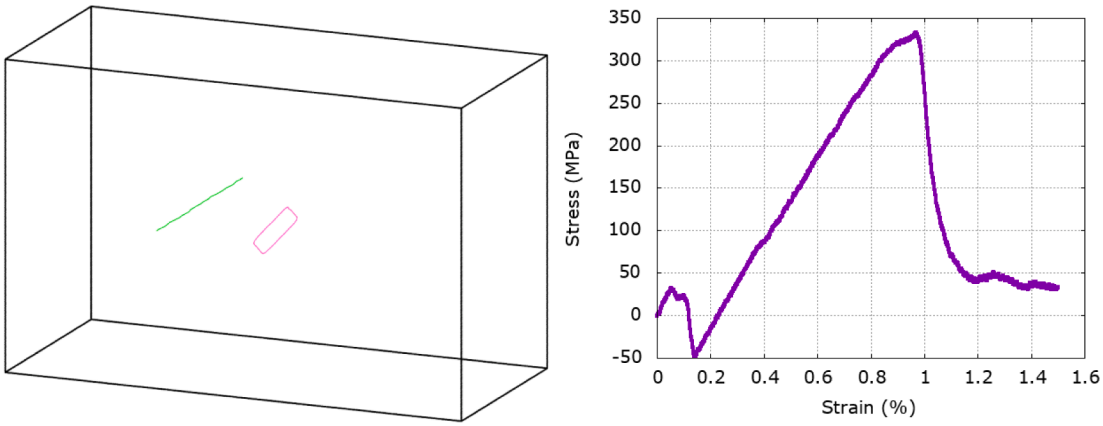

Fig. 20. MD simulation of the interaction of a dislocation with a 5 nm [100] loop in Fe (a) and corresponding stress–strain curve (b) [157].

(3 3 2) grain boundary disconnections pinned by a GBD. The pile-up transforms into the (1 1 2) twin boundaries. The efficiency of this twin in terms of easy shear coupled twin boundary migration is comparable to the most common twin in hcp metals, i.e. the (10–12) twin [161]. These types of studies are expected to provide clues about the conditions that lead dislocation channels to propagate (or not) through grain boundaries. The current main conclusions are that: (1) the crystallography drives the interaction processes between GBs and dislocations; (2) absorption is the predominant reaction observed, while transmission and reflection are possible for both single dislocations and dislocation pileups (transmission only when the stress level is very high and reflection when the second dislocation of the dislocation pileup reaches the GB); (3) the comparison with the results for different materials sharing the same bcc structure of F/M steels (W, Cr) shows that the reactions are the same, with only slight changes in the outcome, thus the results can be partly generalised; (4) the higher the temperature, the lower the stress required for dislocation absorption, therefore the temperature facilitates the absorption process; (5) the GBD, either sessile or glissile (disconnections), are key to understand the mechanisms behind the evolution of the GB under stress conditions. We are however still far from being able to consider all possible cases and thus to translate these results into laws that can be accurately generalized, therefore for the moment the transfer of information through scales is more qualitative than quantitative.

Another problem of transfer of information concerns the dislocation mobility law. As discussed in [162], all atomistic calculations, whether based on interatomic potentials or DFT, overestimate the flow stress at very low temperature, the so-called Peierls stress, by a factor between 2 and 3 [163]. This means that results from MD simulations cannot be directly used to parameterize the dislocation mobility law. It was however possible, based on data from DFT, experiments and high temperature MD simulations, mostly taken from the literature, to propose a mobility law that compares well with the experimental data [162], as shown in Fig. 21.

b) Dislocation dynamics studies

The great majority of defects in irradiated materials have a size below ~ 100 Burgers vectors, hence in the range where the elastic treatment of dislocation lines exhibits instabilities (Fig. 22) [165]. The effect of instability, which is expected to be compensated by non-linear interactions in the dislocation core, is significant in the context of dislocation dynamics, where the treatment of interaction with small defects is believed to be responsible for the radiation hardening and the strain localization effects. The treatment of dislocations interacting with radiation defects requires the force acting on a dislocation segment to be evaluated in the presence of point defects [166], it is therefore necessary to know the stress field generated by these defects. While performing such a calculation appears straightforward, the relevant formulae are not available in literature and need to be derived. Such a derivation has now been performed within the project.

In parallel, the DD simulation code NUMODIS [153,167] was

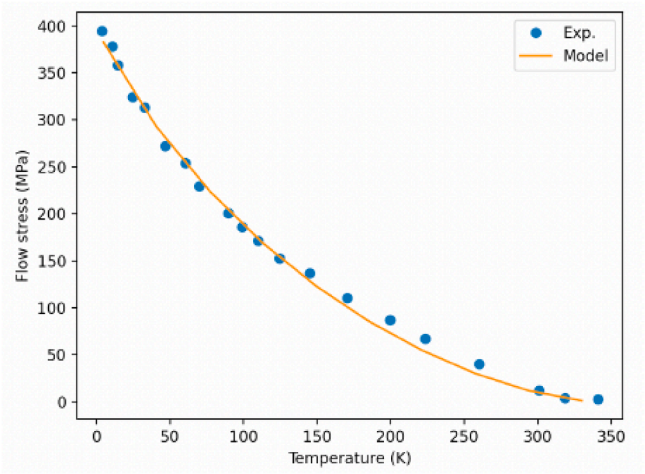

Fig. 21. Comparison between the experimental data of Brunner [164] and the mobility law developed within the M4F project.

coupled to the elastic solver dedicated to boundary value problems resolution AMITEX_FFTP [168], following the example of a similar coupling performed with the code microMegas (Fig. 23). Preliminary benchmarks have been performed to assess the accuracy of this elastic solver against a full DD simulation, but the work is still in course. As an example of benchmark, Fig. 23 shows how the Lomer junction formation is described in classical DD using microMegas and when using the FFT solver.

DD simulations accounting for dislocation/defect interactions and cross-slip [23] have been also used to predict plastic strain spreading in post-irradiated ferritic grain aggregates, using a dedicated micro-model [169]. This model explains how the internal stress landscape evolutions control the dose-dependent development of wavy shear bands, characterized by the *plastic strain spreading ratio* (PSSR), which is defined as the number of shear bands in the irradiated over the non-irradiated case and noted as $PSSR = \frac{N_{irr}}{N_{00dpa}}$ (PSSR < 1 denotes plastic strain localisation). Quantitative PSSRevolutions have been calculated for various grain size, irradiation defect size D and defect number density n conditions. From these calculations (Fig. 24), it has been found that: (1) PSSRsystematically increases with plastic strain level ε_p; (2) PSSRsharply decreases with growing defect size D, for any fixed defect number density n and plastic strain level ε_p; (3) the shear band spacing distribution (i.e. the distribution width and maximum value) depends on the nD product, thus scales with the dispersed barrier hardening effect; (4) the shear band thickness distribution (i.e. the distribution width and maximum value) depends on $1/D$, affecting the local, defect-scale dislocation configuration and corresponding internal stress landscape; (5) homogeneous (PSSR > 1) to localized (PSSR < 1) straining mechanism transition depends on the mutual band-to-band interaction stress intensity and the internal stress level relative to the defect strength σ_{defect}; (6) strain localisation is slightly more pronounced for decreasing grain size, for a fixed n and D.

This approach allows the dose-dependent elongation limit trends to be found and will therefore enable corresponding strain deformation maps [22] to be established. The model applicability to polycrystalline ferritic materials is being evaluated using a specific stochastic calculation procedure, based on observations of ion irradiated/deformed grain aggregates, as discussed in the experimental section.

c) Continuum plasticity studies

Different strain gradient crystal plasticity models have been developed and implemented in the ABAQUS finite element code as user elements for the polycrystalline finite element homogenization process. These models consider displacements and plastic slips as degrees of freedoms. The gradient of plastic slips can be easily calculated through finite element procedures. Initially, non-convex hardening relations were considered for the formation and evolution of slip bands, then the analysis focused more on the evolution of microstructure using simpler linear and nonlinear hardening descriptions. Various studies have been conducted for constant and evolving slip resistance that can be defined per slip system. Due to the computational difficulties, the sign function has been replaced with a smooth sigmoid function, which improves

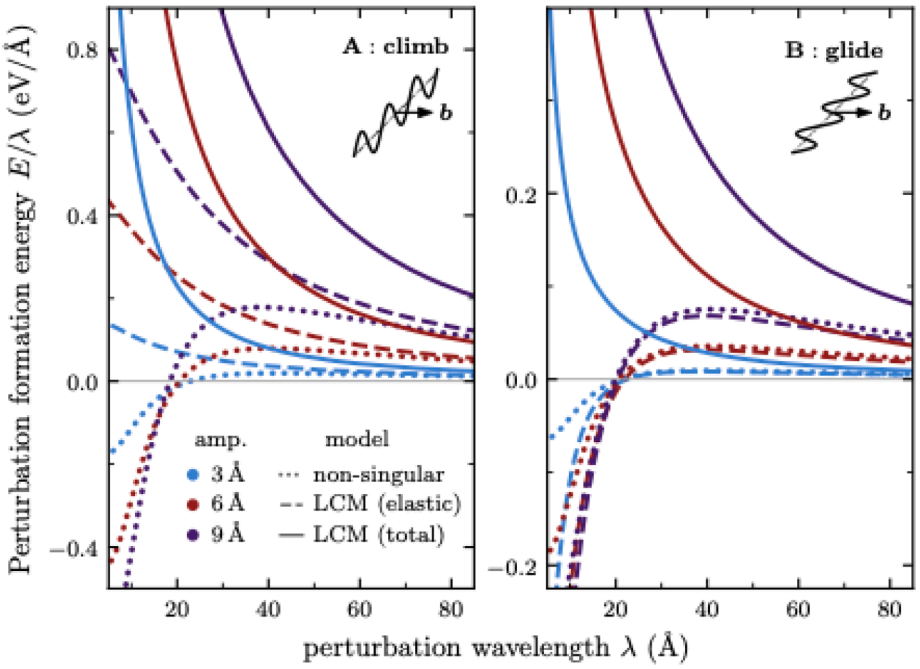

Fig. 22. Formation energy of sinusoidal perturbations in (a) climb and (b) glide directions for a 1/2 [111](1 0 1) edge dislocation. The non-singular elasticity theory is compared with the local core model, with (total) and without (elastic) contribution of the core energy. Note the small-wavelength instabilities inherent to the non-singular theory.

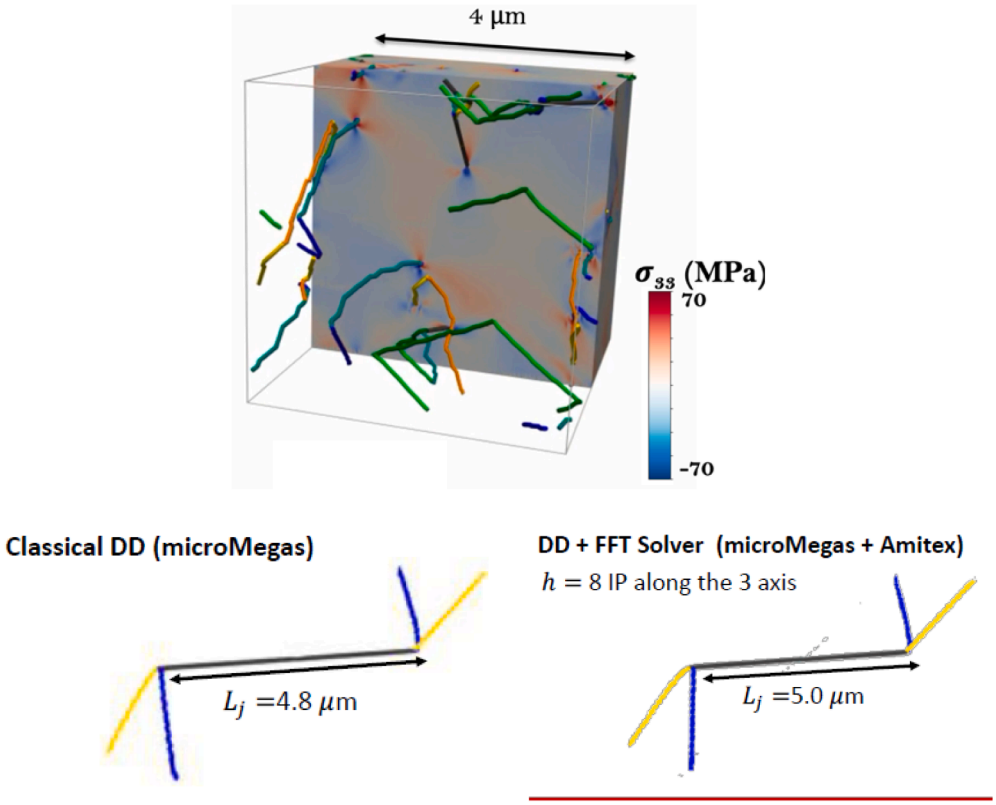

Fig. 23. Above: dislocation microstructure and the associated stress field computed using the coupling between microMegas and AMITEX on a 512x512x512 FFT grid. Below: Lomer junction formation using classical dislocation dynamics with microMegas (left) and the FFT solver (right).

substantially the convergence of the simulations. For example, when modelling a single grain without channels and using three active slip systems, non-linear macroscopic strain-hardening was observed, while linear strain-hardening was observed when using only one active slip system, see Fig. 25**.** The performance of simulations in polycrystals is reported in **section 3.2.3**.

d) Experimental studies

In addition to the ion irradiations described in **Section 3.1.3**, proton irradiations at 7.2 MeV of TEM in-situ straining specimens have been performed employing a degrader to get a flat damage profile up to 50 μm in depth. The materials that have been irradiated are G385-Fe-9Cr and single crystal Fe-16Cr (99.95%), with (1 1 0) oriented surface. In both cases, the proton irradiation conditions were selected to focus on the early stages of dislocation free channel formation: 300 °C as irradiation temperature and 1 dpa as dose. In-situ straining experiments have been performed on the unirradiated Fe-9Cr model alloy, in a wide range of temperatures, i.e. between −170 °C and 500 °C, in order to investigate the plastic deformation mechanisms at the dislocation scale, in the absence of radiation defects, as a pre-requisite to study the irradiated specimens. The observations revealed that dislocations glide in {1 1 0} or {1 1 2} planes with 1/2[111] Burgers vectors at all temperatures, as expected [170]. Dislocation motion always appears to be jerky. At high temperature, this behaviour is exacerbated and culminates with a strong dynamic strain aging at about 400 °C, presumably due to the diffusion of interstitial atoms such as C atoms. Below room temperature, the dislocations exhibit straight screw segments that are pinned by super jogs, which are formed by the combination of cross slip and solute pinning. The dislocation mobility has been estimated based on an assessment of the effective stress. Experiments on irradiated samples were carried out at liquid nitrogen temperature, where dislocation dynamics is steadier. In ion irradiated specimens, several interactions between dislocation loops and mobile screw dislocations were recorded and analyzed. In most cases, irradiation loops are overcome by dislocations after pinning. The importance of dislocation cross-slip in this process has been highlighted. A close inspection of the loop shape tends to indicate that most of them are restored after interactions, although others are pushed along the dislocation line. Further experiments are planned, in order to constitute a statistically representative database of interactions.

Concerning plastic flow localization, the shear band thickness t_B, the spacing d and the surface marking displacement h are closely interrelated quantities, according to the above sketched strain spreading dislocation dynamics model. The theoretical thickness t_B and spacing d distributions results were calculated with the model described above for two different ferritic materials, holding distinct irradiation defect populations, namely: (i) a large number density of small defect clusters; (ii) a smaller number density of larger defect clusters. The model predictions were directly compared to the surface slip marking arrangements and distributions observed in corresponding post-irradiation TEM experiments, after tensile deformation, on the G385-Fe9Cr alloy, which was ion-irradiated with 5 MeV Fe^+ to 0.5 dpa at 300 °C (see Fig. 26). The experimentally-observed shear band distance/thickness d/t_B ratio and PSSR levels are consistent with their theoretical counterparts: d/t_B 4–5 and *PSSR* 0.6–0.7 after 0.5 dpa at 300 °C (mimicked with a number density $n \sim 10^{23}$ m^{-3} of size $D \sim 2$ nm defects) and over 4% plastic strain.

3.2.3. *Deformation mechanisms at the polycrystal scale*

The description of the deformation mechanisms of irradiated F/M steels at the polycrystal scale requires accounting for the deformation localization at the grain scale studied in 3.2.2, with formation of defect-cleared dislocation channels, and consideration of the effects of the interaction of these with microstructural features such as carbides. Furthermore, the consequences of the interaction of the channels with

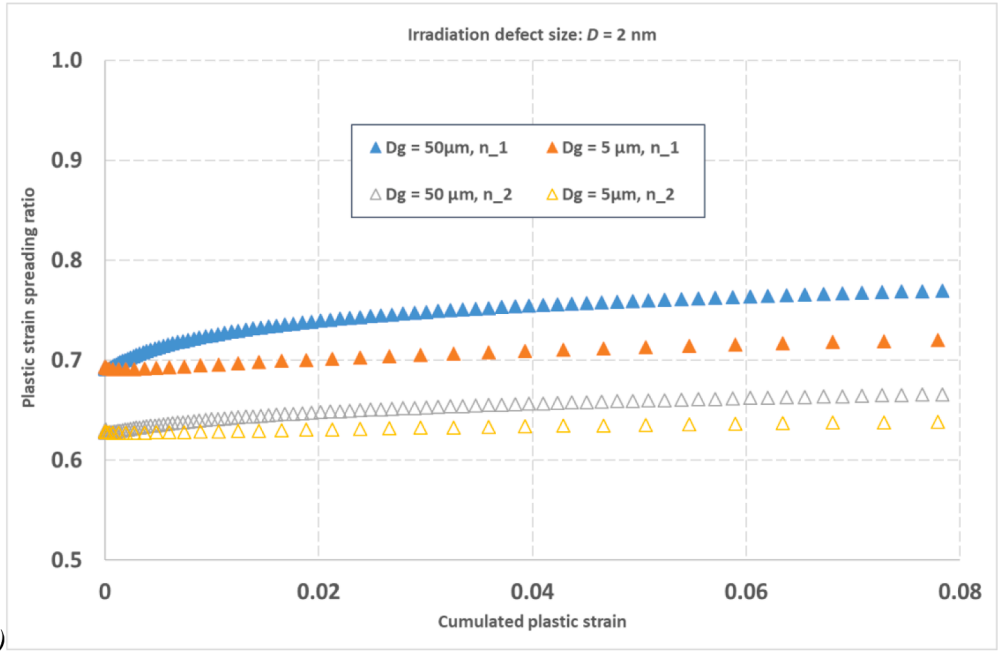

(a)

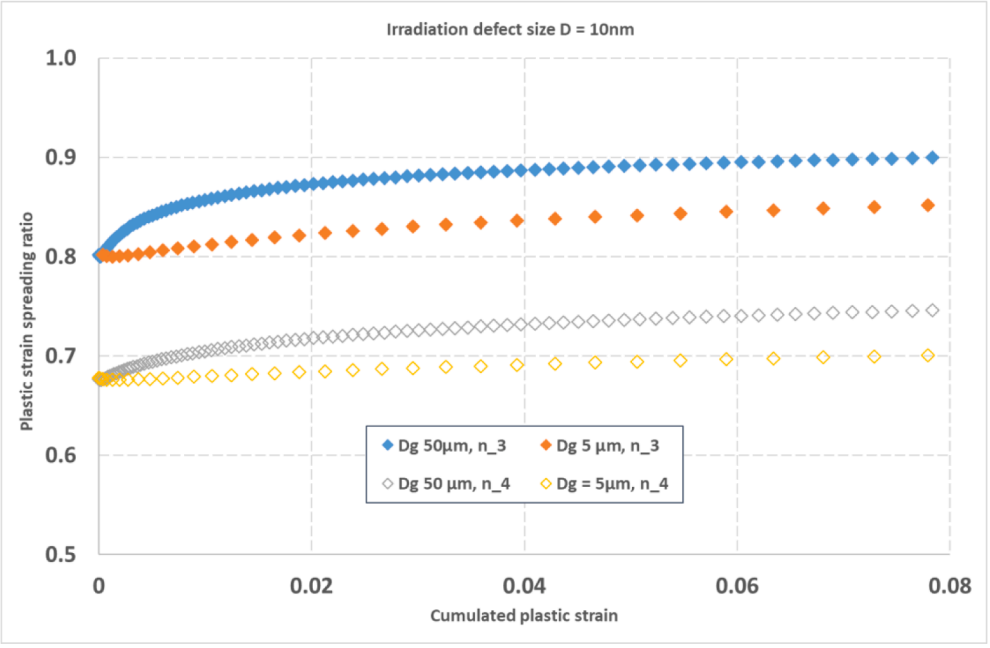

b)

Fig. 24. Plastic strain ratio evolutions with cumulated plastic strain. Influence of the irradiation defect number density and grain size. a) Defect number densities are: $n\_1 = 1 \times 10^{23}$ m^{-3}, $n\_2 = 1 \times 10^{23}$ m^{-3}. b) Defect number densities are: $n\_3 = 3 \times 10^{21}$ m^{-3}, $n\_4 = 3 \times 10^{22}$ m^{-3}. Comparison between (a) and (b) highlights a significant defect size effect. Namely, the plastic strain ratio N_{irr}/N_{00dpa} is significantly lower in presence of larger defects, regardless of the tested defect number densities.

grain boundaries, atomistically studied in 3.2.2a, as well as channel-channel interactions, need to be accounted for, as the resulting stress concentrations may accelerate the cavity nucleation and growth process, thus modifying damage evolution in comparison with the unirradiated state. The lack of extensive data regarding the evolution of radiation defects and void volume fraction as well as quantitative features of channeling in the course of plastic deformation is a major challenge for the modelling of the mechanical response of irradiated materials. It should also be noted that, in this as in many other applications, no lower scale tools currently exist that are suitable to study the effect of carbides as crack initiators or in interaction with dislocations pileups, thus in this case no hint can be obtained from more fundamental tools and the experimental input is essential.

Three aspects of polycrystal deformation modelling in irradiated F/M steels were therefore addressed in the project: (a) damage initiation processes during tensile loading as a consequence of channeling (cavitation/nano-cavitation mechanisms under deformation); (b) homogenization schemes to be applied for the determination of the macroscopic tensile behaviour; (c) description of the coupled deformation and damage behaviour. In addition, experimental examinations of irradiated materials subjected to deformation are conducted in support of the models.

a) Damage initiation

Two cavitation scenarios are studied. The first one considers the decohesion of the carbide-matrix when approaching necking and implies an extrapolation of cavity nucleation in the un-irradiated case [171] towards the irradiated state. A model is proposed where the number of voids per unit volume is a function of the thickness of the clear channel, the inter-channel spacing and the average deformation carried by one such channel. The key constant in the model is taken from the

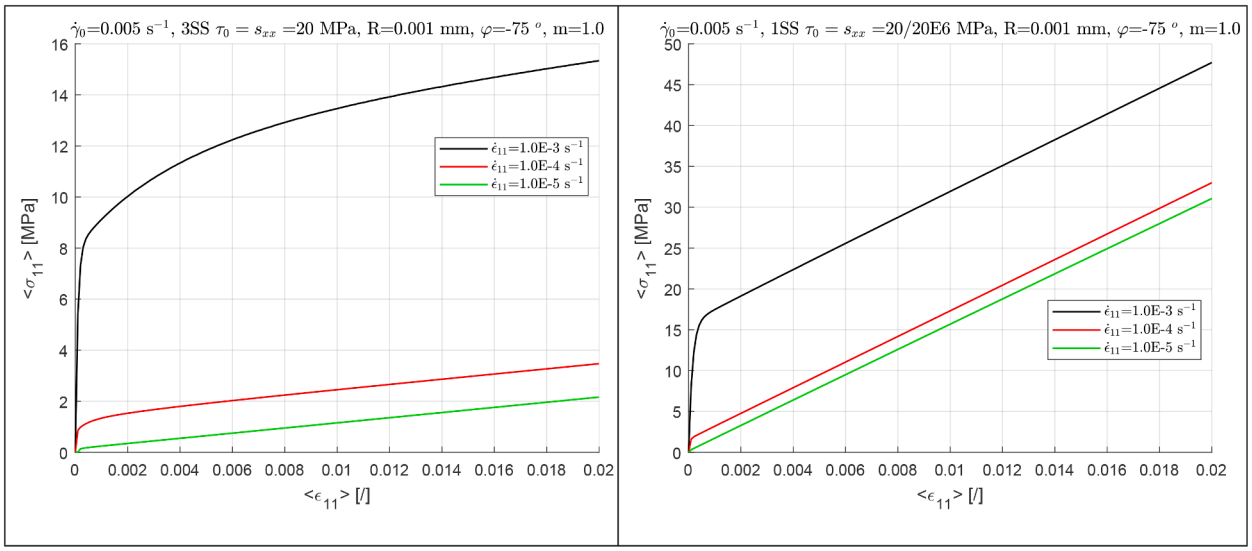

Fig. 25. Macroscopic response of a single grain case without channels. Left: three acive slip systems. Right: one active slip system.

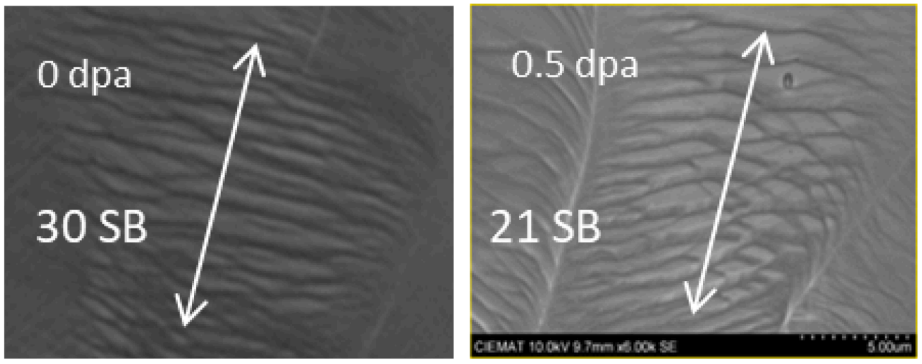

Fig. 26. Example of local, post-irradiation strain localisation assessment in G385-Fe9Cr alloy. The comparison is made for grains of similar size, after the same amount of plastic deformation. "SB" denotes the surface markings associated with shear bands cutting through the grains.

measurement of the number of carbides that are broken with the average plastic deformation in TEM by Senior *et al.* [171], while new studies are being performed in the framework of the project. The second scenario is based on the process of vacancy clustering under the effect of stress concentration, due to the impingement of clear channels on the grain boundaries, given that, in the absence of carbides, crack initiation is intergranular at necking [172]. This process is studied by atomic scale simulations using the EAM potential for bcc Fe proposed in [173]. Four symmetrical tilt grain boundaries were selected, two with an axis along [110] and two along [100]. Segregation energy maps for single vacancies and activation energies for single and di-vacancies, as a function of the strain perpendicular to the interface, were calculated. Segregation is strong, but tends to decrease with increasing strain. Vacancies and di-vacancies are mobile down to room temperature, with a tendency for one dimensional diffusion along the tilt axis. In order to go beyond di-vacancies and study clusters of larger sizes, the method call "Smart Darting" was adapted to an available Metropolis Monte Carlo (MMC) code for vacancies at grain boundaries [174]. The code simulates the (N, V,T) ensemble using the same interatomic potential as in the above mapping calculations. The strain is initially applied to the system by elongating the box length in the direction perpendicular to the interface (one dimensional tension). The volume is decomposed into Voronoi cells, based on the elongated body centered lattice of Fe and the grain boundary structure of minimal energy. A microscopic configuration is defined by a vector containing the cell occupancies which are set to 0 when the cell is empty (vacancy) and to one when it contains a particle. In addition, a displacement vector is associared with every particle to define its position with respect to the lattice node inside its cell. Therefore, the configuration space, which is sampled by MMC, is a vector of length M (M3N) of occupancies, coupled to vectors of three dimensional displacements confined to the Voronoi cells. The MMC moves are: (i) displacements of randomly chosen particles by a random amount of fixed maximum amplitude, within the Voronoi cells and (ii) exchanges of occupancies between empty and occupied cells coupled to a random insertion of the particle within the vacancy, in general in first neighbour position. When the presence of a vacancy creates large relaxations of its neighbours, the exchange move is never accepted. In this case the "Smart Darting" method enables transitions from one relaxed state to another, which resolves the problem of trapping of standard MMC, although at the expense of higher computational cost. With this new method, clusters of vacancies of size 5 either along the tilt axis or in the form of 2D platelets were found for the Σ29(730)[001] grain boundary (Fig. 27). Future work will be devoted to the study of bubbles and the comparison of their energy with respect to the platelets, in order to determine if the bubbles are thermodynamically stable and if so at which strain. These conditions will be compared to those expected at the tip of a clear channel impinging on a grain boundary.

b) Polycrystal homogenization

Two homogenization schemes are being studied, which are based, respectively, on mean-field and full-field approaches. In the mean-field

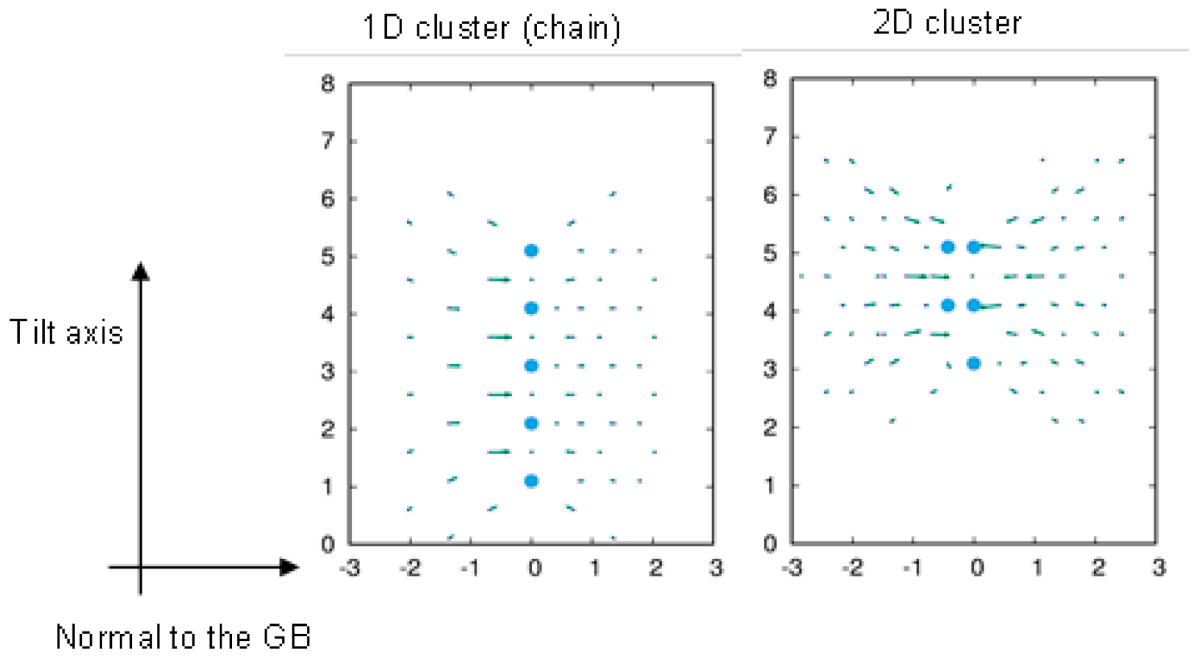

Fig. 27. 1D and 2D clusters, containing 5 vacancies, obtained by atomistic Metropolis Monte Carlo simulations in the $\sum 29(730)[001]$ symmetrical tilt grain boundary in bcc Fe (EAM potential M07 from [177]). The circles represent the vacancies and the arrows the displacement field (the relaxation of the neighbours). The axis × and y are distances in a_0.

homogenization scheme, the advanced Eshelby solution [175] is developed by properly accounting for channel scale, F/M block scale and matrix scale. The full-field homogenization is conducted through a strain gradient crystal plasticity (SGCP) model [176,177], which is employed to the polycrystalline aggregates with and without channels. The comparison of the macroscopic tensile curves predicted by the two parallel approaches and their validation by means of experimentally determined tensile curves will allow the influence of channeling on the tensile behavior to be more deeply understood. The calculations with the two methods are performed with similar sets of parameters (mean grain size, inter-channel distance, channel thickness, initial resolved shear stress, etc), compatibly with the inherent differences between methods. For example in the mean field approximation all channels have similar length, not so in the full field method; but the mean grain size value can be exactly the same in both.

Mean field approach. The formation of channel structures in single crystals and grains has been observed experimentally in irradiated F/M alloys [17,19,178]. In the proposed polycrystalline homogenization model [175], a very small ratio between the channel thickness (about 100 nm) and the channel length (close to the grain size) leads to much lower internal stresses in the polycrystal, yielding lower strain hardening. This model uses three parameters that can be measured by experimental observations (in addition to TEM, also scanning electron microscopy, SEM, and atom force microscopy, AFM): the channel thickness, the grain size and the maximum plastic slip that can be accommodated by each channel. As a first approach, intragranular hardening laws are not accounted for; instead, an initial critical shear stress, $\tau_{c,0}$, is considered. This material parameter is strongly dependent on the irradiation dose received by the material and its grain size. This parameter is the only one that is adjusted using the polycrystalline tensile curves. In the elastic–plastic framework, by accounting for the increase of the number of channels with remote plastic deformation, only negligible hardening is observed. This behaviour results directly from the small ratio between the channel thickness and the channel length. Moreover, the simulations predict polycrystalline tensile curves that show similar behavior to those observed in irradiated bcc iron and F/M steels. Finally, a low number of activated slip systems is predicted, even for remote plastic strains of 10%, in agreement with microscopic observations. In order to avoid the use of $\tau_{c,0}$ as fitting parameter, an analytical method is proposed. The critical stress can be then defined as the sum of the Peierls stress, $\tau_{c,Peierls}$, the stress induced by interactions between dislocation lines, $\tau_{c,\rho}$, and the stress resulting from interactions between mobile dislocations and irradiation loops, $\tau_{c,loop}$. The first stress can be easily defined using tensile curves of non-irradiated single crystals. $\tau_{c,\rho}$ can be expressed through evolution laws of edge and screw dislocation densities, accounting also for the grain size (Hall Petch) effect [179]. Experimentally, it has been shown that the Hall-Petch coefficients that are measured in non-irradiated and irradiated materials are very similar [180]. Finally, the stress resulting from the interaction between mobile dislocations and irradiation loops can be expressed using a Taylor-kind law [181] and depends on the diameter and concentration of the irradiation loops [182]. The analytical values of $\tau_{c,0}$ determined using this method are in agreement with those fitted to polycrystalline curves. The next step in order to better describe the material hardening behavior under tensile tests, without using any adjusted parameter, will be the implementation of intragranular hardening laws. The final goal is the prediction of the tensile behavior of irradiated materials, applying experimental measurements of thickness and length of channels, on irradiated Fe-9Cr (d). The calculated curves will be eventually compared to the experimental ones.

Full field approach. Finite elements descriptions of polycrystalline aggregates, containing 1 (see **3.2.2c**), 2, 14, 50, 110 and 212 grains, have been setup for comparison with the mean field approach. The grains themselves are randomly sized and shaped by using a Voronoi tessellation. The crystallographic orientation of each grain is a random variable. These polycrystalline aggregates are then coupled with a strain gradient crystal plasticity (SGCP) model (see e.g. [176,177]). However, instead of using non-convex potentials (see e.g. [183,184]), which would lead to uncontrolled formation and evolution of channels, the standard version of the strain gradient crystal plasticity framework is employed and channels are explicitly built into the geometry of each of the grain. The channel orientation is aligned with the crystallographic orientation of the grain. The number of channels per grain, channel thickness and spacing (distance between the channels) are all parametrically defined and can be adjusted. A channel thickness of $t = 100$ nm is used as this is a typical channel thickness for pure iron,

ferritic Fe + Cr polycrystals and ferritic-martensitic steels. An average grain size of 23 μm is used. Such a small channel thickness imposes severe constraints on the meshing procedure, the larger the number of grains and the number of channels per grain, the more difficult it becomes to obtain the mesh. Although a mesh could be obtained for aggregates having grains filled with channels (channel spacing $d = 1.2$ μm) containing up to 14 grains, the number of channels had to be reduced to four per grain for the aggregates containing 50 (Fig. 28), 110, and 212 grains. Macroscopic responses for aggregates containing channels up to 212 grains have been computed. The effect of the length scale parameter R (radius of dislocation domain contributing to the internal stress field) on the stress and macroscopic response has been investigated: for R = 0.1 μm the stress between channels is averaged out and channels are almost invisible; for R = 0.05 μm channels become visible in the stress field; finally, for R = 0.025 μm channels are well visible in the stress field. To obtain Figs. 29 and 30, four 0.1 μm thick channels per grain were explicitly built. Only the slip system aligned with the channel direction was activated within a channel, while the slip resistance (critical resolved shear stress) of the other two slip systems were set very high (20^6 MPa), so as not to trigger their activation. This roughly mimics the number of experimentally observed active slip systems. The same high slip resistance for the other two slip systems was also used in the areas in between the channels. Calculated macroscopic stress–strain curves of polycrystalline models with channels resulted in somewhat lower stresses at given strain, compared to the models where channels were not included. At macroscopic strain of 1 %, a thick, highly deformed, global band developed in the polycrystalline aggregate. On the other hand, when three slip systems were activated in between the channels, the stresses reduced significantly, stress increases in channels were easily observable and no highly deformed global band was observed. Fig. 29 shows the Mises stress field of an aggregate containing 110 grains: R = 0.0 is used, three slip systems are activated outside of the channels, while only one slip system is activated within channels. Slip resistance in the channels is 10 times lower than outside of channels. Channels are clearly visible. Activating only one slip system outside of channels results in macroscopic deformation channels, spreading across the aggregate, as in Fig. 30.

c) Coupled deformation and damage behaviour

A thermodynamic framework for irradiated materials is built up by accounting for the amount of energy that is spent for the creation of irradiation defects in the material's free energy. This framework provides a platform for identifying thermodynamic consistency conditions and for modeling the post-yield and post-necking behavior of irradiated F/M steels [185]. The deformation mechanism is described with the viscoplastic model by Aktaa and Petersen [186], which uses the defect density evolution as a metric to determine the amount of instantaneous irradiation hardening present in the material. The viscoplasticity framework reduces the mesh sensitivity of the model and ensures a well-posed initial value problem, which drastically improves the performance of the simulation. A finite strain formulation of this model is developed using the dual variables approach [187] resulting in a set of co-rotational constitutive equations. Finally, the Hughes-Winget algorithm [188] and the Weber transformation method [189] have been chosen to integrate the co-rotational form of the evolution equations. The resulting model needs calibration based on the experimental data from the experimental studies.

Fig. 28. Finite element mesh of an aggregate containing 50 grains with four channels per grain. Each grain is colored differently with channels seen as narrow, parallel bands within each of the grain.

Focus was put on the identification of a suitable ductile damage model to account for void nucleation and coalescence. Among the available pressure-dependent damage models, the Gurson-Trevgaard-Needleman (GTN) one [190] is the most popular, as it establishes an ellipsoid type yield surface that shrinks with the growth of the damage variable - void volume fraction (VVF) - and provides easy-to-implement evolution equations for determining VVF. As a matter of fact, the damage initiation model developed in the project is still at too an early stage of development to be used. The application of the GTN model requires the determination of the critical void volume fraction from experiments, while the other parameters are fitted. These parameters were taken from the literature [191]. Alternative evolution equations to determine VVF are those used in (a), based on the work of Senior [171], which provides a void nucleation criterion that may be modified for application to irradiated materials. The major challenge was to extend the rate-independent plasticity-based GTN model to the rate-dependent plasticity framework, which would reduce the mesh sensitivity of the damage model. A viscoplastic potential was formulated by combining the GTN yield criteria and the viscoplastic flow rule, which was used when deriving the new flow rule and inelastic strain rate for the viscoplastic-GTN model. The model was implemented in ABAQUS using a user-defined subroutine, UMAT, based on the finite strain framework, and the NLGEOM option was used to simulate the yielding and flow softening of irradiated Eurofer97. However, the model parameters at hand (which were used for small deformations) have to be recalibrated for a finite strain application. The finite strain model described above is under implementation in ABAQUS, with the help of a complex integration algorithm, which is capable of handling finite rotations. The model parameters are being recalibrated by using the Bridgemann true-stress and true-strain correction procedure [192], applied to the data from the experimental studies of the project (see next), to replicate experimentally measured post-yielding and post-necking behavior. To ensure that the material instabilities, as well as the diffused and the localized necking, are correctly described, several parameters need still to be optimized and accurately determined. Results of tensile test simulation performed on the unirradiated sample are shown in Fig. 31, along with the experimentally obtained true stress vs true strain curve (see below). The results are encouraging as the desired behavior is captured.

d) Experimental studies

In-situ high-resolution (100 nm) SEM tensile tests, with surface field measurements, in pristine Fe, are underway to try to observe the mechanisms studied in (a) and measure the parameters that appear in the model. In addition, TEM examination of in-situ strained ion and proton irradiated specimens of the fully ferritic Fe-9%Cr is being carried out, in order to provide quantitative information of the pre-irradiated and deformed microstructure, for example clear band thickness, inter-band distance, grain size, maximum accommodated strain, etc., provided that the irradiation dose is high enough to actually observe channels. Next, the deformed samples will be characterized by Electron Backscatter Diffraction (EBSD), in order to provide information about

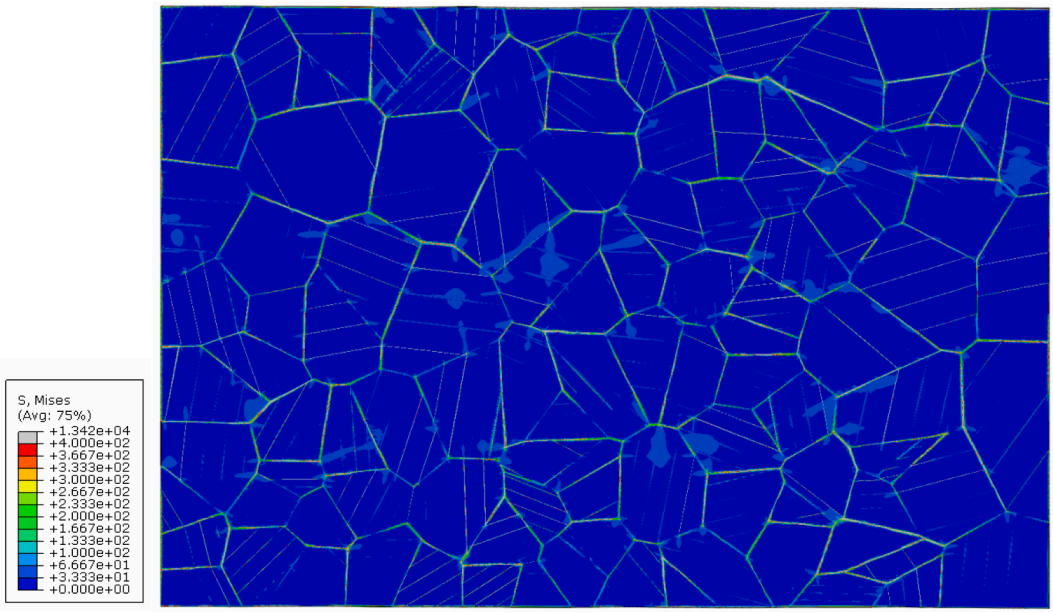

Fig. 29. Mises stress [MPa] field of an aggregate containing 110 grains, with four channels per grain, stretched in the horizontal direction to $<\varepsilon_{11}>=0.01$ [/]. Three slip systems activated in between the channels, one slip system activated in the slip channels. Channels are clearly visible.

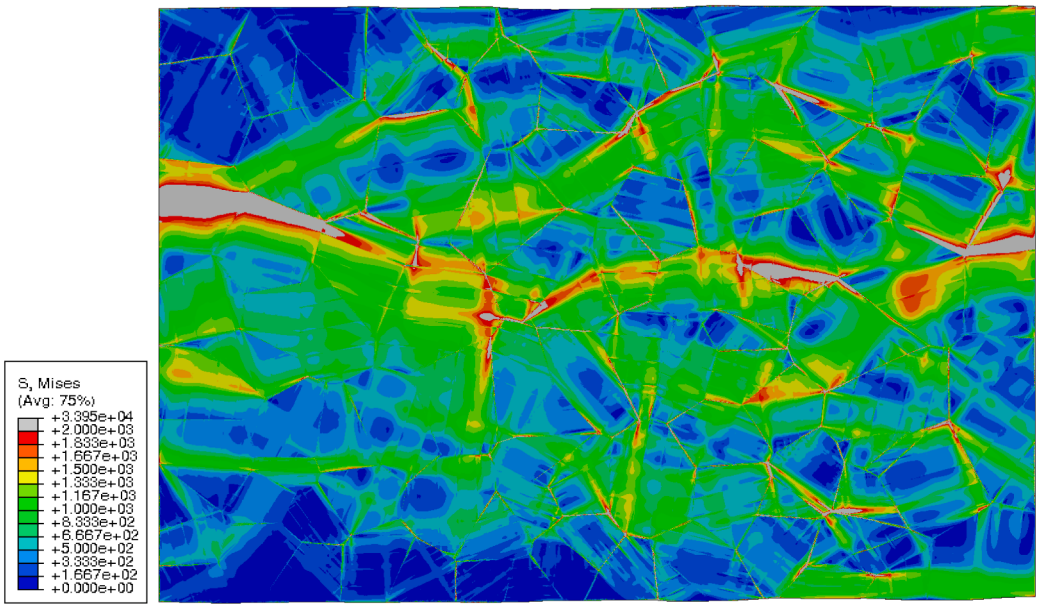

Fig. 30. Mises stress [MPa] field of an aggregate containing 110 grains, with four channels per grain, stretched in the horizontal direction to $<\varepsilon_{11}>=0.01$ [/]. One slip system activated in between the channels, one slip system activated in the slip channels.

deformation modes. Some samples have been already strained and examined in in-situ experiments. The results will be of direct use for the models developed in (b). Additionally, selected samples are being examined by AFM for the evaluation of surface steps and then plastic slips carried out by the shear bands. Strained specimens have already been examined using this technique, yielding reference surface marking displacements in several selected grains. For instance, a quantitative evaluation (serving as a benchmark test) has been carried out and the observed markings compared well with its theoretical counterpart in a reference ferritic steel, in un-irradiated or as-received material conditions. After 7–10% cumulated plastic strain, the theoretical inter-band spacing is $d = 0.4$–$0.7\,\mu m$ and the surface marking displacement $h = 40$–60 nm. Corresponding AFM measurements yield $h = 10$–70 nm, depending on the deformed grain considered. Further surface step height evaluations will be carried out on ion-irradiated materials, depending on available results/specimens. Finally, localized deformation in neutron irradiated Eurofer97 is being investigated by TEM after tensile testing. All mechanical tests have been performed and the fracture surface has been analyzed. TEM examinations of FIB-cut lamellas have been carried out and their analysis is underway.

True stress/true strain curves have been obtained by developing a digital image correlation procedure, first in cold lab and then applied in hot cells to test neutron irradiated samples. The quality of the applied video registration (with fixed focus point) is sufficient to perform video recording with the furnace door closed and with the standard furnace light, which enables video-recording neutron irradiated samples during the test at elevated temperature. The video-recording can be effectively performed at the loading rate of 2 mm/min or lower. The calibration

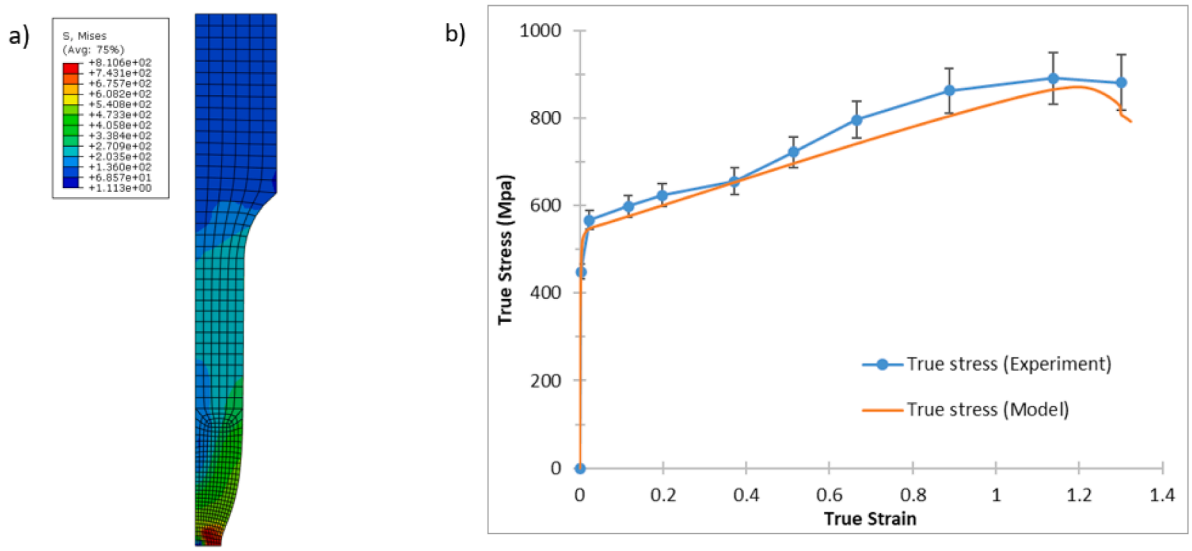

Fig. 31. Simulation results of tensile test on an unirradiated sample at 300 °C with a) contour plot of von Mises stress distribution after damage, b) Simulated mean true stress vs. true strain plotted against true stress vs true strain obtained from experimental load–displacement data and minimum diameter extracted from the recorded video sequence of the experiment. Error bars indicate uncertainties due to limited video record resolution.

measurements were performed using non-irradiated Eurofer97 samples (from the same batch as neutron irradiation samples) in the temperature interval between RT and 300 °C. Additional tests were performed by interrupting the deformation at several points across the loading curve and high resolution photo images were taken to validate the measurements of the neck width, otherwise measured in video stream. The gauge diameter of the sample was 2.4 mm and length 12 mm. Tensile tests on neutron irradiated samples were recorded while being performed in the temperature range of 22–300 C. Four samples were studied, which had been irradiated to 0.22 dpa (E97-204, T_{test} = RT), 0.65 dpa (E97-205, T_{test} = 300 °C), 1.05 dpa (E97-206, T_{test} = RT), 1.18 dpa (E97-208, T_{test} = 300 °C). The samples were cut from the Eurofer97 cylindrical bars in such a way that the sample axis and the bar axis coincide. The samples were cut close to the edge of the bar as is shown in Fig. 32(a). The standard miniaturized geometry of the cylindrical sample was used, as shown in Fig. 32(b).

The resulting engineering and true stress – engineering strain curves are deduced from the experimentally measured load–displacement. The experimental curve in Fig. 31 was obtained with this method. The samples irradiated to a dose higher than 0.65 dpa show very low uniform elongation and deform by early necking. Based on the derivation of the neck cross-section by video recording (with automatic cross-section calculation), the true stress was recalculated. The Bridgeman correction [192] was then applied by extracting snapshots from the video streams, and the comparison of the corrected stress with engineering as well as true stress (from video). The results reveal that only the 1.18 dpa irradiated sample shows the decrease of the true stress after the yield (i.e. strain softening phenomena), which is also seen on the engineering stress–strain curve (as an inflection point). In samples tested at 300 °C, fracture occurs when the true stress reaches ~ 0.8–0.85 GPa, while for those tested at RT, the fracture occurs at ~ 1 GPa.

4. Concluding remarks: Summary of achievements and result exploitation

Here we summarise the main (expected) achievements of the project, knowing that at the time of writing several activities were still underway: not all results had been obtained, analysed and reported. In addition, past experience from projects of similar kind and scope indicates that the post-project exploitation of the corresponding results and their impact, while expected to be significant, takes several years after the official end of the project before emerging [193]. It is especially important to write a note concerning the multiscale modelling approach pursued in the project. Ideally, in this framework the output of lower scale, more fundamental and detailed models, should be the input to higher scale, coarser grained models. In practice, bridging the scales is

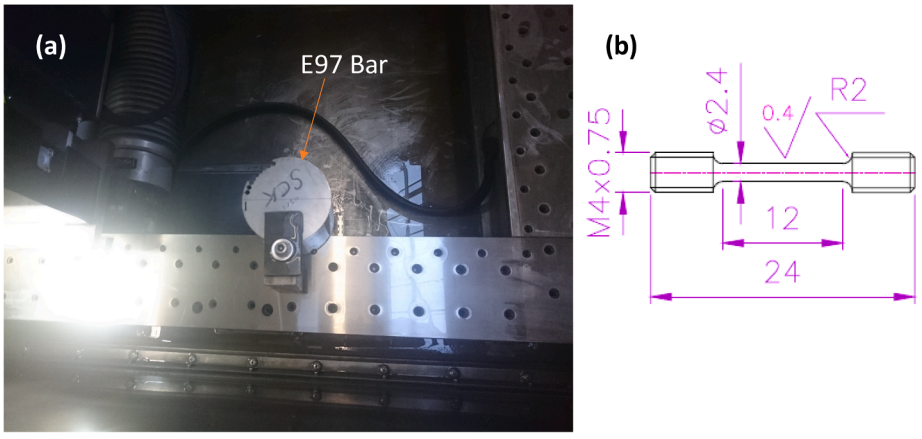

Fig. 32. (a) The E97 bar fixed inside the electroic discharge machine from which the tensile samples are cut. (b) Technical drawing of the tensile sample, gauge section diameter is 2.4 mm, gauge section length is 12 mm.

well-known to be difficult, especially when the materials addressed are real ones such as steels, rather than simpler model alloys. In particular, the effects of complex chemical compositions start to be accessible now to atomic- level and microstructure evolution simulation techniques, but are often ignored, and can only be introduced in an effective way via calibration, in mechanical property models. To realize this, it is sufficient to take the example of the embrittlement of reactor pressure vessel steels used in current nuclear power plants, which started to be addressed using a multiscale modelling approach at the beginning of the 2000s and required several chained European projects to come close to a potential industrial application, with explicit accountance for the detailed chemical composition [117]. This is amply discussed in [193] and is in line with the statement of [194] that, to date, multi scale modelling corresponds mainly to using several "single-scale" approaches, in which one uses one specific method at each relevant scale. Quoting again [194]: "[…] the single-scale approach results in a loss of information across different scales and is an important limiting factor in the science of complex materials. A comprehensive vision would allow the exploration of full ranges of materials solutions and hierarchical architectures at all relevant size scales, with the idea that the resulting product is not simply the sum of all the parts. This requires, [however], the development of new science as well as novel computational methods, since multiscale tools are still in their infancy". In this project the situation is in line with these statements.

Two problems have been addressed using multiscale modelling tools, namely: (1) the differences and similarities between the microstructure evolution under ion and neutron irradiation, together with the exploration of ways of determining its effect on the mechanical properties also from ion irradiated specimens, and (2) the origin of plastic flow localisation and its consequences on the mechanical response of irradiated materials. The development and application of cutting-edge modelling approaches has been attempted, in some cases with very valuable results, but in most cases the time was not sufficient to employ their output as input to higher scale models that were being developed in parallel. These, therefore, had to be based for their development on pre-existing results, measurements and data in general, or else on preliminary qualitative conclusions from other activities within the project. This is why it is expected that the impact of the project will be visible only after several years from its end, as almost invariably happens, when the tools developed in the project have been used on a sufficiently wide and representative set of cases.

4.1. Contribution towards design codes for the use of F/M steels in nuclear systems

It is important to emphasise that the loss of uniform elongation as a consequence of low temperature neutron irradiation currently disqualifies F/M steels for application in structural components, if the existing design rules are used [195]. This is the main motivation for addressing this topic in the M4F project. It is equally important to emphasise that new design rules require deeper understanding of the mechanisms involved in plastic flow localisation to be devised, therefore it is mandatory to study the microstructure evolution under irradiation and its interaction with dislocations, possibly including the effects of the chemical complexity of the target materials, i.e. steels with ferritic/martensitic structure.

In this framework, all the work dedicated to developing faster, but highly detailed, dislocation dynamics models, such as the NUMODIS code, while producing examples of loop-dislocation interaction from MD in somewhat more complex materials than just Fe, which can be used to calibrate the DDD code, clearly moves in the direction that has to be followed to have tools that can eventually quantitatively predict the formation of dislocation channels with their correct features (thickness, mutual distance, length, … as well as local strain). These numbers enter continuum models and can currently only be obtained from long, dedicated and costly experimental examinations. While several useful experimental data exist and more will have been collected on both pristine and irradiated materials by the end of the project, the importance of having a tool that can eventually reliably enrich the limited number of data that can be obtained experimentally is clear and the project did contribute a further step along this path, even if no final tool is yet available. Equally important is the study, also pursued in the project, of the interaction between dislocation pileups and grain boundaries: eventually these, if extended to a sufficient number of representative cases, should provide criteria for improved continuum models concerning channel evolution in aggregates, by providing conditions and criteria for channel interruption or transmission. What remains open, as mentioned already, is the atomic-level and dislocation dynamics study of other phenomenologically important processes, such as channel-channel and channel-carbide interactions. Because of the scales and details involved, these are hardly at the reach of current modelling tools. However, an important result obtained in the project in this respect is the prediction by dislocation dynamics of the dose dependent formation of shear bands, with reasonable degree of success when compared to experimental observations.

The problem of accounting for the effect of dislocation channel formation on the mechanical behaviour of, specifically, 9%Cr iron alloys has been approached in three ways: with a (1) mean field and a (2) full field continuum model at aggregate level, as well as with (3) constitutive equations. The mean field model offers a less detailed, but more efficient, way to study the effect of channel formation on the mechanical behaviour of aggregates; the full field approach, while trying the implementation of advanced strain gradient crystal plasticity, offers the possibility of being more detailed in terms of grain distribution, at the price of a higher computational cost. Both should eventually provide the building blocks for a fully physical description of the mechanical behaviour of components, including the effect of heterogeneities. Meanwhile, the constitutive equation approach, while still requiring extensive calibration, already enables finite element modelling to be extended to components. Tools that are usable to assess the effect of plastic flow localisation at the component level will therefore be available at the end of the project, although further calibration of the damage model will be needed, based on improved understanding of void growth and by means of dedicated experimental and theoretical studies in irradiated materials. This is a crucial step towards improved design rules, because such type of tool did not exist before the project.

4.2. Contribution to good practices for the use of ion irradiation as screening tool for nuclear materials

The final tool, able to fully address the problem of transferability of ion irradiation results for the assessment of the effects of neutron irradiation, should be a sufficiently detailed microstructure evolution model that provides a sort of "transfer function', to be used to move from one to the other type of irradiation. Such tool should be calibrated for both types of impinging particles and include all the relevant chemical effects on radiation damage evolution.

Such a tool is still far away in the future. However, important progresses have been achieved by developing three new and complementary microstructure evolution models, each offering new modelling opportunities that were not available before the project, namely: (1) simulation of the whole ion penetration thickness; (2) simulation of Cr concentrated alloys including precipitation and segregation in representative volumes; and (3) simulation of the effect of minor solutes on microstructure evolution, with correct description of the formation of solute clusters. Obviously, the final tool should include all these currently separated capabilities, but the complexity of addressing each item and the large number of parameters that need to be identified would have made their early merge unmanageable. A way to improve the parameters for these models involves the availability of suitable advanced hamiltonians for systems of atoms, which should allow the effect of composition, temperature and magnetism to be correctly

included in the assessment of typical quantities that drive the microstructure evolution in irradiated materials, such as diffusivity and stability of defects. Several attempts of this type have been made in the project, with different degrees of success. Once again, their impact and actual contribution to the reliability of microstructure evolution models under irradiation will be seen in the coming years, when these tools are used for the computation of the quantities required by the microstructure evolution models. Meanwhile, the large number of DFT data obtained for Fe-Cr can already be used to better parameterise the cell-OKMC model in terms of dependence of characteristic energy values as functions of Cr content.

On the experimental side, ion irradiations have been performed applying different parameters: different ion energy, focused beam versus rastering, different doses and temperatures, on the same materials and under the same conditions. This will provide useful indications for good practices, after the post-irradiation examination is completed, as well as a rich set of data for model calibration and validation. Clearly one difficult variable to control when performing ion irradiation is C contamination and likely special attention will have to be given to this topic in the future, with the help of suitable models to fully understand mechanisms and thus improve the mitigation strategies. It has to be considered that the involved scientific community has full conscience of this problem only from a few years.

Even in the absence of fully developed ion-to-neutron transferability tools, ion irradiation is useful as a screening tool for the down-selection of improved materials for nuclear reactors. This use is especially promising if combined with the progressive incorporation of artificial intelligence and high throughput approaches for fabrication and characterisation, in addition to modelling, towards the creation of platforms for accelerated optimization of materials and even autonomous discovery, as envisaged for a wide spectrum of energy applications in, for example, Ref. [196].

However, in this framework it is mandatory to have the possibility of assessing also the mechanical property changes induced by (ion) irradiation. Nanoindentation is one of the few techniques that allow the mechanical properties of ion irradiated materials to be probed in the thin layers affected by these particles, with the advantage that it does not require the long preparation process that is typical of other mechanical tests applied to miniaturised specimens. However, as well as ion irradiation experiments, its use for these purposes needs to be guided by good practices. These have been drafted in the framework of the M4F project and will be released at the end of it in the case of ion irradiation, while standards for testing have reached the level of a CEN workshop and relevant publication, as is shortly described in the Appendix.

4.3. Conclusion

In conclusion, several important results have been obtained so far in the framework of the M4F project, and more will be obtained by its end, in the field of multiscale modelling applied to radiation effects in F/M alloys. Here the multiscale modelling approach should not be read as synonymous of chaining simulation codes through scales, but rather of using the correct tool to address each problem at the correct scale. The actual contribution to a multiscale model integration will become clearer in the future and will be the main impact of the project. This paper provides an integrated view over its objectives, tasks and preliminary achievements, that is deemed useful in view of understanding the connection between otherwise scattered work that has been published and will still be published over the next few years.

Declaration of Competing Interest

The authors declare that they have no known competing financial interests or personal relationships that could have appeared to influence the work reported in this paper.

Acknowledgments

This work has received funding from the Euratom research and training programme 2014-2018 under grant agreement No. 755039 (M4F project).

Appendix

Nanoindentation data collection and CEN workshop on standard-compliant data formats A total of 687 individual nanoindentation data sets have been uploaded onto the MatDB engineering materials database hosted at https://odin.jrc.ec.europa.eu. Taking advantage of the MatDB data citation feature, all data sets are enabled for citation and hence can be referenced as any publication. This feature ensures that the owners of the data are accredited in any derivative works. Further, the data sets are listed in a citable data catalog entitled 'Database of H2020 M4F nanoindentation test data' at https://doi.org/10.5290/55.

A CEN Workshop on NAnoindentation TEst DAta (CEN/WS NATEDA) was completed. This included completion of a 4-point workplan, extending to (1) analysis of the data generated during application of ISO 14577-1:2015; (2) analysis of existing and development of new tools for data export; (3) development of computer readable terminology; and (4) case studies. The data specification, the development of which was the primary objective of the CEN/WS NATEDA, underwent a number of development iterations and was subject to review by both CEN/WS NATEDA registered participants and equipment manufacturers. With a view to verification of the efficacy of the data technologies, two CEN/WS NATEDA registered participants undertook an inter-laboratory data exchange study. By extending the reporting software of the testing equipment to support a module capable of exporting data in the CEN/WS NATEDA format, the test results were seamlessly transferred to the MatDB engineering materials database. Again, the corresponding data sets have been enabled for citation individually and as a citable catalog entitled 'CEN/WS NATEDA nanoindentation test data' at https://doi.org/10.5290/51. The relevant CEN publication, CWA 17552:2020, has been published. The successful outcome of CEN/WS NATEDA delivers data technologies that significantly reduce the data management overhead, thereby allowing straightforward collection, publication and reuse of data, which in turn ensures effective utilisation of the research investment (in the form of test data available in perpetuity) and promotes data reuse.

References

[1] J.S. Goldstein, S.A. Qvist, A Bright Future, PublicAffairs, New York, 2019.
[2] B.W. Brook, A. Alonso, D.A. Meneley, J. Misak, T. Blees, J.B. van Erp, Why nuclear energy is sustainable and has to be part of the energy mix. Sustainable, Materials and Technologies 1–2 (8–16) (2014), https://doi.org/10.1016/j.susmat.2014.11.001.
[3] IEA (May 2019). Nuclear Power in a Clean Energy System. Paris https://www.iea.org/reports/nuclear-power-in-a-clean-energy-system.
[4] J.A. Lake, R.G. Bennett, J.F. Kotek, Next Generation Nuclear Power, Scientific American (2009). https://www.scientificamerican.com/article/next-generation-nuclear/.
[5] A.J.H. Donné, G. Federici, X. Litaudon, D.C. McDonald, Scientific and technical challenges on the road towards fusion electricity, Journal of Instrumentation 12 (2017) C10008, https://doi.org/10.1088/1748-0221/12/10/C10008.
[6] P. Yvon, M. Le Flem, C. Cabet, J.L. Seran, Structural materials for next generation nuclear systems: Challenges and the path forward, Nuclear Engineering & Design 294 (2015) 161–169, https://doi.org/10.1016/j.nucengdes.2015.09.015.
[7] L. Malerba, M. Bertolus, K.-F. Nilsson, Available at: www.eera-jpnm.eu. Materials for Sustainable Nuclear Energy - The Strategic Research Agenda of the Joint Programme on Nuclear Materials of the European Energy Research Alliance, Publication Office of the European Union, Luxembourg, Euratom, 2019.
[8] L.K. Mansur, A.F. Rowcliffe, R.K. Nanstad, S.J. Zinkle, W.R. Corwin, R.E. Stoller, Materials needs for fusion: Generation IV fission reactors and spallation neutron sources – similarities and differences, Journal of Nuclear Materials 329–333 (2004) 166–172, https://doi.org/10.1016/j.jnucmat.2004.04.016.
[9] VV.AA., European Research Roadmap to the Realisation of Fusion Energy (2018). EUROfusion Programme Management Unit, Garching. ISBN 978-3-00-061152-0.

[10] C. Cabet, F. Dalle, E. Gaganidze, J. Henry, H. Tanigawa, Ferritic-martensitic steels for fission and fusion applications, Journal of Nuclear Materials 523 (2019) 510–537, https://doi.org/10.1016/j.jnucmat.2019.05.058.

[11] S.J. Zinkle and J.T. Busby (2009). Structural materals for fission and fusion energy. Materials Today 12(11), 12-19. ISSN:1369 7021.

[12] G. Federici, W. Biel, M.R. Gilbert, R. Kemp, N. Taylor, R. Wenninger, European DEMO design strategy and consequences for materials, Nuclear Fusion 57 (2017), 092002, https://doi.org/10.1088/1741-4326/57/9/092002.

[13] R. Chaouadi, Effect of irradiation-induced plastic flow localization on ductile crack resistance behavior of a 9%Cr tempered martensitic steel, Journal of Nuclear Materials 372 (2008) 379–390, https://doi.org/10.1016/j.jnucmat.2007.04.044.

[14] E. Gaganidze, J. Aktaa, Assessment of neutron irradiation effects on RAFM steels, Fusion Engineering and Design 88 (2013) 118–128, https://doi.org/10.1016/j.fusengdes.2012.11.020.

[15] F. Bergner, C. Pareige, M. Hernández-Mayoral, L. Malerba, C. Heintze, Application of a three-feature dispersed-barrier hardening model to neutron-irradiated Fe–Cr model alloys, Journal of Nuclear Materials 448 (2014) 96–102, https://doi.org/10.1016/j.jnucmat.2014.01.024.

[16] O. Anderoglu, T.S. Byun, M. Toloczko, S.A. Maloy, Mechanical performance of ferritic martensitic steels for high dose applications in advanced nuclear reactors, Metallurgical and Materials Transactions A 44 (1) (2013) 70–83, https://doi.org/10.1007/s11661-012-1565-y.

[17] K. Wang, Y. Dai, P. Spätig, Microstructure and fracture behavior of F82H steel under different irradiation and tensile test conditions, Journal of Nuclear Materials 468 (2016) 246, https://doi.org/10.1016/j.jnucmat.2015.09.031.

[18] B.N. Singh, A. Horsewell, P. Toft, Effects of neutron irradiation on microstructure and mechanical properties of pure iron, Journal of Nuclear Materials 271–272 (1999) 97–101, https://doi.org/10.1016/S0022-3115(98)00767-3.

[19] S.J. Zinkle, B.N. Singh, Microstructure of neutron-irradiated iron before and after tensile deformation, Journal of Nuclear Materials 351 (2006) 269–284, https://doi.org/10.1016/j.jnucmat.2006.02.031.

[20] E.H. Lee, M.H. Yoo, T.S. Byun, J.D. Hunn, K. Farrell, L.K. Mansur, On the origin of deformation microstructures in austenitic stainless steel: Part II—Mechanisms, Acta Materialia 49 (2001) 3277–3287, https://doi.org/10.1016/S1359-6454(01)00194-X.

[21] P.O. Barrioz, J. Hure, B. Tanguy, Effect of dislocation channeling on void growth to coalescence in FCC crystals, Materials Science and Engineering A 749 (2019) 255–270, https://doi.org/10.1016/j.msea.2019.01.115.

[22] K. Farrell, T.S. Byun, N. Hashimoto, Deformation mode maps for tensile deformation of neutron-irradiated structural alloys, Journal of Nuclear Materials 335 (2004) 471–486, https://doi.org/10.1016/j.jnucmat.2004.08.006.

[23] K. Gururaj, C. Robertson, M. Fivel, Post-irradiation plastic deformation in bcc Fe grains investigated by means of 3D dislocation dynamics simulations, Journal of Nuclear Materials 459 (2015) 194–204, https://doi.org/10.1016/j.jnucmat.2015.01.031.

[24] R.S. Nelson, D.J. Mazey, J.A. Hudson, The use of ion accelerators to simulate fast neutron-induced voidage in metals, Journal of Nuclear Materials 37 (1970) 1–12, https://doi.org/10.1016/0022-3115(70)90176-5.

[25] S.J. Zinkle, L.L. Snead, Opportunities and limitations for ion beams in radiation effects studies: Bridging critical gaps between charged particle and neutron irradiations, Scripta Materialia 143 (2018) 154–160, https://doi.org/10.1016/j.scriptamat.2017.06.041.

[26] E.R. Reese, N. Almirall, T. Yamamoto, S. Tumey, G.R. Odette, E.A. Marquis, Dose rate dependence of Cr precipitation in an ion-irradiated Fe single bond 18Cr alloy, Scripta Materialia 146 (2018) 213–217, https://doi.org/10.1016/j.scriptamat.2017.11.040.

[27] O. Tissot, C. Pareige, E. Meslin, B. Décamps, J. Henry, Influence of injected interstitials on α′ precipitation in Fe–Cr alloys under self-ion irradiation, Materials Research Letters 5 (2) (2017) 117–123, https://doi.org/10.1080/21663831.2016.1230896.

[28] J.G. Gigax, E. Aydogan, T. Chen, D. Chen, L. Shao, Y. Wu, The influence of ion beam rastering on the swelling of self-ion irradiated pure iron at 450 °C, Journal of Nuclear Materials 465 (2015) 343–348, https://doi.org/10.1016/j.jnucmat.2015.05.025.

[29] E. Getto, Z. Jiao, A.M. Monterrosa, K. Sun, G.S. Was, Effect of irradiation mode on the microstructure of self-ion irradiated ferritic-martensitic alloys, Journal of Nuclear Materials 465 (2015) 116–126, https://doi.org/10.1016/j.jnucmat.2015.05.016.

[30] C.-L. Ren, Y. Yang, Y.-G. Li, P. Huai, Z.-Y. Zhu, J. Li, Sample spinning to mitigate polarization artifact and interstitial-vacancy imbalance in ion-beam irradiation, NPJ Computational Materials 6 (2020) 189, https://doi.org/10.1038/s41524-020-00438-9.

[31] G.S. Was, S. Taller, Z. Jiao, A.M. Monterrosa, D. Woodley, D. Jennings, T. Kubley, F. Naab, O. Toader, E. Uberseder, Resolution of the carbon contamination problem in ion irradiation experiments, Nuclear Instruments and Methods B 412 (2017) 58–65, https://doi.org/10.1016/j.nimb.2017.08.039.

[32] J.G. Gigax, H. Kim, E. Aydogan, F.A. Garner, S. Maloy, L. Shao, Beam-contamination-induced compositional alteration and its neutron-atypical consequences in ion simulation of neutron-induced void swelling, Materials Research Letters 5 (2017) 478–485, https://doi.org/10.1080/21663831.2017.1323808.

[33] M. Hernández-Mayoral, C. Heintze, E. Oñorbe, Transmission electron microscopy investigation of the microstructure of Fe–Cr alloys induced by neutron and ion irradiation at 300°C, Journal of Nuclear Materials 474 (2016) 88–98, https://doi.org/10.1016/j.jnucmat.2016.03.002.

[34] M. Hernández-Mayoral et al. (a) Microstructure and Microchemistry Characterization of Ion-Irradiated FeCr Alloys (Concentration, Dose and Temperature Effect): TEM, PAS, APT and Synchrotron Techniques. (b) Microstructural and Mechanical Characterisation of Neutron-Irradiated FeCr Alloys (Concentration and Dose Effect): TEM, PAS, APT, SANS and Mechanical Tests, Deliverables D4.7 and D4.9, GETMAT FP7-Project, 2013. Available at: http://www.eera-jpnm.eu/filesharer/documents/_Euratom_Projects/Past%20projects/GETMAT%20public%20deliverables (last visited 6 May 2021).

[35] C. Heintze, F. Bergner, A. Ulbricht, H. Eckerlebe, The microstructure of neutron-irradiated Fe–Cr alloys: A small-angle neutron scattering study, Journal of Nuclear Materials 409 (2) (2011) 106–111, https://doi.org/10.1016/j.jnucmat.2010.09.010.

[36] C. Heintze, A. Ulbricht, F. Bergner, H. Eckerlebe, SANS investigation of neutron-irradiated Fe-Cr alloys, Journal of Physics: Conference Series 247 (2010), 012035, https://doi.org/10.1088/1742-6596/247/1/012035.

[37] V. Kuksenko, C. Pareige, C. Genevois, F. Cuvilly, M. Roussel, P. Pareige, Effect of neutron-irradiation on the microstructure of a Fe–12at.%Cr alloy, Journal of Nuclear Materials 415 (2011) 61–66, https://doi.org/10.1016/j.jnucmat.2011.05.042.

[38] V. Kuksenko, C. Pareige, P. Pareige, Cr precipitation in neutron irradiated industrial purity Fe–Cr model alloys, Journal of Nuclear Materials 432 (2013) 160–165, https://doi.org/10.1016/j.jnucmat.2012.07.021.

[39] C. Pareige, V. Kuksenko, P. Pareige, Behaviour of P, Si, Ni impurities and Cr in self ion irradiated Fe–Cr alloys – Comparison to neutron irradiation, Journal of Nuclear Materials 456 (2015) 471–476, https://doi.org/10.1016/j.jnucmat.2014.10.024.

[40] J.F. Ziegler, M.D. Ziegler, J.P. Biersack, SRIM - The stopping and range of ions in matter, Nuclear Instruments and Methods B 268 (11–12) (2010) 1818–1823, https://doi.org/10.1016/j.nimb.2010.02.091.

[41] R.E. Stoller, M.B. Toloczko, G.S. Was, A.G. Certain, S. Dwaraknath, F.A. Garner, On the use of SRIM for computing radiation damage exposure, Nuclear Instruments and Methods B 310 (2013) 75–80, https://doi.org/10.1016/j.nimb.2013.05.008.

[42] L.K. Mansur, Correlation of neutron and heavy-ion damage. II. The predicted temperature shift if swelling with changes in radiation dose rate, Journal of Nuclear Materials 78 (1978) 156–160, https://doi.org/10.1016/0022-3115(78)90514-7.

[43] M.J. Konstantinović, L. Malerba, Mechanical properties of FeCr alloys after neutron irradiation, Journal of Nuclear Materials 528 (2020), 151879, https://doi.org/10.1016/j.jnucmat.2019.151879.

[44] P. Olsson, I.A. Abrikosov, L. Vitos, J. Wallenius, Ab initio formation energies of Fe-Cr alloys, Journal of Nuclear Materials 321 (1) (2003) 84–90, https://doi.org/10.1016/S0022-3115(03)00207-1.

[45] A.A. Mirzoev, M.M. Yalalov, D.A. Mirzaev, Calculation of the energy of mixing for the Fe-Cr alloys by the first-principles methods of computer simulation, The Physics of Metals and Metallography 97 (4) (2004) 336–341.

[46] P. Olsson, I.A. Abrikosov, J. Wallenius, Electronic origin of the anomalous stability of Fe-rich bcc Fe-Cr alloys, Physical Review B 74 (2006), 104416, https://doi.org/10.1103/PhysRevB.73.104416.

[47] T.P.C. Klaver, R. Drautz, M.W. Finnis, Magnetism and thermodynamics of defect-free Fe-Cr alloys, Physical Review B 74 (2006), 094435, https://doi.org/10.1103/PhysRevB.74.094435.

[48] P. Olsson, C. Domain, J. Wallenius, Ab initio study of Cr interactions with point defects in bcc Fe, Physical Review B 75 (2007), 014110, https://doi.org/10.1103/PhysRevB.75.014110.

[49] G. Bonny, D. Terentyev, L. Malerba, On the alpha-alpha' miscibility gap of Fe-Cr alloys, Scripta Materialia 59 (2008) 1193–1196, https://doi.org/10.1016/j.scriptamat.2008.08.008.

[50] W. Xiong, M. Selleby, Q. Chen, J. Odqvist, Y. Du, Phase Equilibria and Thermodynamic Properties in the Fe-Cr System, Critical Reviews in Solid State and Materials Sciences 35 (2010) 125–152, https://doi.org/10.1080/10408431003788472.

[51] M.Yu. Lavrentiev, D. Nguyen-Manh, S.L. Dudarev, Magnetic cluster expansion model for bcc-fcc transitions in Fe and Fe-Cr alloys, Physical Review B 81 (2010), 184202, https://doi.org/10.1103/PhysRevB.81.184202.

[52] D. Terentyev, L. Malerba, A.V. Barashev, On the correlation between self-interstitial cluster diffusivity and irradiation-induced swelling in Fe–Cr alloys, Philosophical Magazine Letters 85 (11) (2005) 587–594, https://doi.org/10.1080/09500830500383563.

[53] S. Choudhury, L. Barnard, J.D. Tucker, T.R. Allen, B.D. Wirth, M. Asta, D. Morgan, Ab-initio based modeling of diffusion in dilute bcc Fe–Ni and Fe–Cr alloys and implications for radiation induced segregation, Journal of Nuclear Materials 411 (1–3) (2011) 1–14, https://doi.org/10.1016/j.jnucmat.2010.12.231.

[54] J.P. Wharry, G.S. Was, A systematic study of radiation-induced segregation in ferritic–martensitic alloys, Journal of Nuclear Materials 442 (2013) 7–16, https://doi.org/10.1016/j.jnucmat.2013.07.071.

[55] O. Senninger, F. Soisson, E. Martínez, M. Nastar, C.-C. Fu, Y. Bréchet, Modeling radiation induced segregation in iron–chromium alloys, Acta Materialia 103 (2016) 1–11, https://doi.org/10.1016/j.actamat.2015.09.058.

[56] L. Malerba, A. Caro, J. Wallenius, Multiscale modelling of radiation damage and phase transformations: The challenge of FeCr alloys, Journal of Nuclear Materials 382 (2008) 112–125, https://doi.org/10.1016/j.jnucmat.2008.08.014.

[57] L. Messina, T. Schuler, M. Nastar, M.-C. Marinica, P. Olsson, Solute diffusion by self-interstitial defects and radiation-induced segregation in ferritic Fe–X (X=Cr,

Cu, Mn, Ni, P, Si) dilute alloys, Acta Materialia 191 (2020) 166–185, https://doi.org/10.1016/j.actamat.2020.03.038.
[58] N. Castin, L. Messina, C. Domain, R.C. Pasianot, P. Olsson, Improved atomistic Monte Carlo models based on ab-initio-trained neural networks: Application to FeCu and FeCr alloys, Physical Review B 95 (2017), 214117, https://doi.org/10.1103/PhysRevB.95.214117.
[59] N. Castin, M.I. Pascuet, L. Messina, C. Domain, P. Olsson, R.C. Pasianot, L. Malerba, Advanced atomistic models for radiation damage in Fe-based alloys: Contributions and future perspectives from artificial neural networks, Computational Materials Science 148 (2018) 116–130, https://doi.org/10.1016/j.commatsci.2018.02.025.
[60] J.S. Wrobel, M.R. Zemła, D. Nguyen-Manh, P. Olsson, L. Messina, C. Domain, T. Wejrzanowski, S.L. Dudarev, Elastic dipole tensors and relaxation volumes of point defects in concentrated random magnetic Fe-Cr alloys, Computational Materials Science 194 (2021), 110435, https://doi.org/10.1016/j.commatsci.2021.110435.
[61] B. Minov (2012). Investigation of the Hardening of Neutron Irradiated and Thermally Aged Iron-Copper Alloys, on the Basis of Mechanical and Magnetic Relaxation Phenomena. PhD thesis, Ghent University. ISBN 978-90-8578-500-2. Available at: https://users.ugent.be/~ldupre/Phd_Boris_Minov.pdf (visited 01 July 2021).
[62] S.L. Dudarev, D.R. Mason, E. Tarleton, P.-W. Ma, A.E. Sand, A multi-scale model for stresses, strains and swelling of reactor components under irradiation, Nuclear Fusion 58 (2018), 126002, https://doi.org/10.1088/1741-4326/aadb48.
[63] J.B.J. Chapman, P.-W. Ma, S.L. Dudarev, Dynamics of magnetism in Fe-Cr alloys with Cr clustering, Physical Review B 99 (2019), 184413, https://doi.org/10.1103/PhysRevB.99.184413.
[64] K. Mergia, E.O. Tsompopoulou, S. Dellis, C.H. Marrows, I. Michelakaki, C. Kinane, A. Caruana, S. Langridge, A.P. Douvalis, C. Cabet, Phase stability of Fe-5at%Cr and Fe-10at%Cr films under Fe+ ion irradiation, Journal of Physics: Condensed Matter 32 (2020), 185702, https://doi.org/10.1088/1361-648X/ab69a1.
[65] M.Yu. Lavrentiev, S.L. Dudarev, D. Nguyen-Manh, Magnetic cluster expansion simulations of FeCr alloys, Journal of Nuclear Materials 386–388 (2009) 22, https://doi.org/10.1016/j.jnucmat.2008.12.052.
[66] M. Trochet, F. Soisson, C.-C. Fu and M. Yu. Lavrentiev (2021). Influence of magnetic excitation and vibrational entropy on the phase diagram of Fe1−xCrx alloys. Computational Materials Science, submitted.
[67] A. Schneider, C.-C. Fu, F. Soisson, C. Barreteau, Atomic Diffusion in α-iron across the Curie Point: An Efficient and Transferable Ab Initio-Based Modeling Approach, Physical Review Letters 124 (2020), 215901, https://doi.org/10.1103/PhysRevLett.124.215901.
[68] R. Alexander, L. Proville, C.S. Becquart, A.M. Goryaeva, J. Deres, C. Lapointe, M.-C. Marinica, Interatomic potentials for irradiation-induced defects in iron, Journal of Nuclear Materials 535 (2020), 152141, https://doi.org/10.1016/j.jnucmat.2020.152141.
[69] A.M. Goryaeva, C. Lapointe, C. Dai, J. Dérès, J.B. Maillet, M.-C. Marinica, Reinforcing materials modelling by encoding the structures of defects in crystalline solids into distortion scores, Nature Communications 11 (2020) 4691, https://doi.org/10.1038/s41467-020-18282-2.
[70] F. Gao, D.J. Bacon, A.V. Barashev and H.L. Heinisch (1998). Kinetic Monte Carlo Annealing Simulation of Damage Produced by Cascades in Alpha-Iron. MRS Online Proceedings Library Archive, Vol. 540: Symposium N / Microstructural Processes in Irradiated Materials, 703-708. 10.1557/PROC-540-703.
[71] N. Soneda and T. Díaz de La Rubia (1998). Defect production, annealing kinetics and damage evolution in -Fe: an atomic-scale computer simulation. Philosophical Magazine A 78, 995-1019. DOI: 10.1080/01418619808239970.
[72] N. Soneda, T. Diaz de la Rubia, Migration kinetics of the self-interstitial atom and its clusters in bcc Fe, Philosophical Magazine A 81 (2001) 331, https://doi.org/10.1080/01418610108214307.
[73] M.J. Caturla, N. Soneda, E. Alonso, B.D. Wirth, T. Diaz de la Rubia, J.M. Perlado, Comparative study of radiation damage accumulation in Cu and Fe, Journal of Nuclear Materials 276 (2000) 13–21, https://doi.org/10.1016/S0022-3115(99)00220-2.
[74] N. Soneda, S. Ishino, A. Takahashi, K. Dohi, Modeling the microstructural evolution in bcc-Fe during irradiation using kinetic Monte Carlo computer simulation, Journal of Nuclear Materials 323 (2003) 169–180, https://doi.org/10.1016/j.jnucmat.2003.08.021.
[75] C. Domain, C.S. Becquart, L. Malerba, Simulation of radiation damage in Fe alloys: an object kinetic Monte Carlo approach, Journal of Nuclear Materials 335 (2004) 121–145, https://doi.org/10.1016/j.jnucmat.2004.07.037.
[76] H. Xu, R.E. Stoller, Y.N. Osetsky, Cascade annealing simulations of bcc iron using object kinetic Monte Carlo, Journal of Nuclear Materials 423 (2012) 102–109, https://doi.org/10.1016/j.jnucmat.2012.01.020.
[77] C. Björkas, K. Nordlund, M.J. Caturla, Influence of the picosecond defect distribution on damage accumulation in irradiated α-Fe, Physical Review B 85 (2012), 024105, https://doi.org/10.1103/PhysRevB.85.024105.
[78] I. Martin-Bragado, A. Rivera, G. Valles, J.L. Gomez-Selles, M.J. Caturla, MMonCa: An Object Kinetic Monte Carlo simulator for damage irradiation evolution and defect diffusion, Computer Physics Communications 184 (2013) 2703–2710, https://doi.org/10.1016/j.cpc.2013.07.011.
[79] V. Jansson, M. Chiapetto, L. Malerba, The nanostructure evolution in Fe–C systems under irradiation at 560 K, Journal of Nuclear Materials 442 (2013) 341–349, https://doi.org/10.1016/j.jnucmat.2013.09.017.
[80] V. Jansson, L. Malerba, Simulation of the nanostructure evolution under irradiation in Fe–C alloys, Journal of Nuclear Materials 443 (2013) 274–285, https://doi.org/10.1016/j.jnucmat.2013.07.046.
[81] D. Terentyev, I. Martin-Bragado, Evolution of dislocation loops in iron under irradiation: The impact of carbon, Scripta Materialia 97 (2015) 5–8, https://doi.org/10.1016/j.scriptamat.2014.10.021.
[82] J.P. Balbuena, M.J. Aliaga, I. Dopico, M. Hernández-Mayoral, L. Malerba, I. Martin-Bragado and M.J. Caturla (2019). Insights from atomistic models on loop nucleation and growth in -Fe thin films under Fe+ 100 keV irradiation. Journal of Nuclear Materials 521, 71-80. 10.1016/j.jnucmat.2019.04.030.
[83] M. Chiapetto, L. Malerba, C.S. Becquart, Nanostructure evolution under irradiation in FeMnNi alloys: A ‘‘grey alloy’’ object kinetic Monte Carlo model, Journal of Nuclear Materials 462 (2015) 91–99, https://doi.org/10.1016/j.jnucmat.2015.03.045.
[84] M. Chiapetto, L. Malerba, C.S. Becquart, Effect of Cr content on the nanostructural evolution of irradiated ferritic/martensitic alloys: An object kinetic Monte Carlo model, Journal of Nuclear Materials 465 (2015) 326–336, https://doi.org/10.1016/j.jnucmat.2015.06.012.
[85] M. Chiapetto, C.S. Becquart, C. Domain, L. Malerba, Nanostructure evolution under irradiation of Fe(C)MnNi model alloys for reactor pressure vessel steels, Nuclear Instruments and Methods in Physics Research B 352 (2015) 56–60, https://doi.org/10.1016/j.nimb.2014.11.102.
[86] M. Chiapetto, C.S. Becquart, C. Domain, L. Malerba, Kinetic Monte Carlo simulation of nanostructural evolution under post-irradiation annealing in dilute FeMnNi, Physica Status Solidi C 12 (1–2) (2015) 20–24, https://doi.org/10.1002/pssc.201400143.
[87] M. Chiapetto, L. Malerba, C.S. Becquart, Simulation of nanostructural evolution under irradiation in Fe-9%Cr –C alloys: An object kinetic Monte Carlo study of the effect of temperature and dose-rate, Nuclear Materials and Energy 9 (2016) 565–570, https://doi.org/10.1016/j.nme.2016.04.009.
[88] M. Chiapetto, L. Malerba, A. Puype, C.S. Becquart, Object kinetic Monte Carlo study of the effect of grain boundaries in martensitic Fe–Cr–C alloys, Physica Status Solidi A 213 (11) (2016) 2981–2987, https://doi.org/10.1002/pssa.201600294.
[89] M. Chiapetto, L. Messina, C.S. Becquart, P. Olsson, L. Malerba, Nanostructure evolution of neutron-irradiated reactor pressure vessel steels: Revised Object kinetic Monte Carlo model, Nuclear Instruments and Methods in Physics Research B 393 (2017) 105–109, https://doi.org/10.1016/j.nimb.2016.09.025.
[90] M. Chiapetto, Computer simulation of the nanostructural evolution under irradiation in ferritic alloys, PhD. Thesis (defended in 2017), University of Lille, France, 2018.
[91] Y. Li, S. Hu, X. Sun, M. Stan, A review: applications of the phase field method in predicting microstructure and property evolution of irradiated nuclear materials, NPJ Computational Materials 3:16 (17 (2017) pp.), https://doi.org/10.1038/s41524-017-0018-y.
[92] A.A. Kohnert, B.D. Wirth, L. Capolungo, Modeling microstructural evolution in irradiated materials with clusterdynamics methods: A review, Computational Materials Science 149 (2018) 442–459, https://doi.org/10.1016/j.commatsci.2018.02.049.
[93] E. Martínez, J. Marian, M.H. Kalos, J.M. Perlado, Synchronous parallel kinetic Monte Carlo continuum diffusion-reaction systems, Journal of Computational Physics 227 (2008) 3804–3823, https://doi.org/10.1016/j.jcp.2007.11.045.
[94] I. Martin-Bragado, J. Abujas, P.L. Galindo, J. Pizarro, Synchronous parallel Kinetic Monte Carlo: Implementation and results for object and lattice approaches, Nuclear Instruments and Methods B 352 (2015) 27–30, https://doi.org/10.1016/j.nimb.2014.12.081.
[95] F. Jiménez, C.J. Ortiz, A GPU-based parallel Object kinetic Monte Carlo algorithm for the evolution of defects in irradiated materials, Computational Materials Science 113 (2016) 178–186, https://doi.org/10.1016/j.commatsci.2015.11.011.
[96] C.J. Ortiz and F. Mota (2019). Primary damage distribution in ion/neutron irradiated Fe/FeCr. M4F project, Deliverable D3.1. Available at https://cordis.europa.eu/project/id/755039/results.
[97] C.J. Ortiz, A combined BCA-MD method with adaptive volume to simulate high-energy atomic-collision cascades in solids under irradiation, Journal of Computational Materials Science 154 (2018) 325, https://doi.org/10.1016/J.COMMATSCI.2018.07.058.
[98] L. Malerba, N. Anento, J. P. Balbuena, C.S. Becquart, N. Castin, M. J. Caturla, C. Domain, C. Guerrero, C. Ortiz, B. Pannier, A. Serra (2021). Physical mechanisms and parameters for models microstructure evolution under irradiation in Fe alloys – part I: pure Fe. Nuclear Materials and Energy, submitted.
[99] M.J. Caturla, J.P. Balbuena, C. Ortiz, L. Malerba, C. Guerrero and N. Castin (2020). Milestone n° 3-2: Model parameterization to study microstructure evolution of Fe-Cr-C. M4F Project, Milestone M3.2/MS15. Available at http://www.h2020-m4f.eu/filesharer/documents/Deliverables%20&%20Milestones/Milestones (visited 01 July 2021).
[100] J.P. Balbuena, N. Castin, M.J. Caturla, C. Guerrero, L. Malerba, C. Ortiz. Validation of microstructure evolution models: limitations and applicability. M4F Deliverable D3.2/D13. Available at: https://ec.europa.eu/research/participants/documents/downloadPublic?documentIds=080166e5d6bf519c&appId=PPGMS (visited 25 June 2021).
[101] C.J. Ortiz, A. Souidi, C.S. Becquart, C. Domain, M. Hou, Recent radiation damage studies and developments of the Marlowe code, Radiation Effects & Defects in Solids 169 (7) (2014) 592–602, https://doi.org/10.1080/10420150.2014.920018.
[102] A. Dubinko, N. Castin, D. Terentyev, G. Bonny, M.J. Konstantinovic, Effect of SiNiP on the emergence of dislocations loops in Fe-9Cr matrix under neutron irradiation: TEM study and OKMC modelling, Journal of Nuclear Materials 540 (2020), 152395, https://doi.org/10.1016/j.jnucmat.2020.152395.

[103] M.J. Konstantinović, A. Ulbricht, T. Brodziansky, N. Castin, L. Malerba, Vacancy-solute clustering in Fe-Cr alloys after neutron irradiation, Journal of Nuclear Materials 540 (2020), 152341, https://doi.org/10.1016/j.jnucmat.2020.152341.
[104] S.L. Dudarev, K. Arakawa, X. Yi, Z. Yao, M.L. Jenkins, M.R. Gilbert, P.M. Derlet, Spatial ordering of nano-dislocation loops in ion-irradiated materials, Journal of Nuclear Materials 455 (2014) 16–20, https://doi.org/10.1016/j.jnucmat.2014.02.032.
[105] S.L. Dudarev, A.P. Sutton, Elastic interactions between nano-scale defects in irradiated materials, Acta Materialia 125 (2017) 425, https://doi.org/10.1016/j.actamat.2016.11.060.
[106] S.L. Dudarev, P.-W. Ma, Elastic fields, dipole tensors, and interaction between self-interstitial atom defects in bcc transition metals, Physical Review Materials 2 (2018), 033602, https://doi.org/10.1103/PhysRevMaterials.2.033602.
[107] S. Novy, P. Pareige, C. Pareige, Atomic scale analysis and phase separation understanding in a thermally aged Fe–20 at.%Cr alloy, Journal of Nuclear Materials 384 (2009) 96–102, https://doi.org/10.1016/j.jnucmat.2008.10.008.
[108] J.P. Balbuena, L. Malerba, N. Castin, G. Bonny, M.J. Caturla, An object kinetic Monte Carlo method to model precipitation and segregation in alloys under irradiation, Journal of Nuclear Materials 557 (2021), 153236, https://doi.org/10.1016/j.jnucmat.2021.153236.
[109] C. Pareige et al. (2017), Microstructural and mechanical characterisation of selected ion and neutron irradiated alloys, Deliverable D2.3.1, MATisse FP7-Project,. Available at: http://www.eera-jpnm.eu/filesharer/documents/_Euratom_Projects/Past%20projects/MatISSE (last visited 7 May 2021).
[110] F. Bergner, A. Ulbricht, C. Heintze, Estimation of the solubility limit of Cr in Fe at 300 °C from small-angle neutron scattering in neutron-irradiated Fe–Cr alloys, Scripta Materialia 61 (11) (2009) 1060–1063, https://doi.org/10.1016/j.scriptamat.2009.08.028.
[111] M.J. Konstantinovic, W. Van Renterghem, M. Matijasevic, B. Minov, M. Lambrecht, T. Toyama, M. Chiapetto, L. Malerba, Mechanical and microstructural properties of neutron irradiated Fe–Cr–C alloys, Physica Status Solidi (A) 213 (2016) 2988–2994, https://doi.org/10.1002/pssa.201600316.
[112] B. Gómez-Ferrer, C. Heintze, C. Pareige, On the role of Ni, Si and P on the nanostructural evolution of FeCr alloys under irradiation, Journal of Nuclear Materials 517 (2019) 35–44, https://doi.org/10.1016/j.jnucmat.2019.01.040.
[113] M. Bachhav, G.R. Odette, E. Marquis, α' precipitation in neutron-irradiated Fe-Cr alloys, Scripta Materuialia 74 (2014) 48–51, https://doi.org/10.1016/j.scriptamat.2013.10.001.
[114] M. Bachhav, G.R. Odette, E. Marquis, Microstructural changes in a neutron-irradiated Fe–15 at.%Cr alloy, Journal of Nuclear Materials 454 (2014) 381–386, https://doi.org/10.1016/j.jnucmat.2014.08.026.
[115] M. Bachhav, L. Yao, G.R. Odette, E. Marquis, Microstructural changes in a neutron-irradiated Fe–6 at.%Cr alloy, Journal of Nuclear Materials 453 (2014) 334–339, https://doi.org/10.1016/j.jnucmat.2014.06.050.
[116] L. Messina, M. Nastar, N. Sandberg, P. Olsson, Systematic electronic-structure investigation of substitutional impurity diffusion and flux coupling in bcc iron, Physical Review B 93 (2016), 184302, https://doi.org/10.1103/PhysRevB.93.184302.
[117] N. Castin, G. Bonny, A. Bakaev, F. Bergner, C. Domain, J.M. Hyde, L. Messina, B. Radiguet, L. Malerba, The dominant mechanisms for the formation of solute-rich clusters in low-Cu steels under irradiation, Materials Today Energy 17 (2020), 100472, https://doi.org/10.1016/j.mtener.2020.100472.
[118] C. Domain, C.S. Becquart, Solute-⟨111⟩ interstitial loop interaction in α-Fe: A DFT study, Journal of Nuclear Materials 499 (2018) 582–594, https://doi.org/10.1016/j.jnucmat.2017.10.070.
[119] G. Monnet, Multiscale modeling of irradiation hardening: Application to important nuclear materials, Journal of Nuclear Materials 508 (2018) 609–627, https://doi.org/10.1016/j.jnucmat.2018.06.020.
[120] V. Bryk, O. Borodin, A. Kalchenko, V. Voyevodin, V. Ageev, A. Nikitina, V. Novikov, V. Inozemtsev, A. Zeman and F. Garner (2013). Ion issues on irradiation behaviour of structural materials at high doses and gas concentrations. Proc. 11th International Topical Meeting on Nuclear Applications of Accelerators, Bruges.
[121] F. Bergner, A. Ulbricht, A. Gokhman, D. Erak, Nature of defect clusters in neutron-irradiated iron-based alloys deduced from small-angle neutron scattering, Journal of Nuclear Materials 373 (1–3) (2008) 199–205, https://doi.org/10.1016/j.jnucmat.2007.05.044.
[122] M. Prester, D. Drobac, Z. Marohnic, V. Surija, N. Novosel, M.J. Konstantinović, High temperature magnetic after-effect studies of iron and iron-chromium steels. In preparation, 2021.
[123] W.D. Nix, H. Gao, Indentation size effects in crystalline materials: a law for strain gradient plasticity, Journal of the Mechanics and Physics of Solids 46 (1998) 411–425, https://doi.org/10.1016/S0022-5096(97)00086-0.
[124] A. Bakaev, J. Zhao, D. Terentyev, G. Bonny, N. Castin, N. Kvashin, A. Kuronen, E. E. Zhurkin and K. Nordlund (2021). Effect of radiation defects on the early stages of nanoindentation tests in bcc Fe and Fe-Cr alloys. Computational Materials Science, submitted.
[125] G. Bonny, R.C. Pasianot, D. Terentyev, L. Malerba, Iron Chromium Potential to Model High-Chromium Ferritic Alloys, Philosophical Magazine 91 (12) (2011) 1724–1746, https://doi.org/10.1080/14786435.2010.545780.
[126] J.S. Weaver, S. Pathak, A. Reichardt, H.T. Vo, S.A. Maloy, P. Hosemann, N. A. Mara, Spherical nanoindentation of proton irradiated 304 stainless steel: A comparison of small scale mechanical test techniques for measuring irradiation hardening, Journal of Nuclear Materials 493 (2017) 368–379, https://doi.org/10.1016/j.jnucmat.2017.06.031.
[127] E. Martínez-Pañeda, C. Betegón, Modeling damage and fracture within strain-gradient plasticity, International Journal of Solids and Structures 59 (2015) 208–215, https://doi.org/10.1016/j.ijsolstr.2015.02.010.
[128] A. Ruiz-Moreno, P. Hähner, F. Fumagalli, V. Haiblikova, M. Conte, N. Randall, Stress-strain curves and derived mechanical parameters of P91 steel from spherical nanoindentation at a range of temperatures, Materials and Design 194 (2020), 108950, https://doi.org/10.1016/j.matdes.2020.108950.
[129] X. Hou, N.M. Jennett, Application of a modified slip-distance theory to the indentation of single and poly–crystalline copper to model the interactions between indentation size and structure size effects, Acta Materialia 60 (10) (2012) 4128–4135, https://doi.org/10.1016/j.actamat.2012.03.054.
[130] L. Veleva, P. Hähner, A. Dubinko, T. Khvan, D. Terentyev, A. Ruiz-Moreno, Depth sensing hardness measurements to probe hardening behaviour and dynamic strain ageing of pure Fe during tensile pre deformation, Nanomaterials 11 (2021) 71, https://doi.org/10.3390/nano11010071.
[131] A. Ruiz-Moreno, P. Hähner, L. Kurpaska, J. Jagielski, P. Spätig, M. Trebala, S. P. Hannula, S. Merino, G. de Diego, H. Namburi, O. Libera, D. Terentyev, T. Khvan, C. Heintze, N.M. Jennett, Round Robin into Best Practices for the Determination of Indentation Size Effects, Nanomaterials 10 (2020) 130, https://doi.org/10.3390/nano10010130.
[132] O. Libera, H.K. Namburi, P. Gávelová, P. Kůs, Nanoindentation testing of nuclear materials at Research Centre Rez. REMOO 2019 Conference Proceedings, 2019.
[133] K. Vogel, C. Heintze, P. Chekhonin, S. Akhmadaliev, E. Altstadt, F. Bergner, Relationships between depth-resolved primary radiation damage, irradiation-induced nanostructure and nanoindentation response of ion-irradiated Fe-Cr and ODS Fe-Cr alloys, Nuclear Materials and Energy 24 (2020), 100759, https://doi.org/10.1016/j.nme.2020.100759.
[134] M. Clozel, Ł. Kurpaska, I. Jóźwik, J. Jagielski, E. Wyszkowska, Nanomechanical properties of low-energy Fe-ion implanted Eurofer97 and pure Fe, Surface & Coatings Technology 393 (2020), 125833, https://doi.org/10.1016/j.surfcoat.2020.125833.
[135] M. Clozel, Ł. Kurpaska, J.H. O'Connell, I. Jóźwik, E. Wyszkowska, J. Jagielski, J. H. Neethling (2021). Impact of the precipitates on hardening and softening phenomena of Fe-Cr alloys analyzed in-situ at high temperature via nanoindentation technique. Journal of Nuclear Materials, submitted.
[136] D.J. Bacon, Y.N. Osetsky, Z. Rong, Computer simulation of reactions between an edge dislocation and glissile self-interstitial clusters in iron, Philosophical Magazine 86 (25–26) (2006) 3921–3936, https://doi.org/10.1080/14786430600570527.
[137] D. Terentyev, L. Malerba, D.J. Bacon, Yu.N. Osetsky, The effect of temperature and strain rate on the interaction between an edge dislocation and an interstitial dislocation loop in α-iron, Journal of Physics: Condensed Matter 19 (2007), 456211, https://doi.org/10.1088/0953-8984/19/45/456211.
[138] D. Terentyev, P. Grammatikopoulos, D.J. Bacon, Yu.N. Osetsky, Simulation of the interaction between an edge dislocation and a <100> interstitial dislocation loop in α-iron, Acta Materialia 56 (2008) 5034–5046, https://doi.org/10.1016/j.actamat.2008.06.032.
[139] X.-Y. Liu, S.B. Biner, Molecular dynamics simulations of the interactions between screw dislocations and self-interstitial clusters in body-centered cubic Fe, Scripta Materialia 59 (2008) 51–54, https://doi.org/10.1016/j.scriptamat.2008.02.031.
[140] D. Terentyev, G. Bonny, L. Malerba, Mobility of dislocations in thermal aged and irradiated Fe–Cr alloys, Journal of Nuclear Materials 386–388 (2009) 257–260, https://doi.org/10.1016/j.jnucmat.2008.12.106.
[141] D. Terentyev, D.J. Bacon, Yu.N. Osetsky, Reactions between a ½<111> screw dislocation and <100> interstitial dislocation loops in alpha-iron modelled at atomic scale, Philosophical Magazine 90 (7–8) (2010) 1019–1033, https://doi.org/10.1080/14786430903019073.
[142] D. Terentyev, Yu.N. Osetsky, D.J. Bacon, Competing processes in reactions between an edge dislocation and dislocation loops in a body-centred cubic metal, Scripta Materialia 62 (2010) 697–700, https://doi.org/10.1016/j.scriptamat.2010.01.034.
[143] D. Terentyev, N. Anento, A. Serra, Interaction of dislocations with carbon-decorated dislocation loops in bcc Fe: an atomistic study, Journal of Physics: Condensed Matter 24 (2012), 455402, https://doi.org/10.1088/0953-8984/24/45/455402.
[144] D. Terentyev, F. Bergner and Y. Osetsky (2013). Cr segregation on dislocation loops enhances hardening in ferritic Fe–Cr alloys. Acta Materialia 61, 1444–1453. DOI: /10.1016/j.actamat.2012.11.021.
[145] D. Terentyev, A. Bakaev, Radiation-induced strengthening and absorption of dislocation loops in ferritic Fe–Cr alloys: the role of Cr segregation, Journal of Physics: Condensed Matter 25 (2013), 265702, https://doi.org/10.1088/0953-8984/25/26/265702.
[146] D. Terentyev, G. Bonny, C. Domain, G. Monnet and L. Malerba (2013). Mechanisms of radiation strengthening in Fe–Cr alloys as revealed by atomistic studies. Journal of Nuclear Materials 442, 470–485. DOI: /10.1016/j.jnucmat.2013.03.054.
[147] D. Terentyev, A. Bakaev and E.E. Zhurkin (2014). Effect of carbon decoration on the absorption of ⟨100⟩ dislocation loops by dislocations in iron. Journal of Physics: Condensed Matter 26, 165402. DOI: 10.1088.0953-8984/26/16/165402.
[148] T. Nogaret, D. Rodney, M. Fivel, C. Robertson, Clear band formation simulated by dislocation dynamics: Role of helical turns and pile-ups, Journal of Nuclear Materials 380 (2008) 22–29, https://doi.org/10.1016/j.jnucmat.2008.07.00.
[149] J.S. Robach, I.M. Robertson, B.D. Wirth, A. Arsenlis, In-situ transmission electron microscopy observations and molecular dynamics simulations of dislocation-

defect interactions in ion-irradiated copper, Philosophical Magazine 83 (8) (2003) 955–967, https://doi.org/10.1080/0141861031000065329.
[150] A. Arsenlis, M. Rhee, G. Hommes, R. Cook, J. Marian, A dislocation dynamics study of the transition from homogeneous to heterogeneous deformation in irradiated body-centered cubic iron, Acta Materialia 60 (9) (2012) 3748–3757, https://doi.org/10.1016/j.actamat.2012.03.041.
[151] P.J. Doyle, K.M. Benensky, S.J. Zinkle, Modeling of dislocation channel width evolution in irradiated metals, Journal of Nuclear Materials 499 (2018) 47–64, https://doi.org/10.1016/j.jnucmat.2017.10.063.
[152] Y. Cui, G. Po, N.M. Ghoniem, A coupled dislocation dynamics-continuum barrier field model with application to irradiated materials, International Journal of Plasticity 104 (2018) 54–67, https://doi.org/10.1016/j.ijplas.2018.01.015.
[153] X.J. Shi, L. Dupuy, B. Devincre, D. Terentyev, L. Vincent, Interaction of ≤100≥ dislocation loops with dislocations studied by dislocation dynamics in α-iron, Journal of Nuclear Materials 460 (2015) 37–43, https://doi.org/10.1016/j.jnucmat.2015.01.061.
[154] L. Ventelon, B. Lüthi, E. Clouet, L. Proville, B. Legrand, D. Rodney, F. Willaime, Dislocation core reconstruction induced by carbon segregation in bcc iron, Physical Review B 91 (2015) 220102(R), https://doi.org/10.1103/PhysRevB.91.220102.
[155] G. Bonny, A. Bakaev, D. Terentyev, Energetic Stability of Vacancy-Carbon Clusters in Solid Solution Alloys: The Fe-Cr-C Case, Physica Status Solidi B 256 (2019) 1900130, https://doi.org/10.1002/pssb.201900130.
[156] G. Bonny, D. Terentyev, J. Elena, A. Zinovev, B. Minov, E.E. Zhurkin, Assessment of hardening due to dislocation loops in bcc iron: Overview and analysis of atomistic simulations for edge dislocations, Journal of Nuclear Materials 473 (2016) 283–289, https://doi.org/10.1016/j.jnucmat.2016.02.031.
[157] G. Bonny, A. Bakaev, D. Terentyev, E. Zhurkin, M. Posselt, Atomistic study of the hardening of ferritic iron by Ni-Cr decorated dislocation loops, Journal of Nuclear Materials 498 (2018) 430–437, https://doi.org/10.1016/j.jnucmat.2017.11.016.
[158] N. Kvashin, P.L. García-Müller, N. Anento, A. Serra, Atomic processes of shear-coupled migration in 112 twins and vicinal grain boundaries in bcc-Fe, Physical Review Materials 4 (7) (2020), 073604, https://doi.org/10.1103/PhysRevMaterials.4.073604.
[159] D. Terentyev, A. Bakaev, A. Serra, F. Pavia, K.L. Baker, N. Anento, Grain boundary mediated plasticity: The role of grain boundary atomic structure and thermal activation, Scripta Materialia 145 (2018) 1–4, https://doi.org/10.1016/j.scriptamat.2017.10.002.
[160] N. Kvashin, N. Anento, D. Terentyev, A. Bakaev, A. Serra, Interaction of a dislocation pileup with 332 tilt grain boundary in bcc metals studied by MD simulations, Physical Review Materials 5 (2021), 013605, https://doi.org/10.1103/PhysRevMaterials.5.013605.
[161] A. Serra, N.A. Kvashin, N. Anento, On the common topological conditions for shear-coupled twin boundary migration in bcc and hcp metals, Letters on Materials 10 (2020) 537–542, https://doi.org/10.22226/2410-3535-2020-4-537-542.
[162] D. Rodney, L. Dupuy, MD simulations to develop a DD code with dislocation mobility and defect resistance. Milestone MS29 (M4.2). M4F project. Available at: http://www.h2020-m4f.eu/filesharer/documents/Deliverables%20&%20Milestones/Milestones, 2021 (last visited 29 June 2021).
[163] L. Proville, D. Rodney, M.-C. Marinica, Quantum effect on thermally activated glide of dislocations, Nature Materials 11 (2012) 845–849, https://doi.org/10.1038/NMAT3401.
[164] D. Brunner, J. Diehl, Softening of α-iron by solute nitrogen atoms investigated between 30 and 300 K by use of stress-relaxation measurements, Materials Science and Engineering A 164 (1993) 350–355, https://doi.org/10.1016/0921-5093(93)90691-7.
[165] M. Boleininger, T.D. Swinburne, L. Dupuy, S.L. Dudarev, Ultraviolet catastrophe of a fluctuating curved dislocation line, Physical Review Research 2 (3) (2020), 032033, https://doi.org/10.1103/PhysRevResearch.2.032033.
[166] Y. Li, M. Boleininger, C. Robertson, L. Dupuy, S.L. Dudarev, Diffusion and interaction of prismatic dislocation loops simulated by stochastic discrete dislocation dynamics, Physical Review Materials 3 (7) (2019), 073805, https://doi.org/10.1103/PhysRevMaterials.3.073805.
[167] J. Drouet, L. Dupuy, F. Onimus, F. Mompiou, A direct comparison between in situ transmission electron microscopy observations and dislocation dynamics simulations of interaction between dislocation an irradiation induced loop in a zirconium alloy, Scripta Materialia 119 (2016) 71–75, https://doi.org/10.1016/j.scriptamat.2016.03.029.
[168] L. Gélébart, R. Mondon-Cancel, Non-linear extension of FFT-based methods accelerated by conjugate gradients to evaluate the mechanical behavior of composite materials, Computational Materials Science 77 (2013) 430–439, https://doi.org/10.1016/j.commatsci.2013.04.046.
[169] C. Robertson, Y. Li, B. Marini, Dose-dependent strain localization and embrittlement in ferritic materials: a predictive approach based on grain-scale modelling results. In preparation, 2021.
[170] C.R. Weinberger, B.L. Boyce, C.C. Battaile, Slip planes in bcc transition metals, International Materials Reviews 58 (5) (2013) 296–314, https://doi.org/10.1179/1743280412Y.0000000015.
[171] B.A. Senior, F.W. Noble, B.L. Eyre, The nucleation and growth of voids at carbides in 9 Cr-1 Mo steel, Acta Metallurgica 34 (1986) 1321–1327, https://doi.org/10.1016/0001-6160(86)90019-2.
[172] Y. Chen, P. Spätig, M. Victoria, The mechanical properties of 590 MeV proton irradiated iron, Journal of Nuclear Materials 271&272 (1999) 128–132, https://doi.org/10.1016/S0022-3115(98)00702-8.
[173] L. Malerba, M.C. Marinica, N. Anento, C. Björkas, H. Nguyen, C. Domain, F. Djurabekova, P. Olsson, K. Nordlund, A. Serra, D. Terentyev, F. Willaime, C. S. Becquart, Comparison of empirical interatomic potentials for iron applied to radiation damage studies, Journal of Nuclear Materials 406 (2010) 19–38, https://doi.org/10.1016/j.jnucmat.2010.05.017.
[174] E. Vamvakopoulos and D. Tanguy (2009). Equilibrium vacancy concentrations in Al-Σ=33(554)[11 ¯0] by grand canonical Monte Carlo simulations. Physical Review B 79, 094116-1. DOI: 10.1103/PhysRevB.79.094116.
[175] D. Gonçalves (2018). Modélisation polycristalline du comportement élasto-viscoplastique des aciers inoxydables austénitiques 316L(N) sur une large gamme de chargements: application à l'étude du comportement cyclique à température élevée. PhD thesis, UPMC Paris IV. Available at : https://hal.archives-ouvertes.fr/tel-02325387/ (last visited 01 July 2021).
[176] T. Yalçinkaya, Strain Gradient Crystal Plasticity: Thermodynamics and Implementation, in: G. Voyiadjis (Ed.), Handbook of Nonlocal Continuum Mechanics for Materials and Structures, Springer, Cham, 2016, https://doi.org/10.1007/978-3-319-22977-5_2-1.
[177] T. Yalçinkaya, İ. Özdemir, I. Simonovski, Micromechanical modeling of intrinsic and specimen size effects in microforming, International Journal of Material Forming 11 (2018) 729–741, https://doi.org/10.1007/s12289-017-1390-3.
[178] M. Eldrup, B.N. Singh, S.J. Zinkle, T.S. Byun, K. Farrell, Dose dependence of defect accumulation in neutron irradiated copper and iron, Journal of Nuclear Materials 307–311 (2002) 912, https://doi.org/10.1016/S0022-3115(02)01160-1.
[179] M.F. Giordana, P.-F. Giroux, I. Alvarez-Armas, M. Sauzay, A. Armas, T. Kruml, Microstructure evolution during cyclic tests on EUROFER 97 at room temperature. TEM observation and modelling, Materials Science and Engineering A 550 (2012) 103–111, https://doi.org/10.1016/j.msea.2012.04.038.
[180] S.B. Kass and K.L. Murty (1995). Effect of Neutron Irradiation on Mechanical Properties of Ferritic Steels. Annual meeting and exhibition of the Minerals, Metals and Materials Society (TMS), Las Vegas, NV (United States), 12-16 Feb 1995, CONF-950201—25, INIS 30(28) 27-35, 30031290. https://inis.iaea.org/collection/NCLCollectionStore/_Public/30/031/30031290.pdf?r=1.
[181] X. Xiao, Fundamental Mechanisms for Irradiation-Hardening and Embrittlement: A Review, Metals 9 (2019) 1132, https://doi.org/10.3390/met9101132.
[182] G. Monnet, L. Vincent, L. Gélebart, Multiscale modeling of crystal plasticity in Reactor Pressure Vessel steels: Prediction of irradiation hardening, Journal of Nuclear Materials 541 (2019) 128, https://doi.org/10.1016/j.jnucmat.2018.11.028.
[183] T. Yalcinkaya, W.A.M. Brekelmans, M.G.D. Geers, Deformation patterning driven by rate dependent non-convex strain gradient plasticity, Journal of the Mechanics and Physics of Solids 59 (2011) 1–17, https://doi.org/10.1016/j.jmps.2010.10.002.
[184] T. Yalcinkaya, W.A.M. Brekelmans, M.G.D. Geers, Non-convex rate dependent strain gradient crystal plasticity and deformation patterning, International Journal of Solids and Structures 49 (2012) 2625–2636, https://doi.org/10.1016/j.ijsolstr.2012.05.029.
[185] R.R. Rajakrishnan, E. Gaganidze, J. Aktaa, Macro-scale modelling of finite strain viscoplasticity in irradiated F/M steels: continuum thermodynamic framework, Continuum Mechanics and Thermodynamics, in preparation (2021).
[186] J. Aktaa, C. Petersen, Modeling the constitutive behavior of RAFM steels under irradiation conditions, Journal of Nuclear Materials 417 (2011) 1123–1126, https://doi.org/10.1016/j.jnucmat.2010.12.295.
[187] P. Haupt, Ch. Tsakmakis, On the application of dual variables in continuum mechanics, Continuum Mechanics and Thermodynamics 1 (1989) 165–196, https://doi.org/10.1007/BF01171378.
[188] T.J.R. Hughes, J. Winget, Finite rotation effects in numerical integration of rate constitutive equations arising in large-deformation analysis, International Journal for Numerical Methods in Engineering 15 (12) (1980) 1862–1867, https://doi.org/10.1002/nme.1620151210.
[189] G.G.A. Weber, Computational procedures for a new class of finite deformation elastic-plastic constitutive equations, PhD thesis, MIT, 1988.
[190] V. Tvergaard, A. Needleman, Analysis of the cup-cone fracture in a round tensile bar, Acta Metallurgica 32 (1) (1984) 157–169, https://doi.org/10.1016/0001-6160(84)90213-X.
[191] L. Stratil, F. Siska, H. Hadraba, I. Dlouhy, Modeling of Ductile Tearing for RAFM Steel Eurofer97, Procedia Materials Science 3 (2014) 1155–1160, https://doi.org/10.1016/j.mspro.2014.06.188.
[192] Y. Ling, Uniaxial True Stress-Strain after Necking, AMP Journal of Technology 5 (1996) 37–48.
[193] L. Malerba (2020). Large Scale Integrated Materials Modeling Programs. In: R.J. M. Konings and R.E. Stoller (eds.), Comprehensive Nuclear Materials 2nd Ed. Vol. 1, 881–916, Oxford, Elsevier. 10.1016/b978-0-12-803581-8.11601-7.
[194] S. Taioli, M. Dapor, N.M. Pugno, "Editorial: New Frontiers in Multiscale Modelling of Advanced Materials", in: S. Taioli, M. Dapor, N.M. Pugno, Eds., New Frontiers in Multiscale Modelling of Advanced Materials (Lausanne, 2016). 10.3389/978-2-88919-755-2 10.3389/fmats.2015.00071.
[195] G. Aiello, J. Aktaa, F. Cismondi, G. Rampal, J.-F. Salavy, F. Tavassoli, Assessment of design limits and criteria requirements for Eurofer structures in TBM components, Journal of Nuclear Materials 414 (2011) 53–68, https://doi.org/10.1016/j.jnucmat.2011.05.005.
[196] D.P. Tabor, L.M. Roch, S.K. Saikin, et al., Accelerating the discovery of materials for clean energy in the era of smart automation, Nature Reviews Materials 3 (2018) 5–20, https://doi.org/10.1038/s41578-018-0005-z.